

Voltage control of uniaxial and unidirectional magnetic thin films by electrochemical reactions

Von der Fakultät Maschinenwesen
der Technischen Universität Dresden
zur Erlangung des akademischen Grades
Doktoringenieur (Dr.-Ing.)
angenommene

DISSERTATION

von

Dipl.-Ing. Jonas Zehner
geb. am 09.08.1988 in Schweinfurt

angefertigt am

Leibniz-Institut für Festkörper- und Werkstoffforschung (IFW) Dresden e.V.

eingereicht am 17.12.2020

verteidigt am 29.06.2021

© 2021

All rights reserved

Erstgutachter: Prof. Dr. Kornelius Nielsch
Zweitgutachter: Prof. Dr. Sebastian Gönnerwein
Drittgutachterin: Dr. habil. Liza Herrera Diez

Vorsitzende der Promotionskommission: Prof. Dr. Kerstin Eckert
Mitglied der Promotionskommission: Prof. Dr. Ginaurelio Cuniberti
Fachbetreuerin: Dr. Karin Leistner

TABLE OF CONTENTS

1	Introduction.....	1
2	Fundamentals of magnetic thin films.....	5
3	State of the Art	11
3.1	Voltage control of magnetism	11
3.2	Electrochemical control of magnetism	14
4	Methods.....	21
4.1	Film fabrication	21
4.2	Ex-situ and in-situ analytical characterization.....	22
4.3	Electrochemical characterization.....	24
4.4	Magneto-optical Kerr Magnetometry and Microscopy	25
5	Combining Kerr microscopy and electrochemistry – the in situ cell.....	29
6	In-plane uniaxial anisotropy and blocked domain state in FeO_x/Fe thin films.....	33
6.1	Microstructure and composition.....	33
6.2	Magnetically blocked state in pristine FeO _x /Fe thin film.....	34
7	Voltage control of FeO_x/Fe thin films with in-plane uniaxial anisotropy	41
7.1	Voltage control of hysteresis by electrochemical reduction of FeO _x	41
7.2	Inverse scaling of coercivity and anisotropy revealed by anhysteresis	44
7.3	Voltage control of magnetic domains.....	46
7.4	Magnetic de-blocking due to change of Néel wall interactions	48
7.5	Switching of magnetization by a low voltage and energy efficiency	51
7.6	Energy efficiency and application potential for data storage and actuation.....	53
7.7	Interim conclusion	54

8 Voltage control of FeO_x/Fe/IrMn thin films with in-plane unidirectional anisotropy	57
8.1 Characterization of the pristine state exchange biased thin films.....	57
8.2 Electrochemical modification of EB – voltage dependency.....	58
8.3 Electrochemical modification of EB – time dependency.....	61
8.4 Model for voltage control of EB by electrochemistry	64
8.5 Non-volatile and reversible voltage control of exchange bias	65
8.6 Nonvolatile change of oxidation state and layer thickness	67
8.7 Electrochemical patterning of EB and magnetic domain state	68
8.8 Interim conclusion.....	70
9 Voltage control of magnetic thin films with perpendicular unidirectional anisotropy	73
9.1 Co thin films with perpendicular unidirectional anisotropy	73
9.2 Voltage control of EB in Co/Pd/NiO thin films.....	73
9.3 Interim conclusion.....	81
9.4 Voltage control of ferrimagnetic GdCo/Pd/NiO thin film	81
10 Evaluation with regard to perspective applications.....	83
11 Summary	87
12 Appendix	93
References.....	107
List of Figures	121
Publication List	123
Acknowledgments	125
Symbols.....	127
Statement of Authorship	129

1 Introduction

The results of chapter 6 and 7 are published in [1], chapter 8 is published in [2] and chapter 9 is partly published in [3] within the framework of this thesis. The respective paragraphs – with minor adjustments – are indicated in grey font. Reprint from [1] under Creative Commons Attribution (CC BY) license (<https://creativecommons.org/licenses/by/4.0/>). Reprint from [2] under permission from © 2019 WILEY-VCH Verlag GmbH & Co. KGaA, Weinheim. Reprinted with permission from [3] (Copyright 2021, <https://doi.org/10.1103/PhysRevMaterials.5.L061401>) by the American Physical Society.

Motivation

Reducing the electrical energy demand of magnetic devices used for data storage and memory in computing processes, as well as of micro- and nanotechnological systems in general, is a major global challenge.[1] The aforementioned magnetic systems are embedded in the information and communication technology (ICT) sector which consumes about 11 % of the global electricity use, see **Figure 1.1**. [4] It is predicted that the energy consumption of the ICT sector will further rise over time. [4] The high energy consumption is in wide parts due to the use of external magnetic fields or large spin-polarized electrical currents which lead to undesired Joule heating and thus energy losses. A promising alternative for increasing the energy efficiency of magnetic devices is to control the magnetism by electric fields instead of electric currents. Since magnetoelectric materials offer the possibility to control their magnetic properties via a voltage, intense research efforts have been pursued in exploring these materials. However, the voltage induced effects occur mainly at low temperatures, high voltages and/or in material systems with a complex layer fabrication. [1,5]

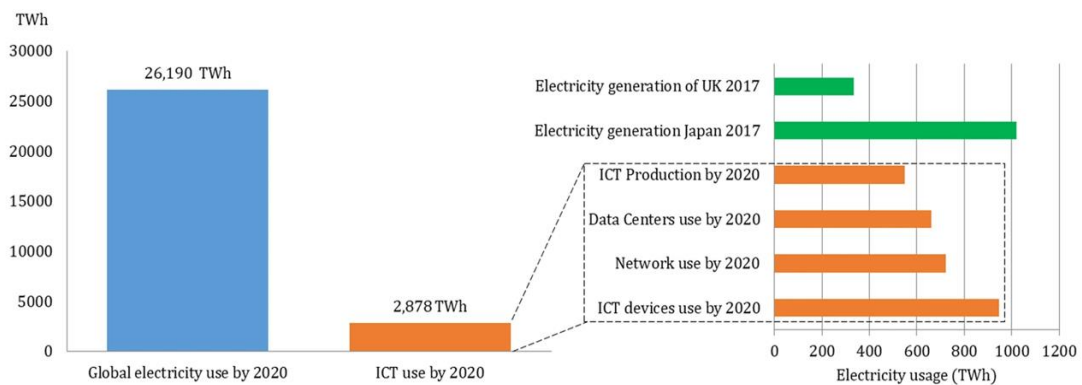


Figure 1.1. Electricity consumption of the ICT sector and involved subsections. In a more intuitive picture, the electricity usage of Data Centers is about two times the amount of electricity which is produced in the UK. Reprint from [4] with permission under Creative Common (CC BY) licence. (<https://creativecommons.org/licenses/by/4.0/>)

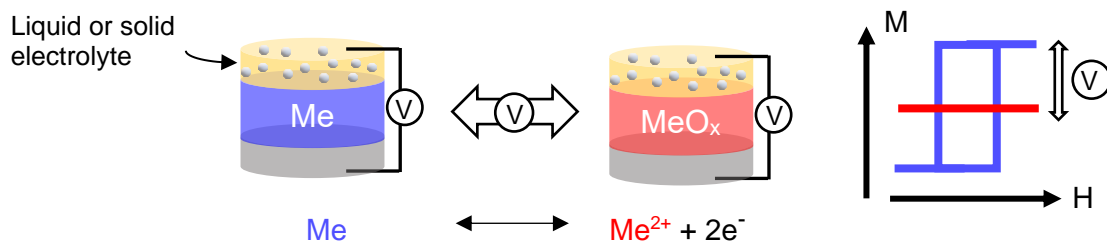


Figure 1.2. Electrochemical reactions and subsequent changes on the magnetic properties. Voltage controlled transformation of a ferromagnetic metal (Me) into a weakly-magnetic oxide (MeO_x) leads to significant changes of the magnetic properties.

A topical magnetoelectric approach is the voltage control of magnetic nanostructures via an electrolyte or a dielectric oxide. [1,5–7] **Figure 1.2** shows an example of magnetic property changes induced by electrochemical reaction, manifested by a transformation of a magnetic metallic layer into a weakly-magnetic oxide. Here, ferro- and ferrimagnetic metals or oxides, with a high Curie temperature and magnetization, are suitable materials. [1] In comparison to conventional strain-based magnetoelectric composites and magnetic semiconductors, this approach offers the combined advantages of large effects at room temperature, orders of magnitude lower required voltages, and an often less complex material and layer synthesis. [5,6,8]

In such voltage-gated magnetic nanostructures, the control of magnetic properties is mainly discussed with regard to two interfacial mechanisms, namely voltage-induced electrochemical reactions or electrostatic effects (capacitive effects). [1,6,7,9]

Electrostatic effects are by nature volatile and occur just in a few atomic layers in the case of metallic materials. In case of electrochemical reactions (or charge-transfer reactions) [6,7,10,11], chemical changes can affect magnetic properties beyond the interface and these changes can be non-volatile. [11–15] This makes electrochemical approaches promising for energy-efficient and voltage-programmable materials. [1] The application perspectives is fairly broad like in magnetic random access memory, domain wall logic, neuromorphic computing and magnetophoretic devices for e.g. lab-on-a-chip technologies. [1,16–18]

A general challenge for the electrochemical control of thin films is that the understanding of the underlying mechanisms is difficult. This is because the electrochemical, microstructural, and magnetic processes exhibit complex interdependencies, and at the same time they occur at the magnetic layer, which is buried under the solid or liquid electrolyte. To exploit the full potential of electrochemical control of magnetism, a fundamental understanding of the key mechanisms is required. So far, the interpretation of electrochemically induced effects is most often solely based on voltage-dependent magnetization curve changes, probed in situ via, e.g., superconducting quantum interference device magnetometry, [19] magneto-optical Kerr effect magnetometry [20,21] or anomalous Hall effect [20,22] setups.[1] Additional knowledge on the voltage induced impact on the magnetic domains, which underlies the

magnetization processes, would be an important step forward to disentangle the possible origins. The modulation of domain expansion [11,23], domain contrast [24] and domain size [25] after ionic modification of thin films are reported in a few cases, but the direct and simultaneous detection of electrochemical oxidation/reduction reactions and magnetic domain structure changes has not been reported so far.[1] In fact, latter reports [11,23–25] deal with ultrathin films and uniaxial anisotropy perpendicular to the film plane.

Voltage control of heterostructures, in contrast to single magnetic films, with additional functionality is highly desired. Additional functionality is achieved in ferro- or ferrimagnetic layers which share an interface with an antiferromagnet, giving rise to a unidirectional anisotropy or the exchange bias effect. The latter is also heavily used in existing nanomagnetic applications, as in hard-drives and magnetic sensors. Thus, the voltage control of exchange bias is of fundamental importance while the electrochemical approach for controlling exchange biased materials is still rather unexplored. [2]

Objectives of the thesis

The aims of this thesis are twofold:

1. To directly observe, for the first time, magnetic microstructure changes of magnetic thin films with in-plane magnetization in a liquid electrolyte during simultaneous voltage-triggered electrochemical reactions.
2. To demonstrate novel concepts on the tuning of exchange bias at room temperature based on electrochemical reactions

2 Fundamentals of magnetic thin films

Magnetic Microstructure and Magnetization Reversal

Landau and Lifshitz [26] found the driving force for the creation of the magnetic microstructure, or domains, to be the result of minimizing the total free energy. [27,28] In magnetic domains, the magnetization is uniformly aligned while this alignment strongly deviates in the domain walls. The creation of domains is governed by the stray field energy, exchange energy and anisotropy energy as well as possible Zeeman energy and magnetoelastic energy. [28]

The *stray field energy* is a magnetostatic energy term and originates from magnetic surface poles. It is also described as the demagnetizing energy evoked by the magnetic material itself. The stray field energy can further be described by the stray field coefficient K_d under the condition that the demagnetizing factor $N = 1$: [29]

$$K_d = 0.5 \cdot \mu_0 \cdot M_s^2 \quad (\text{Eq. 1})$$

with μ_0 being the vacuum permeability, M_s the saturation magnetization. Iron (Fe) has a stray field energy coefficient of $K_d = 1.8 \cdot 10^6 \text{ J/m}^3$.

In a ferromagnetic domain, the exchange energy is at a minimum when the magnetic spins are aligned parallel. The exchange constant of Fe is $A \approx 2 \cdot 10^{-11} \text{ J/m}$. [27]

The *anisotropy energy* describes the preferred alignment of the magnetic spins along distinct directions, so called easy axis. If the anisotropy energy appears to have uniaxial character, it can be described with the uniaxial anisotropy constant K_u which can be determined with:

$$K_U = 0.5 \cdot M_s \mu_0 H_A \quad (\text{Eq. 2})$$

where H_A denotes to the anisotropy field which can be determined from the hard axis loop. The quality parameter $Q = K/K_d$ classifies materials, if either the (uniaxial) anisotropy energy (K or K_U) or the stray field energy (K_d) dominates. If $Q > 1$ ($\ll 1$), the material of interest has a high (low) anisotropy.

For single crystalline materials, and in absent of any other anisotropy, the easy axes coincide with the principal axes of the crystal structure and is called *magnetocrystalline anisotropy*. [27] For instance, the easy axes for bcc Fe are the $\langle 100 \rangle$ directions.

In thin film geometries, the *shape anisotropy energy* promotes an in-plane alignment of the magnetization to avoid unfavorable stray fields. [28,30]

With reducing the ferromagnetic layer thickness, additional interfacial effects might dominate over shape anisotropy. Interfacial effects can lead to an easy axis which is normal to the film plane, giving rise to the *perpendicular magnetic anisotropy* (PMA).

Bloch and Néel Domain walls

The boundary between domains is called a domain wall. Domain walls are distinguished by the rotation of the magnetization in the wall relative to the magnetization alignment in the domain. In a Bloch wall (**Figure 2.1** (a)), the magnetization rotates out of the plane of the domain magnetization. In a Néel wall (**Figure 2.1** (b)), the magnetization rotates in the plane of the domain magnetization. [28]

Magnetic films with in-plane magnetization will experience a wall transition from Bloch to Néel walls according to **Figure 2.1** (c) as the film thickness decreases. **Figure 2.1** (b) shows the wall energy over the film thickness without an applied magnetic field. Néel walls are expected, with no applied field for film thicknesses below $12\sqrt{A/K_d}$ (grey dotted line in **Figure 2.1** c)). [29,31] The critical thickness for the Bloch-Néel transition in zero magnetic field for extended Permalloy thin films with a quality factor of $Q = 2.5 \cdot 10^{-4}$ can be calculated with:

$$12\sqrt{A/K_d} \quad (\text{Eq. 3})$$

Equation 3 can also be used for other material systems exhibiting a similar quality factor. [29] The driving force of this transition is to minimize the associated stray field energy by keeping Bloch walls with decreasing film thickness, as surface charges would develop above and below the wall. [29,31]. Néel walls becoming favorable as the film thickness decreases. As the Néel wall energy is proportional to the area of the charged surface inside the film, it decreases with decreasing film thickness. [31] As the energy of the Néel wall decreases, it increases its wall width until the energy contribution of the stray field is neglectable by reaching a small enough film thickness (see **Figure 2.1** (d)). In contrast, the stray field reduction for a Bloch wall results in decreasing wall widths as the film thickness decreases. [31]

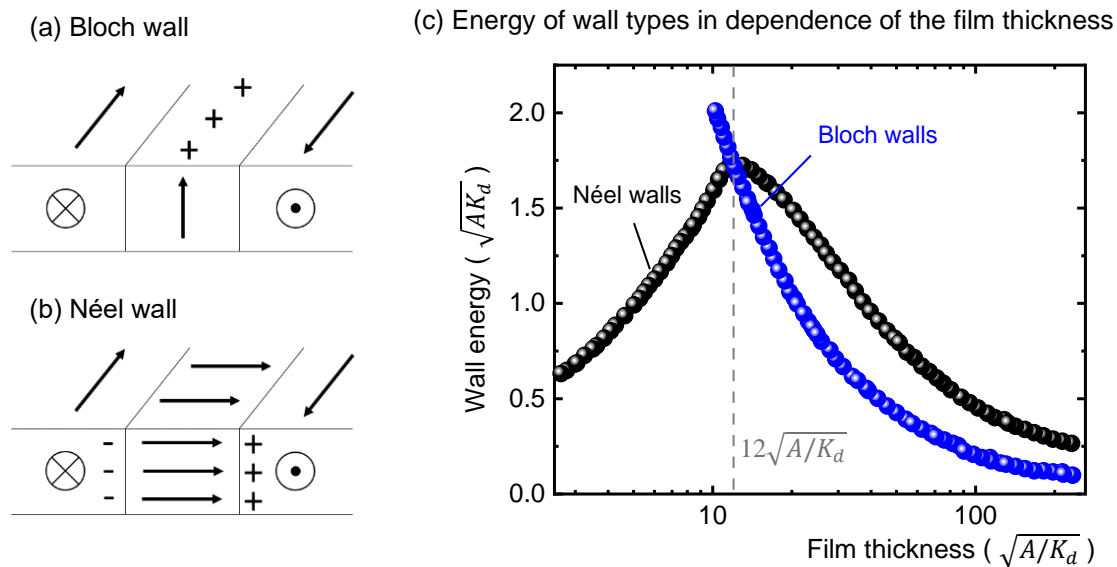


Figure 2.1: Characteristics of Bloch and Néel walls in thin films.

a) Bloch wall and b) Néel wall. c) Energy of different wall types in dependence of the film thickness ($H = 0 \text{ kAm}^{-1}$). The transition thickness from symmetric Néel walls to asymmetric Bloch walls is marked with a dotted line at $12\sqrt{A/K_d}$. Adapted by permission from [29] (Copyright 1998).

Surface energy density of a Néel wall

In a simple approach the Néel wall total energy can be approximated, for a perfectly flat surface, with: [31]

$$\gamma = A \frac{\pi^2}{a} + 0.5aK_u + 0.25 \left[\frac{ad}{a+d} \right] \mu_0 M_s^2 \quad (\text{Eq. 3})$$

where γ is the surface energy density, a denotes to the Néel wall core thickness and d is the film thickness. In the case of ultrathin films (film thickness \ll wall thickness), the wall core thickness a can be approximated as:

$$a \approx \pi \left(\frac{2A}{K_u} \right)^{1/2} \quad (\text{Eq. 4})$$

Charged Néel wall tails

A more realistic Néel wall consists, besides the relatively small core, of two relatively wide tails. **Figure 2.2** (a) depicts a Néel wall cross-section and the charge distribution, showing a dipolar charge of the core while each tail contains a single charge which is distributed over the tail width. The extended tails become especially important in thin films as they strongly interact due to their overlapping tails. For example, in Permalloy films of 50 nm thickness, the Néel wall tails interact over a distance of at least 100 μm . [29] For Néel walls, w_{tail} is determined between the magnetic charge distribution, described by the maximum stray field energy density (Kd) and the anisotropy energy (K_u): [29]

$$w_{\text{tail}} = e^{-\gamma'} d K d / K_u \approx 0.56 d K d / K_u \quad (\text{Eq. 6})$$

with $\gamma' = 0.577$ is the Euler-Mascheroni constant and d is the film thickness.

Two equivalent rotation senses of a domain wall exist and if both are energetically equal, a domain wall can contain both rotation senses. The position, at which these two parts are separated is called a Bloch line. In thin films with in-plane magnetization, the magnetization rotates either circular or cross like in a Bloch line. The center of a Bloch line is commonly magnetized perpendicularly to the film plane. [29]

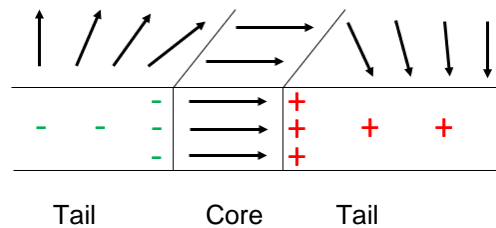


Figure 2.2: Néel wall decomposed in tails and core. Adapted by permission from [29] (Copyright 1998).

Magnetization process and Magnetization curve

The application of an applied magnetic field adds Zeeman energy to the ferromagnetic system. At a strong enough applied field, the magnetization will fully align with the direction thereof. This state is named saturation magnetization (M_S). [27] **Figure 2.3** shows the two principle magnetization processes based on a single domain wall element with uniaxial anisotropy and the magnetization aligned along the easy axis. In case the external field is applied along the hard axis, the magnetization uniformly rotates out of the easy axis (Figure 2.3 (a)). On the other hand, if the external field is applied along the easy axis, the magnetization changes via domain wall motion (Figure 2.3 (b)). [27] The wall motion is in accordance with increasing the volume of the magnetic domain which is favored by the applied field direction. [27] In real materials, smooth domain wall motion can be interrupted by defects which pin the wall where A or K differ from the value of the host magnetic material. The related magnetization curves along the hard axis (rotation of magnetization) and easy axis (domain wall motion) are shown in Figure 2.3 (c) and (d), respectively. The anisotropy field (H_A) can be deduced from the hard axis curve at the field where the magnetization saturates. Further, the area enclosed between the magnetization axis, zero field and the (positive) anisotropy field is a measure for the anisotropy energy density K , marked in Figure 2.3 (c). The field at which the magnetization becomes zero in an applied field is called coercivity (H_C). The remanence (M_R) is the magnetization in zero field after an external field, which saturated the sample, is removed. H_C and M_R are both marked in Figure 2.3 (d).

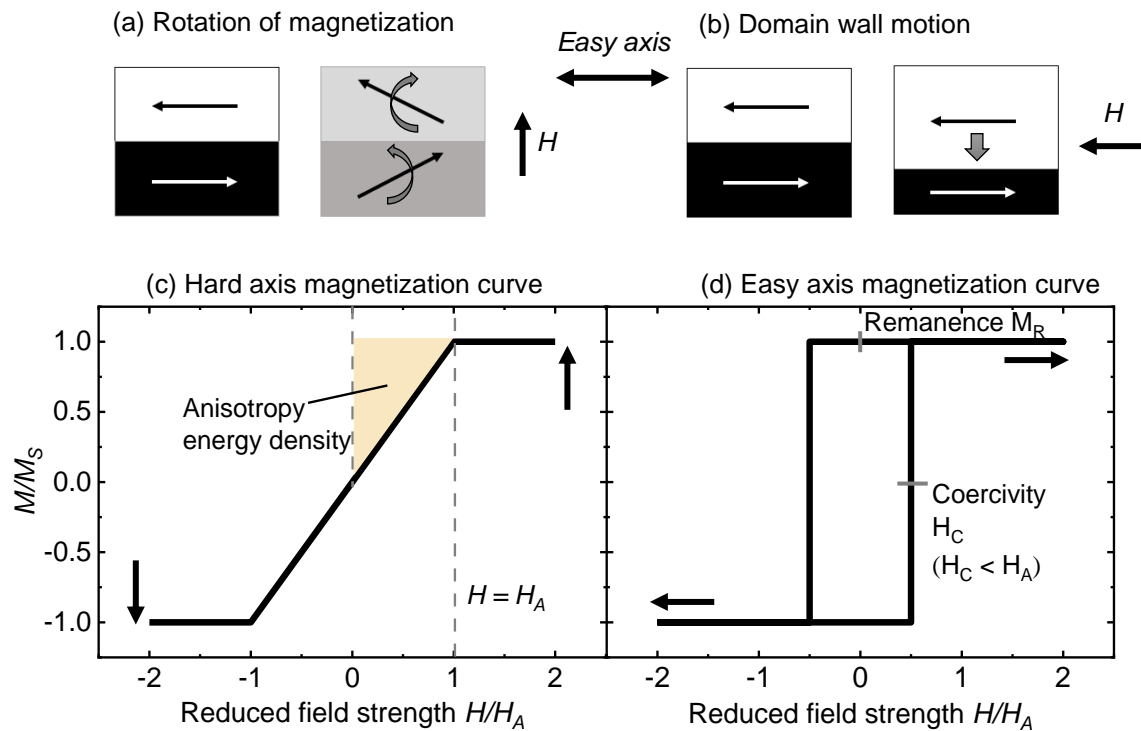


Figure 2.3: Typical magnetization processes in a material with uniaxial anisotropy.

(a) Uniform rotation of magnetization and (b) domain wall motion. The yellow area in (c) corresponds to the anisotropy energy density and H_A corresponds to the anisotropy field. The remanent field and the coercive field are marked in (d).

Exchange bias in thin films

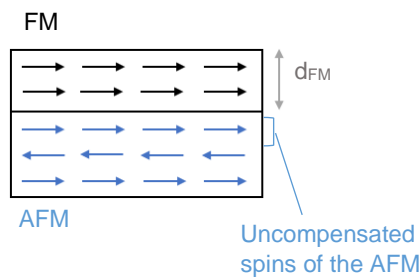
A distinct deviation from the aforementioned magnetic anisotropies is the unidirectional anisotropy in nanostructured ferro-/antiferromagnetic bilayers. [32–34] The unidirectional anisotropy manifests in a shift of the ferromagnetic magnetization curve along the magnetic field axis. The effect is due to the quantum mechanical exchange coupling [28,32] of interfacial magnetic moments in a ferromagnet to pinned uncompensated moments of an antiferromagnet (see **Figure 2.4** (a)). [34,35] The effect is also called exchange bias (EB) effect. The shift of the magnetization curve along the magnetic field axis, relative to zero magnetic field, is called the exchange bias field (H_{EB}) (see Figure 2.4 (b)). A prerequisite for establishing EB is that the Néel temperature of the antiferromagnet is below the Curie temperature of the ferromagnet. [34] Usually, EB can be initialized by a field cooling procedure, i.e. heating and cooling of a sample in an external magnetic field. Alternatively, the film fabrication in an external applied magnetic field can also initialize the EB. If the loop shift is opposite to the external magnetic field direction after the fabrication procedure, it is called negative EB. [34]

Usually, the H_{EB} shows a dependency on the ferromagnetic layer thickness (d_{FM}) as EB is an interface effect. This dependency can phenomenologically be expressed as in [36].

$$H_{EB} = -\frac{J_{EB}}{\mu_0 \cdot M_S(FM) \cdot d_{FM}} \quad (\text{Eq. 7})$$

This relation (Eq. 7) breaks down for either very thick or very thin ferromagnetic layers or if the film is not continuous. A second characteristic of EB systems beside the loop shift is the enhanced H_C which often inversely scales with the ferromagnetic layer thickness and H_C usually has about the same magnitude as H_{EB} .

(a) Characteristic EB layer system



(b) Characteristic magnetization curve of an EB system curve

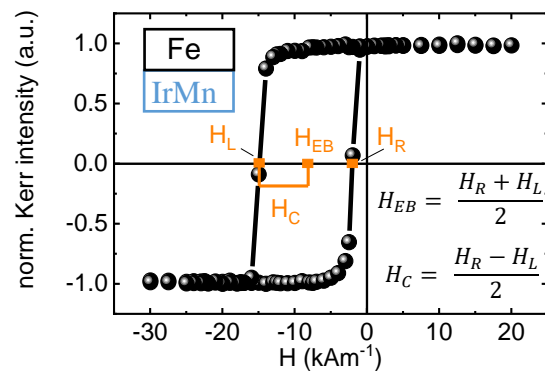


Figure 2.4: Characteristics of an exchange bias (EB) system.

a) Layer architecture with uncompensated spins of the antiferromagnet (AFM) at the interface to the ferromagnet (FM). b) Typical EB curve of a 13nm Fe/ 10 nm IrMn system with marked curve characteristics: H_{EB} and H_C . c) Thickness dependency of the exchange bias field in dependence of the ferromagnetic layer thickness.

Magneto-optical Kerr effect to characterize magnetism in thin films

The magneto-optical Kerr effect (MOKE) is used to characterize magnetic properties of thin films. The MOKE [37,38] is based on a rotation of the plane of linearly polarized light upon reflection from a magnetized specimen. On the other hand, rotation of linearly polarized light caused by transmission of a (magnetic) specimen in the presence of a magnetic field is called the Faraday effect. A phenomenological explanation of the MOKE can be made with the concept of Lorentz force. Let us assume that the magnetization direction of the sample is parallel to the surface and the light beam is inclined relative to the sample surface, see **Figure 2.5**. Linear polarized light with its electric field (**E**) component parallel to the magnetization direction (**M**) will be reflected in the same plane as the incident light (**R**). The electric field component perpendicular to the magnetization direction (here: perpendicular to the surface) will experience a Lorentz force (**v**) which causes an additional vectorial component to **R**, the Kerr amplitude (**K**). The superposition of **R** and **K** will lead to a magnetization dependent rotation of the electric field vector. The MOKE is a surface sensitive effect with an information depth on metal surfaces of about 25 nm. The MOKE requires a net magnetization component in the sample and thus ferro- and ferrimagnets can be probed but not antiferromagnets. [29] If the magnetization lies along the plane of incidence and parallel to the surface, it is called the longitudinal effect (as in Figure 2.5). The longitudinal mode is usually used to investigate samples with an in-plane magnetization. Samples with PMA can be measured in the polar mode at perpendicular incidence. [29]

A Kerr microscope and a laser-MOKE uses the MOKE to measure magnetization curves (laser MOKE and Kerr microscope) and to observe magnetic domains (Kerr microscope). In general, several techniques like Lorentz microscopy, magnetic force microscopy or the Bitter pattern technique would allow magnetic domain observation. However, choosing Kerr microscopy has some advantages over these techniques. In principle, no surface treatment is necessary and the contrast between differently magnetized domains can be digitally enhanced. Further, magnetization curves and magnetic domains can be captured within seconds. Taking this into account, Kerr microscopy becomes a flexible and efficient technique.

The aforementioned characteristics of magnetic materials are usually defined by the fabrication process and cannot be changed during usage. However, voltage control of magnetism might offer an elegant way for the reversible and energy efficient post-fabrication control of magnetic properties.

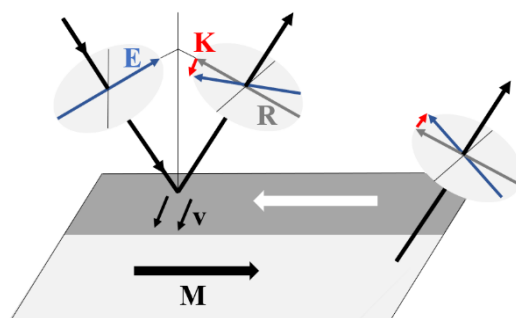


Figure 2.5: Magneto-optical Kerr effect in longitudinal geometry. Adapted by permission from [29] (Copyright 1998).

3 State of the Art

3.1 Voltage control of magnetism

Among other possible control parameters, such as electrical current, the voltage control of magnetism promises a low energy consuming alternative, as undesired Joule heating effects can be avoided. [5,39] Within this research field, the electrochemical control of nanoscale magnetism is a rapidly emerging topic. [5,6,9–11,20,21,40–43] In the following, we first describe different approaches on the voltage controlled manipulation of magnetism. Afterwards, we focus on the electrochemical control of magnetism in more detail.

Materials for voltage control of magnetism

Voltage control of magnetism can be broadly distinguished by the material class. The material classes are magnetic semiconductors, single-phase and two-phase multiferroic materials as well as nanostructured metals. [5] Capacitive effects in diluted magnetic semiconductors due to the application of a voltage leads to a modulation of the charge carrier density and results in a change of the ferromagnetic properties thereof. [44,45] Changes in H_C and M_R have been observed [44]. For the most prominent diluted magnetic semiconductor based on (In,Mn)As [44], the low Curie temperature (< 30 K) and complex fabrication procedures remain open challenges. Strain induced modulation of (ferro)magnetic properties can be achieved with single-phase and two phase multiferroic materials. Applying a voltage to single phase multiferroic, exhibiting magnetic and ferroelectric order at the same time, can trigger a change of the magnetic properties thereof. However, single-phase multiferroics are rare and their Curie temperature is usually below room temperature. [8,46] Applying a voltage on heterogeneous ferroic materials, e.g. bilayered ferromagnetic-ferroelectric materials, leads to a polarization of the ferroelectric material. Due to interfacial magneto-elastic coupling, the change in ferroelectric domains results also in a change of the ferromagnetic domains [8,47–51], see **Figure 3.1**. Nevertheless, multiferroics show disadvantages in their complex fabrication procedure and degrading interfaces during repetitive straining cycles. [6,9]

The following subsections will now focus on voltage control of ferromagnetic metal layers gated via a dielectric layer or an electrolyte. In comparison to magnetic semiconductors and multiferroics, these involved magnetic layers are usually easy to fabricate, e.g. often using room temperature deposition and polycrystalline materials. In addition, ferromagnets can be manipulated which exhibit a high Curie temperature and a high saturation magnetization saturation.

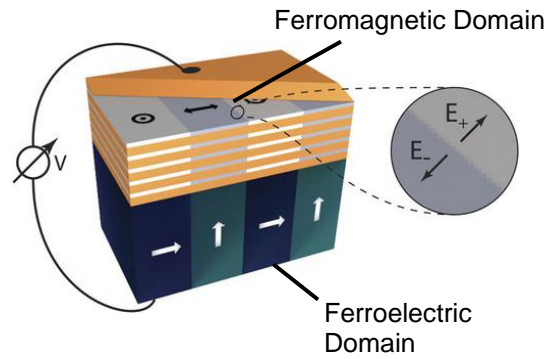


Figure 3.1: Illustration of ferroelectric/ferromagnetic magneto-elastic coupling. The alternating ferro-electric domains (white arrows) transfer strain to the ferromagnetic domains (black arrows) and causes their magnetization to rotate from in-plane to out-of-plane. Reprinted with permission from [48] under Creative Common Attribution (CC BY) license. (<https://creativecommons.org/licenses/by/4.0/>)

Architectures for voltage control of ferromagnetic metals by electrostatic or electrochemical effects

The principle device architecture for voltage control of ferromagnetic metals is shown in **Figure 3.2**. The structure contains the ferromagnetic metal layer, in contact with a solid-state dielectric layer or an electrolyte and a top electrode. The voltage is applied between the ferromagnetic layer and the top electrode. Two principle mechanisms are distinguished for changing the ferromagnetic properties. These are (i) voltage-triggered electrostatic effects (Figure 3.2 (a)) and (ii) electrochemical reactions (Figure 3.2 (b)), occurring at the ferromagnetic/electrolyte interface.

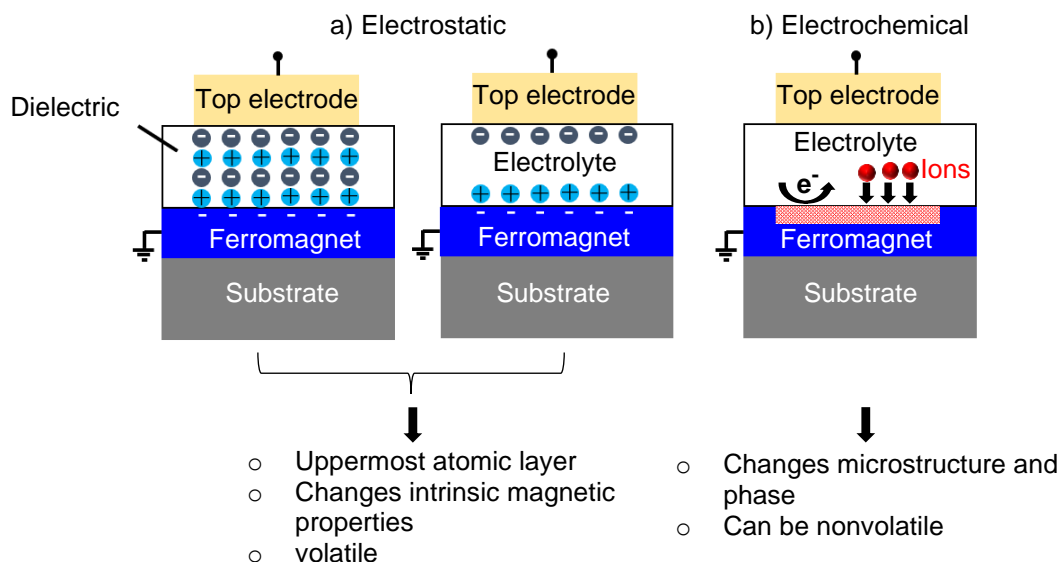


Figure 3.2: Common architectures to achieve magnetoelectric effects. a) Electrostatic effect in dielectric or electrolytic architecture and b) electrochemical reaction based on a change in oxidation state of part of the ferromagnetic layer (red bar)

Electrostatic effects (Figure 3.2 (a)), meaning charge accumulation or depletion at the surface of a ferromagnet can affect the intrinsic magnetic properties at the surface. [52] This can be achieved by either using a dielectric or an electrolyte.

However, the conduction electrons of the metal screen the applied electric field and limits the penetration depth of the applied electric field. In metals, the screening length is on the order of one atomic layer. Thus, only ultrathin nanostructured ferromagnetic metals, exhibiting a high surface to volume ratio, are accessible. [53] An overall characteristic of charge accumulation is the volatility of the induced magnetic changes.

Voltage control of ferromagnetic metals based on electrostatic effects

Electrostatic effects have been proposed as the origin for experimentally observed voltage induced changes in the magnetic anisotropy [54], coercivity [53], Curie temperature [55] or domain wall dynamics [56] and on EB [57,58]. The ferromagnetic materials are ultrathin (≤ 1 nm) FePt, FePd, Fe, Co, FeCo and FeCoB films. [54,57–62] Typical gate barrier materials are oxide layers with a high relative permittivity such as MgO, Al₂O₃ or HfO₂. [54,59–62] In addition, the voltage can also be applied via a liquid electrolyte or ionic liquid. [53,61] In these systems, the electrochemical double layer that forms in front of the ferromagnetic surface acts as a dielectric barrier layer that is only a few nanometers thick. [53,61,63] The voltage drop across a much smaller distance and larger electric fields are achievable, by a given external voltage, compared to solid oxide barriers, which are typically 50 nm thick to avoid the formation of pinholes. The enhanced electrostatic effects and lower required external voltages motivate the use of liquid electrolytes and ionic liquids films, sometimes in combination with an oxide layer measuring a few nanometers thick. [53,61,63–65]

Electrostatic effects on the magnetic microstructure has been demonstrated via Kerr microscopy. For this, a transparent or a thin enough dielectric or electrolytic layer was used in combination with a transparent top electrode, such as indium tin oxide. [65–68] Ultrathin films with perpendicular magnetic anisotropy were utilized to induce charge accumulated effects in FePt, CoFeB or Co thin films which results in changes of the nucleation and pinning sites, the wall velocity or the domain size. The observed electrostatic induced changes on the magnetic microstructure were caused by changes in the magnetic anisotropy. [61,65,66,68–70]

In an electrolyte, besides electrostatic effects, electrochemical reactions can be triggered by the external voltage. This will allow additional device functionalities. Indeed, the occurrence of charge transfer reactions were started to be realized as the magnitude of observed effects in voltage controlled electrolyte/magnetic film architectures exceeded those expected for charge accumulation. [21,64,71] Electrochemical reactions (Figure 3.2 (b)), e.g. voltage-assisted metal to metal-oxide transformations, enable the manipulation of larger film thicknesses. [6,9] Of additional advantage is the possibility to obtain non-volatile effects. [6,9,11]

3.2 Electrochemical control of magnetism

For electrochemical control of ferromagnetic thin films, solid-state oxide layers [11], liquid electrolytes [21] or a combination of both [72] have been proposed. As indicated in Figure 3.2 (b), the electrochemical control relies on a change in the oxidation state of the ferromagnetic material. The transferred charge during an oxidation or a reduction process is directly proportional to the transformed amount of material. For instance, for an oxide-metal transformation of a thickness d , where Me^{z+} are reduced to Me ($\text{Me}^{z+} + ze^- \rightarrow \text{Me}$), the charge density q can be calculated according to Faraday's law of electrolysis:

$$Q' = m \cdot z \cdot F \cdot (M)^{-1} \quad (\text{Eq. 7})$$

and

$$q = \frac{Q'}{A_A} = \rho \cdot d \cdot z \cdot F \cdot (M)^{-1} \quad (\text{Eq. 8})$$

where Q' is the electrical charge, m is the mass of the metal, ρ is the density of the metal, A_A is the layer area, F is the Faraday constant and (M) is the molar mass.

Within the presented thesis, liquid and solid-state electrolytes are utilized. In case of liquid electrolytes, an additional third electrode with a fixed potential (reference electrode) is used. The potentials, E , quoted in this work represent the potential of the working electrode (magnetic thin film) in Volt vs. the reference electrode. The formula symbol E for the electrode potential is chosen according to the IUPAC definition for electrochemistry, to avoid confusion please note that it is not equivalent to the electric field. [1]

A reference electrode is absent in the case of solid-state electrolytes and the term gate voltage, V_g in Volt, will be used instead.

Liquid electrolytes for voltage control of magnetism

Using liquid electrolytes requires electrochemical methods e.g., cyclic voltammetry for investigating the oxidization and reduction potentials. In a cyclic voltammogram, the potential of the working electrode is linearly swept, back and forth between two potentials, versus time. The current density at the working electrode is then plotted against the potential and the different obtained peaks in a cyclic voltammogram indicate different oxidation states of the working electrode.

For the electrochemical voltage control of magnetism using liquid electrolytes, large effects on the magnetization curve have been reported for the reduction and oxidation of FeO_x/Fe nanoislands using liquid alkaline electrolyte. [43] **Figure 3.3** (a) shows the cyclic voltammogram of a $\text{KOH}/\text{FeO}_x/\text{Fe}$ system. The reduction potential $E_R = -1.26 \text{ V}_{\text{SCE}}$ at which the reduction of Fe^{2+} to Fe occurs ($\text{Fe}^{2+} + 2e^- \rightarrow \text{Fe}$) and the

oxidation potential $E_O = -0.20 \text{ V}_{\text{SCE}}$ at which a passivation oxide forms, are marked. Figure 3.3 (b) show in situ anomalous hall measurements which reveal an almost complete voltage-induced on/off switching of the magnetism when the FeO_x/Fe nanoislands (Figure 3.3 (c)) are electrochemically reduced and oxidized.

Another vivid example for the control of magnetism within the liquid electrolyte approach can be seen in **Figure 3.4**. Di et al. investigated the influence of controlled surface-limited oxidation and reduction of electrodeposited Co (0001) (3.1 ML) on atomically flat Au (111). [73] Here, the development of the hysteresis loop is measured, via a laser-MOKE, at different potentials on a cyclic voltammogram, see **Figure 3.4** (a). At the starting potential at $E = -1.45 \text{ V}_{\text{MSE}}$, the film is in-plane magnetized. Sweeping towards more positive potential, the film becomes out-of-plane magnetized by reaching the first peak (P1 at $E = -1.16 \text{ V}_{\text{MSE}}$). This is due to the surface oxidation of the Co which is correlated to OH coverage (sketch in Figure 3.4 (b)). In the reversed sweep, towards more negative potential, the film becomes in-plane magnetized due to the oxide reduction, at $E = -1.34 \text{ V}_{\text{MSE}}$ which is correlated to a H adlayer (sketch in Figure 3.4 (c)).

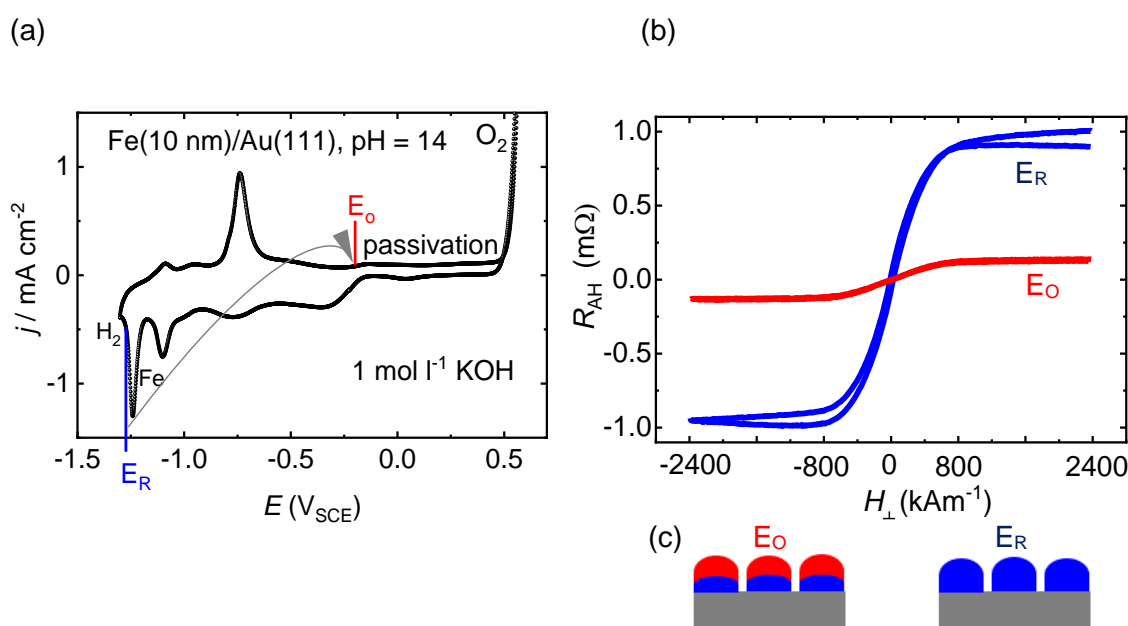


Figure 3.3: Electrochemical control of FeO_x/Fe films polarized in $1 \text{ mol l}^{-1} \text{ KOH}$.

(a) Cyclic voltammogram of FeO_x/Fe in $1 \text{ mol l}^{-1} \text{ KOH}$ solution. (b) In situ anomalous hall curves which show a close to on/off switching of magnetism. FeO_x/Fe nanoislands.

Adapted from [43] with permission from The Royal Society of Chemistry.

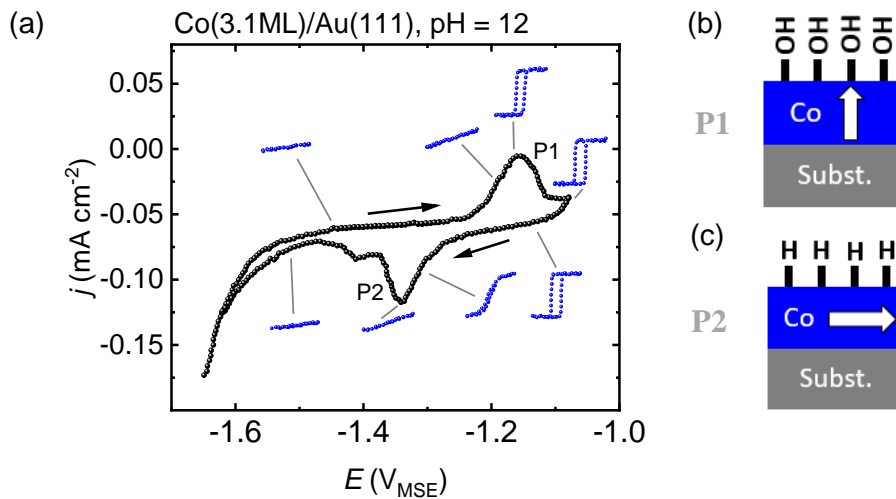


Figure 3.4: Electrochemical control of a Co thin film via surface reduction and oxidation. (a) Electrochemical transformation of the ferromagnetic layer. (b) Adsorption processes of hydrogen on a ferro-magnetic layer. Reproduced/Reprinted from [73], with the permission of AIP Publishing.

Solid-State electrolytes for voltage control of magnetism

Electrochemical oxidation and reduction can also be achieved within solid state structures. Among the used solid state electrolytes like HfO_x , AlO_x and MgO [64,74,75], GdO_x [11,42,71,76] takes a superior role for achieving electrochemical reactions in magnetic materials, as for instance a complete on/off switching of magnetization was first achieved with a solid state GdO_x electrolyte. [11,42] GdO_x is also used in the presented thesis to change the properties of thin magnetic films.

GdO_x is often utilized in a Pd/Co/GdO_x structure with perpendicular magnetization of the Co layer, shown in **Figure 3.5** (a). Oxygen ion migration was utilized in the $\text{Pt/Co/GdO}_x/\text{Au}$ at elevated temperatures, to oxidize the full volume of the Co layer [11], shown in Figure 3.5 (b). In the pristine state, the Co layer exhibits an out-of-plane magnetization curve (blue curve in Figure 3.5 (b)). Upon oxidizing at $V_g = -4$ V, the out-of-plane magnetization curve vanishes (red line in Figure 3.5 (b)).

The mechanism for magnetization switching can change in the same device structure by utilizing hydrogen accumulation at the Pd/Co/GdO_x interfaces. [20,77,78] The hydrogen based switching mechanism is shown in Figure 3.5 (c). In its pristine state, the Co layer is magnetized out-of-the film plane (blue magnetization curve in Figure 3.5 (c)) in order to switch to the hydrogen based mechanism, hydrated Gd(OH)_3 [78] is used and a water splitting reaction at the Au/Air interface is needed. It is thus mandatory to operate such a device in a humid environment. The current understanding of this mechanism is as follows: Upon the application of a positive gate voltage, water from the ambient surrounding is being split at the Au(anode)/Air interface ($2\text{H}_2\text{O} \rightarrow 4\text{H}^+ + \text{O}_2 + 4\text{e}^-$). The produced protons (H^+) are passed on from an OH^- to the neighboring O^{2-} ion inside the Gd(OH)_3 layer. When the protons reach the Pd/Co (cathode) interface, they become electrochemically reduced to atomic hydrogen ($4\text{H}^+ + 4\text{e}^- \rightarrow 4\text{H}$). The accumulated

hydrogen at the Pd/Co interface affects the hybridization between the Co and the Pd layer and leads to a switching of the magnetization in the film plane, see red line in Figure 3.5 (c). [20,77] After setting the external voltage back to 0 V, the accumulated hydrogen at the Pd/Co interface is being oxidized and removed from the Pd/Co/GdO_x interfaces by diffusing towards the GdO_x. Thus, PMA is being restored.

With the same hydrogen switching mechanism, the voltage control of a heavy-metal/ferromagnetic interface in an all solid-state structure was also achieved in Pd/Co/Pd/GdO_x. [20] In addition, the Pd layer between the Co and GdO_x is transformed into PdH_x upon the first application of a gating voltage [20], see **Figure 3.6**.

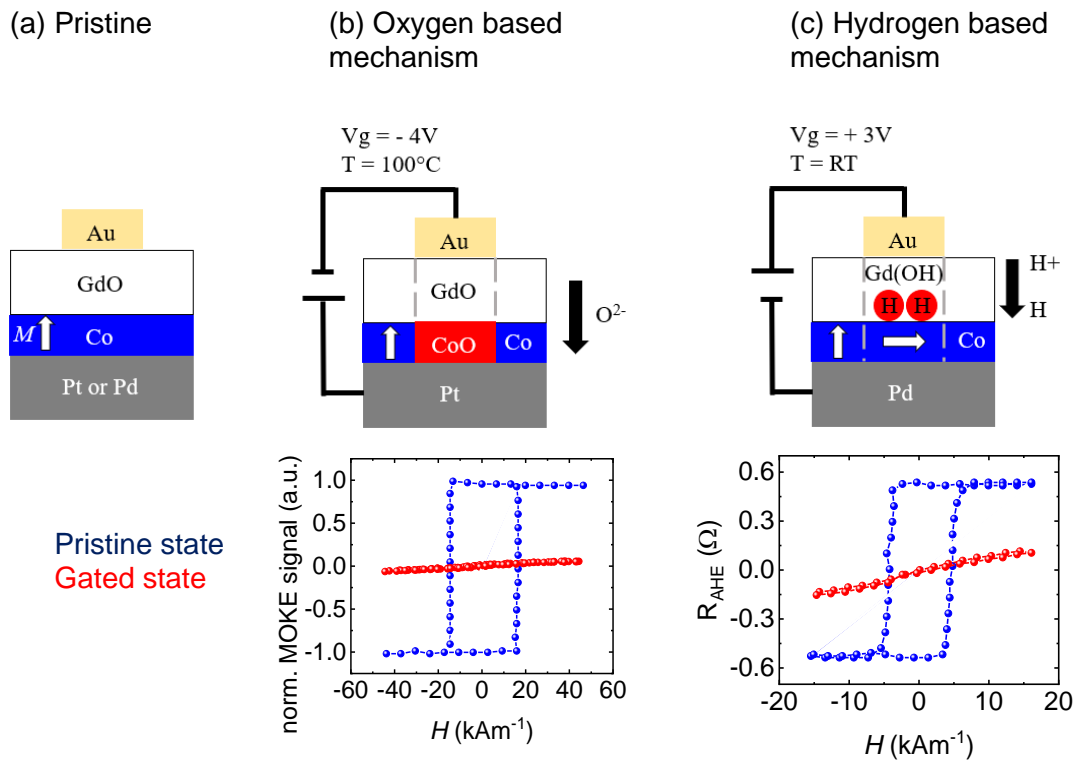


Figure 3.5: Co/GdO based architectures and switching mechanism of magnetization.

(a) Pristine structure. (b) Oxygen based switching mechanism. (c) Hydrogen based switching mechanism. The blue magnetization curves show the pristine state with an out-of-plane magnetization. Whereas the red lines show the magnetization curve after the gating voltage is applied. The magnetization curves in (b) are adapted by permission from [11] (Copyright 2015 <https://doi.org/10.1038/nmat4134>) and the magnetization curves in (c) are adapted by permission from [20] (Copyright 2019 <https://doi.org/10.1038/s41563-018-0211-5>).

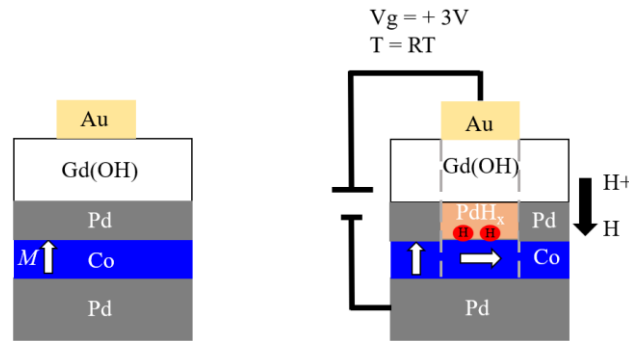


Figure 3.6: Hydration of Pd layer and magnetization switching.

Electrochemical control of magnetic domains

From a fundamental and application perspective, the understanding of the changes in the magnetization reversal, induced by an external voltage, is of crucial interest. So far, interpretations of underlying mechanism were mainly deduced from changes in the hysteresis loop. However, investigating the magnetic microstructure could be of additional benefit in understanding the underlying mechanism. To the best of the author's knowledge, only two publications [11,71] gave a glimpse on the subsequent impact on the magnetic microstructure during voltage control of magnetism based on charge transfer reactions. Both studies [11,71] utilize an oxygen based switching mechanism in the Pt/Co/GdO_x/Au structure. One example shall also be discussed here. [71] The experimental set up and the results can be seen in **Figure 3.7**. Without an applied electric field, the domain wall propagates undisturbed beneath the electrode perimeter (Figure 3.7 upper row). However, upon applying a voltage through the cylindrical electrode (-6V for 180s), the domain wall is pinned at the electrode perimeter (Figure 3.7 lower row). The phase change from Co to CoO, and thus a change in the magnetic anisotropy, hinders an undisturbed propagation of the domain wall. [71]

Pristine state

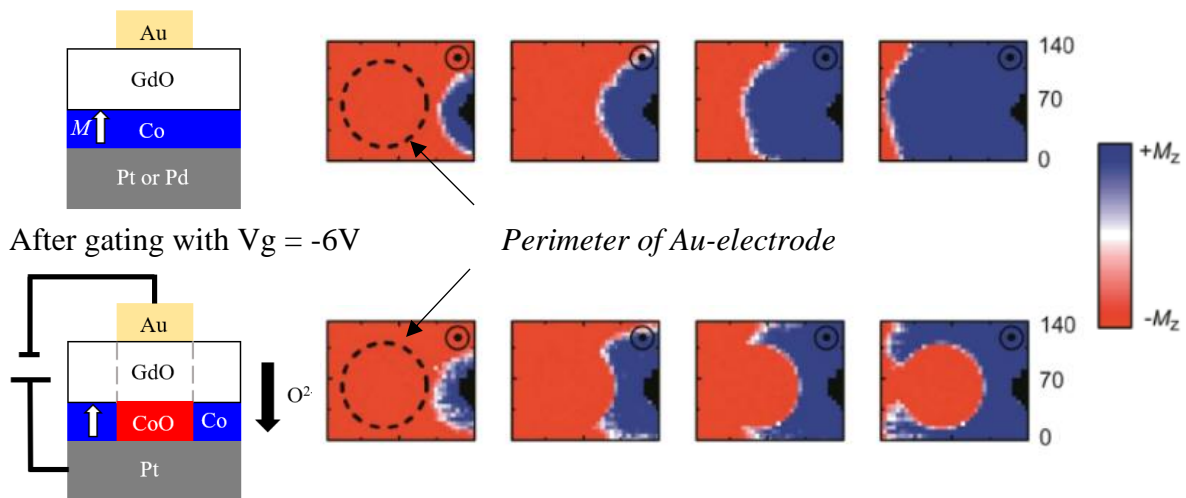


Figure 3.7: Co/GdO architecture and modulations of domain wall propagation. Adapted by permission from [71] (Copyright 2015 <https://doi.org/10.1038/nano.2013.96>).

Electrochemical control of the magnetic domain wall motion has also been achieved in architectures which utilize a combination of a solid-state and a ionic liquid [23,66] or using a liquid electrolyte [79]. However, in all cases, the observations were made on Co-based thin films with perpendicular magnetic anisotropy. No reports are available which investigate the influence of electrochemical reactions on the magnetic microstructure of samples with in-plane magnetization.

Voltage control of exchange bias

Mainly thermal treatments like field cooling or ion bombardment are utilized to achieve irreversible changes in the antiferromagnet in order to control the EB properties. [34,80,81] In contrast, voltage control of the EB offers an alternative way of tuning these properties at room temperature. Indeed, a first result on isothermal switching of EB via a voltage was achieved in a ferroelectric antiferromagnet (Cr_2O_3) combined with a ferromagnetic layer. [82] Latter concept was further exploited by utilizing different ferroelectric antiferromagnets (BiFeO_3 [83] or YMnO_3 [84]) and multilayered multiferroic heterostructures. [84–86] Multiferroics require a special crystal structures, often low temperatures or extremely high electric fields. [85,86] An alternative topical approach towards low-voltage electric control of magnetic properties of thin films is based on charge accumulation or charge transfer reactions, but reports on the control of EB are scarce in this field. [6,9,57,58] Wang et al. achieved the electric modulation of EB by ionic liquid gating of the [Co/Pt]/IrMn system and explained it by the injection and extraction of electrons in the antiferromagnetic layer. [57] The EB effects in this case are restricted to low temperatures (10–100 K), because the electronic charging is significant only in very thin IrMn films (≤ 5 nm) which exhibit low blocking temperatures. [57] One first report addresses $\text{NiCoO}_x/\text{NiCo}$ interfaces, in which irreversible EB changes are induced by oxygen ion diffusion and interfacial reduction/oxidation reactions via temperature control. [40] First attempts to voltage-control EB via ionic mechanisms involve topographically patterned elements consisting of a cobalt layer in contact with a CoO_x or HfO_x antiferromagnetic layer that exhibits resistive switching. [87–89] The voltage-dependent EB is interpreted based on a resistive switching mechanism, involving the formation and rupture of conducting filaments in the antiferromagnet and associated dynamic atomistic rearrangement of the antiferromagnet/ferromagnet interface. Analogous to the high and low resistance states set by resistive switching, the voltage can only toggle between two states possessing different EB fields. Moreover, the choice of materials is strongly limited because specific oxides are required for the antiferromagnetic layer. Consequently, effects are only reported for small EB values and partially shifted magnetization curves. [2]

4 Methods

4.1 Film fabrication

The films were deposited via sputtering which is a physical vapor deposition technique. During the sputtering process, the inert working gas is ionized and the charged particles are accelerated towards the target. This leads to the ejection of the target material which is deposited onto the substrate. The sputter process is done in a vacuum chamber. For the deposition of Co and Fe, magnets were placed behind the target, which is negatively charged, to trap electrons. This results in faster deposition rates and is called magnetron sputtering. In addition, other gases besides the working gas can be inserted during the sputtering process which undergo an electrochemical reaction with the deposited material. For example, oxygen gas can be added to form a metal-oxide thin film, e.g. GdO. Further, more than one target material can be deposited at once, if the desired film should be an alloy, e.g. sputtering Co and Gd at once to form a CoGd alloy. [90] The film systems which are investigated within the presented theses were deposited in different sputtering chambers.

The FeO_x/Fe/Au films: For this work, we sputtered thin films of Fe (8 nm)/Au (13 nm)/Cr (3 nm) on SiO₂ (100 nm)/Si substrates with an area of 10 mm x 10 mm. The targets were aligned under an incidence angle of 45° with respect to the substrate normal. Cr was used as adhesion layer and Au to ensure good film conductivity. The base pressure was 2x10⁻⁸ mbar and 2% ArH was used as sputtering gas. The deposition took place at room temperature. The deposition rates were measured with a quartz crystal before depositing the film. The native oxidation of the Fe surface was initiated by exposing the sample to ambient condition.

The FeO_x/Fe/IrMn films: Exchange bias thin film systems consists of a 5 nm Au (buffer layer), 10 nm Ir₁₇Mn₈₃ (antiferromagnet) and a top Fe (ferromagnet) layer with different nominal thicknesses $d_{\text{Fe,nom}} = 5, 7, 9, 11, 13$ nm were deposited on thermally oxidized Si(100) substrates with an area of 10 mm x 10 mm by rf-magnetron sputtering at room temperature (base pressure was 10⁻⁷ mbar and the working pressure under continuous argon flux was 10⁻² mbar). [2] The sputtering rate was determined beforehand via step measurements by using atomic force microscopy. During the sputtering procedure an external magnetic field of 28 kAm⁻¹ was applied parallel to the sample plane to set the initial ordering state within the antiferromagnetic layer, i.e., a preferred alignment of the local unidirectional anisotropy. After removal from the vacuum chamber, a native FeO_x layer formed on the Fe layer. [2]

The FeO_x/Fe/IrMn exchange biased samples were fabricated by Rico Huhnstock at the University of Kassel.

The Co and GdCo films: Films with layer architecture of Ta (3 nm) / Pd (10 nm) / NiO (30 nm) / Pd (0.2 nm) / Co (0.9 nm) / Pd (5 nm) / GdO_x (10 nm) / Au (8 nm) and Ta (3 nm) / Pd (10 nm) / NiO (30 nm) / Pd (0.2 nm) / GdCo (6 nm) / Pd (5 nm) / GdO_x (10 nm) / Au (3 nm) were fabricated by sputtering. For deposition, the thermally oxidized Si/SiO₂ substrate was mounted on a 1x1 cm² flat permanent magnet with a magnetic field of 2.8 kOe with the magnetic north pole perpendicular to the substrate surface. The layers were deposited by dc magnetron sputtering at room temperature at 3 mTorr Ar pressure. In addition, the oxide layers were deposited via dc reactive sputtering with a partial oxygen pressure of 0.07 mTorr. Before depositing GdO_x, a corner of the film was covered to serve as contact for upcoming gating experiments. [3] The deposition rate was measured beforehand via X-ray reflectivity by Sara Sheffels (MIT). Hydration of the GdO_x into Gd(OH)₃ followed the procedure described in [78] at 70°C whereas the sample sit at distance of about 2 cm above the heating plate. Circular Au electrodes with a diameter of 200 μm and about 8 nm in thickness were patterned via a shadow mask and dc magnetron sputtering on top of the continuous film. [3]

A second film set of samples utilized the ferrimagnet GdCo as the functional layer. The same layer architecture and procedure as mentioned above are used. Except, the Co (0.9 nm) was replaced by GdCo (6 nm), whereas Gd and Co were sputtered at the same time.

4.2 Ex-situ and in-situ analytical characterization

Transmission electron microscopy

Transmission electron microscopy (TEM) was used to probe the microstructural, morphological, structural and compositional appearance of the films. In a TEM, highly accelerated electrons are directed at a very thin specimen. [91] The differently scattered and transmitted electrons can be used to form an image. For bright field imaging, an aperture is inserted which blocks the strongly scattered electrons. In the bright field case, the intensity of scattering is dependent on the mass and the thickness, which gives rise to the so called mass thickness contrast, as well as on the relative orientation of the crystal lattice and the electron beam, which gives the diffraction contrast. [91,92]

In order to chemically analyze the sample, energy-filtered transmission electron microscopy (EFTEM) is used. In EFTEM, electrons with characteristic kinetic energies are selected for image acquisition. The obtained energy-filtered images hold information of the chemical element in the sample.

The preparation of the cross-section lamellas was carried out via focused ion beam technique on a FEI Helios Nanolab 600i using 30 and 4 kV Ga⁺ ions. Further thinning of the lamella was performed in a Gatan PIPSII with 0.2 kV Ar⁺ ions. The lamellas were prepared by Almut Pohl and Tina Sturm, both IFW Dresden

The FeO_x/Fe/Au films: High resolution transmission electron microscopy was conducted on a double-aberration-corrected FEI Titan3 80-300 microscope to investigate the architecture and microstructure of the film. The crystallographic orientations of the layers were

determined by performing a fast Fourier transform in the Gatan Microscopy Suite of the respective sample areas. [1]

The TEM was operated by Dr. Sebastian Schneider (IFW Dresden).

The FeO_x/Fe/IrMn films: The layer architecture and microstructure were characterized by TEM (FEI Tecnai G2, acceleration voltage 200 kV, field-emission). [2] The TEM was operated by Dr. Ulrike Wolf (IFW Dresden).

The Co and GdCo films: TEM was used to characterize the architecture and microstructure. To conduct qualitative elemental mapping, we carried out energy-filtered TEM (three window method) using a post column Gatan imaging filter (GIF Trideiem, Gatan, Inc., US). We thereby exploited the inner-shell electrons excitations of respective elements by the highly energetic TEM beam electrons. For example, we used for mapping Pd the M_{4,5} edge at 335 eV, Co the M_{2,3} edge at 60 eV, and Ni the M_{2,3} edge at 68 eV. [3] The TEM was operated by Dr. Daniel Wolf (IFW Dresden).

X-ray photoelectron spectroscopy

X-ray photoelectron spectroscopy (XPS) was used to investigate the chemical states of Fe, in FeO_x/Fe/IrMn thin films, before and after electrochemical treatment. XPS is based on the photoelectric effect. The material under investigation is exposed to (high) energetic radiation (X-ray's) which will lead to the ejection of photoelectrons from the electron shells of the material. The final analysis of the kinetic energy of the liberated photoelectrons holds information of the chemical states.

XPS was conducted at a PHI 5600 CI (Physical Electronics) spectrometer. The pass energy of the hemispherical analyzer amounts to 29 eV. Monochromatic Al-K α excitation (350 W) was used. The information depth of the measurements was varied by changing the angle between analyzer and sample surface (values are given with respect to the sample surface). The analysis area had a diameter of $\approx 800 \mu\text{m}$. [2]

XPS was conducted by Dr. Steffen Oswald (IFW Dresden).

Ex-situ and in-situ Raman spectroscopy

In situ Raman spectroscopy was used for the chemical identification of FeO_x. The principle is based on the interaction of the incident laser light and the chemical bonds of the material of interest. The incoming laser light is scattered at the sample surface at different wavelengths which hold information about the chemical structure of the analyte. Raman spectra were recorded on a T64000 triple spectrometer (Jobin Yvon) Horiba, equipped with a diffraction grid of 600gr/mm and a 532 nm excitation wavelength of a Torus 532 laser (Laser Quantum). The ex situ measurements were carried out with a Leica PL FLUOTAR 50x objective and with the laser power adjusted to less than 7.4 μW (laser spot diameter of 20 μm on the sample). [93] An UMPlanFLN 20XW Olympus water immersion objective was used for the in-situ measurements. E was applied by the potentiostat in a two-electrode configuration. [1]

In-situ Raman experiments were conducted under the supervision and with assistance of Sandra Schiemenz and Frank Ziegls, both IFW Dresden.

In situ Rutherford backscattering

In-situ Rutherford backscattering measurements (RBS) were conducted to investigate the thickness and the layer stability in contact with the electrolyte of FeO_x/Fe/Au samples. [1] In a RBS experiment, high energetic ions with a low mass (e.g. Helium) are shoot on the sample. The ions penetrate the material and the energy of the backscattered ions are detected. The obtained, and characteristic, energies of the backscattered ions can be converted into a spectra which allows to determine the elements of the film and the thickness thereof. The layered film was deposited on a Si₃N₄ window with a thickness of 500 nm. The different substrate is expected not to affect the film properties as both, Si₃N₄ and SiO are amorphous. The substrate was attached to the beamline instrumentation in such a way that the backside faced vacuum (10⁻⁶ mbar) and the Fe layer faced either air or the electrolyte by using a special in situ cell [94]. The He⁺ ion beam of 1.7 MeV energy was generated by a 2 MV van de Graff accelerator and guided via switching magnets towards the sample. The obtained spectra were evaluated using SIMNRA [95] software. [1] The voltage was applied with the assistance of a SP-50 BioLogic potentiostat. In situ RBS measurements were conducted under the supervision and with assistance of René Heller and Nasrin B. Khojasteh (both HZDR).

4.3 Electrochemical characterization

Electrochemical procedures

Electrochemical operations with liquid electrolytes: The electrochemical reduction and oxidation for the FeO_x/Fe systems was conducted in a cell made out of polyether ether ketone in a three-electrode array. Cyclic voltammetry (CV) is an electrochemical characterization method for identifying oxidation and reduction potentials of an electrochemical system. The applied potential is swept while the current is recorded.

In chronoamperometry (CA), a fixed potential is applied to the ferromagnetic layer and the resulting current is recorded over time.

A 1 mol l⁻¹ LiOH aqueous solution was used as electrolyte. The FeO_x/Fe thin film samples were connected as the working electrode, while platinum wires served as counter- and reference electrodes. The potentials, E , quoted in this work represent the potential of the magnetic thin film in Volt vs. the platinum reference electrode. The formula symbol E for the electrode potential is chosen according to the IUPAC definition for electrochemistry, to avoid confusion please note that it is not equivalent to the electric field. The application of E and the measurement of the $j(E)$ characteristics were performed with a potentiostat (Biologic SP50). [1]

Electrochemical operations with solid electrolytes: Electrochemical cells utilizing a solid-state electrolyte, such as GdO_x, are usually operated in a two electrode array. Reference electrodes are usually absent, because of very difficult design requirements. [96] Thus,

solid-state devices operate in a two electrode configuration. The applied potential thus equals the cell voltage.

The voltage was applied by using a Keithley 6430 source meter and a Lakeshore CPX-VF probe station with CuBe probes.

4.4 Magneto-optical Kerr Magnetometry and Microscopy

The evaluation of magnetic properties is examined via the magneto-optical Kerr effect (see Figure 2.5). Within the frame of the presented thesis, a wide-field Kerr microscope and a laser-MOKE has been used. A Kerr microscope is typically used to image the magnetic microstructure as it allows for imaging a wide area on the sample surface (up to cm^2). In contrast, a laser-MOKE has only a small spot size (in the range of μm^2) which needs to raster across a larger sample area in order to image the magnetic microstructure.

Kerr microscopy

Wide-field Kerr microscopy was used to investigate samples with in-plane magnetization. This includes measurements of magnetization curves and the imaging of magnetic domains. A principle sketch of the elements of an advanced Kerr microscope with the beam paths is shown in **Figure 4.1**. “The Kerr microscope is based on an optical polarization reflection microscope that applies the Köhler illumination technique to obtain homogeneously illuminated images.” [97] The light is emitted from white LEDs. A polarizer in the illumination path linearly polarizes the incoming light. The linearly polarized light is guided via a beam splitter and an objective to the sample surface. Upon reflection, the light passes through the beam splitter and a second polarizer, called analyzer, which is used to extinguish the light of one magnetic domain direction. The opposite magnetic domain direction appears brighter on the camera image. A compensator in the image forming path can be optionally installed to correct the elliptically distorted light. A camera is used to visualize the magnetic domains.

The light of 8 LEDs is guided independently to the microscope via glass fibers, which ends are arranged in a conoscopical plane in a cross-like manner. The sensitivity direction of the microscope depends on the incident direction of the incoming light. Thus, the conoscopical arrangement allows to adjust the light incidence direction for probing the desired magnetization direction. **Figure 4.2** (a) exemplifies the selection of LEDs for the longitudinal mode to image magnetization directions. Two orthogonal incidences, as shown in Figure 4.2 (a), can be combined to either image magnetic domains or domain walls at the same sample area, which is shown in Figure 4.2 (b).

A contrast enhancement among the magnetic domains can be achieved by subtracting two domain images obtained with opposite light incidence (see Figure 4.2 (c)).

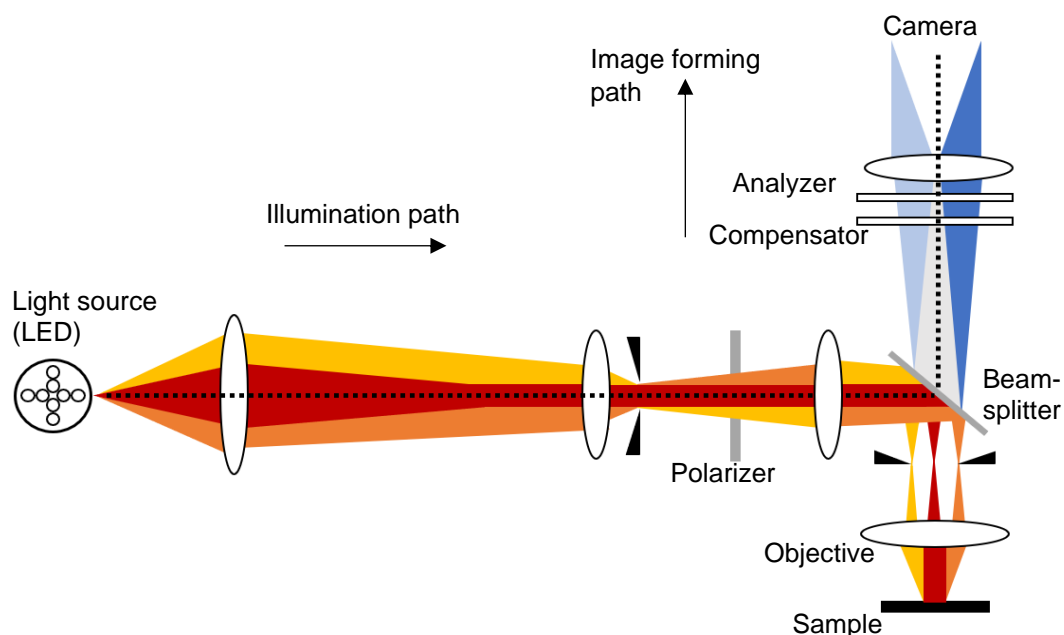


Figure 4.1: Illumination and image forming path.

The basic parts are named. Adapted from [97], with the permission of AIP Publishing.

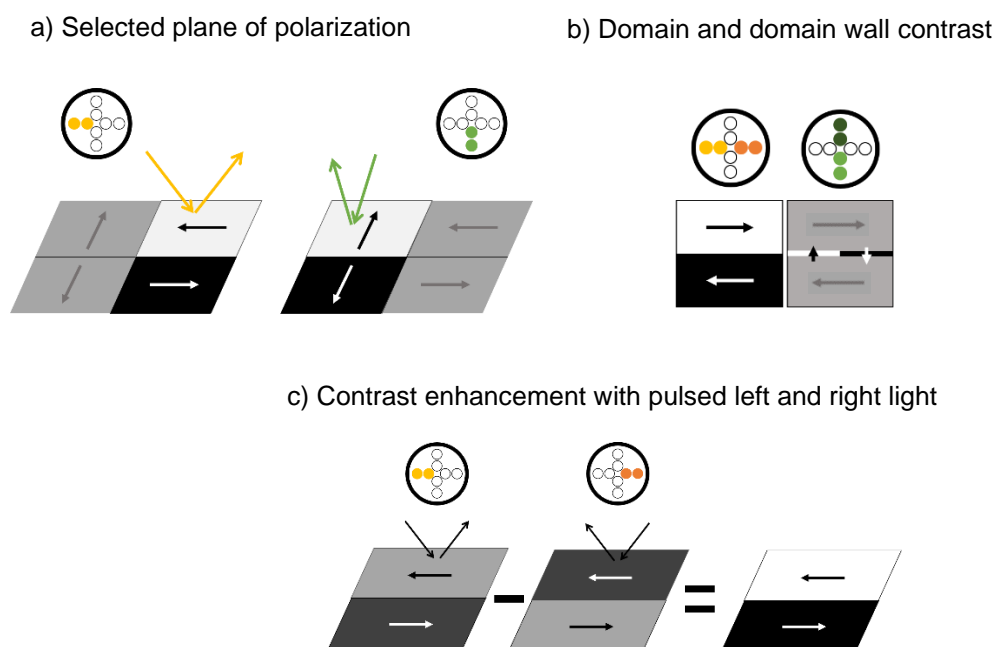


Figure 4.2: Influence of selected light sensitivity on the magnetic domain contrast.

a) selected plane of polarization is sensitive to different magnetization directions. b) domain and domain wall contrast. c) contrast enhancement with selective light pulses with oblique incidence from left and right. Inspired and adapted from [97], with the permission of AIP Publishing.

An additional way of contrast enhancement is offered by digital means [98] which is shown in **Figure 4.3**. First, a background image is recorded while the sample is saturated. This background image is subtracted from images during the magnetization reversal which removes any non-magnetic signal, such as the topography. As a result, the magnetic domains can be seen more easily.

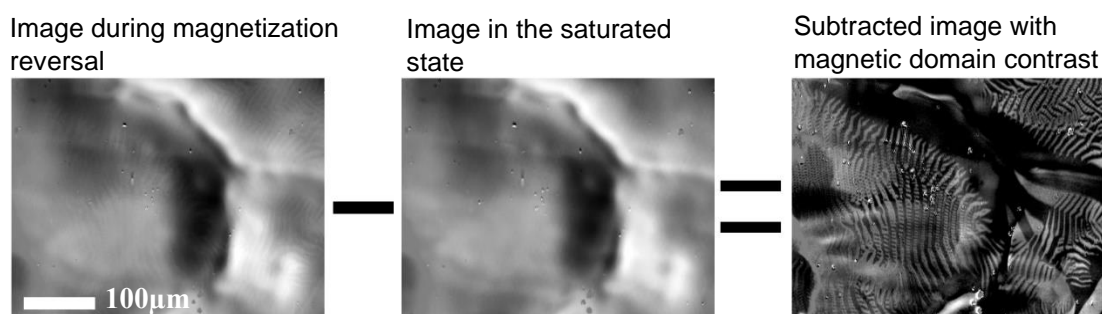


Figure 4.3: Digital contrast enhancement.

The combination of a Kerr microscope with an electrochemical cell is part of the presented thesis and will be described in chapter 5.

Laser-MOKE

Laser-MOKE was used to investigate samples with perpendicular magnetization and solely for measuring magnetization curves. Here, a polar rotation geometry, in which the light is coming perpendicular to the surface, was used. A laser-MOKE setup consists, similar to the Kerr microscope, of an incident polarizer, an analyzer and a photodiode detector. A 2.5 mW laser with a wavelength of 660 nm (red) was used as the light source. In order to conduct gating experiments on the solid state samples, a probe station was adjusted to the setup. The gate voltage was applied via a CuBe probe near the edge of the circular Au electrode and another CuBe probe landed on the previously covered Ta/Pd/NiO/Pd/Co/Pd layer. All experiments were performed at room temperature. The temperature of the iron yoke of the magnet was constantly monitored, with the help of an attached thermocouple, and stayed at 26°C (+/-1°C) during the measurements. The $M_R/M_{1000 \text{ Oe}}$ ratio was determined by normalizing each loop and taking M_R from the ascending field branch of the magnetization curve.

5 Combining Kerr microscopy and electrochemistry – the in situ cell

In order to carry out a combined electrochemical and magnetic analysis, an electrochemical cell, suitable for a Kerr microscope, has to be developed. This method is named in-situ Kerr microscopy. In this chapter, the design and the construction of the electrochemical cell used for in-situ Kerr microscopy will be presented.

Design requirements for the in situ cell

In order to conduct combined electrochemical and magnetic experiments, an electrochemical cell has to be designed which with a Kerr microscope. This cell has to offer sufficient space for the electrolyte and electrodes as well as space to connect the electrodes of the cell via cables to a potentiostat. At the same time, the cell has to fulfill the space restrictions given by the Kerr microscope. The cell width is restricted by the magnetic pole shoes (maximum diameter of 50 mm). The height of the cell should be in accordance with the working distance of the objective (maximum of 3 mm). Also, the cell has to offer the possibility to place a glass slide on top of the cell which will give a plane surface of the electrolyte and thus allows for proper microscopical operations. The competing space requirements for the cell, to allow electrochemical experiments (“as large as possible”), and the space restrictions given by the Kerr microscope (“as small as possible”) have to be optimally considered.

Additional requirements for the Kerr microscope

The Kerr microscope has to be equipped with an objective being able to compensate for the changes in refractive index arising from the cover glass and the electrolyte. In addition, the objective lens must still be able to guide polarized light. For this, a long-distance objective (ZEISS ACHROPLAN with 40x magnification) with a collar ring was used. This makes it possible to focus on the sample surface at a distance of 3 mm between the sample surface and the objective.

Cell realization

Figure 5.1 shows the electrochemical cell, which fulfills the design requirements for in-situ Kerr microscopy. The cell bottom and top piece are fabricated out of polyether ether ketone (PEEK), which is stable in alkaline electrolyte of pH 14. The bottom piece of the cell carries the sample (Figure 5.1 (a)) and has electrical contacts. The contacts for the electrodes are made out of CuBe to ensure a low contact resistance. The top piece, including the overflow container for the electrolyte, can be screwed on the bottom piece (Figure 5.1 (b)) while the sample is in between. The Pt-wires acting as pseudo-reference and counter electrode are placed on the lid and are electrically connected to the CuBe contacts (Figure 5.1 (b)). The Pt-wire electrodes will also stay later in contact with the electrolyte. Figure 5.1 (c) shows the electrical connection of the cell with the cables from the potentiostat.

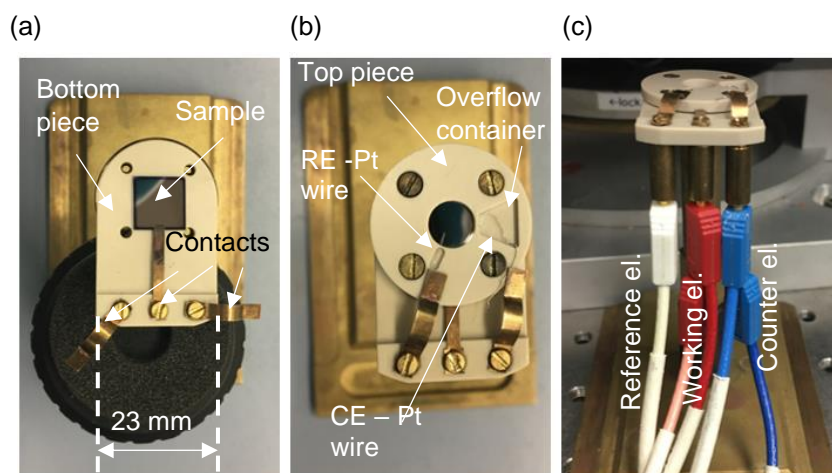


Figure 5.1. In situ electrochemical cell for the Kerr microscope
 (a) Bottom of the cell and electric contact to the sample. (b) Top piece with overflow container on the bottom piece and connection of the Pt wire as reference and the counter electrode, RE - reference electrode, CE – counter electrode. (c) Connection of electrodes with the potentiostat at the bottom of the cell.

Figure 5.2 shows the cell placed in the Kerr microscope set up. Figure 5.2 (a) shows how the electrolyte is filled into the cell (not shown for the overflow container). The cell can contain 100 μl of electrolyte in the inside in combination with an additional overflow container. The cover glass is placed on top of the cell (Figure 5.2 (b)). Figure 5.2 (c) shows the cell placed between the magnetic poles and the objective above.

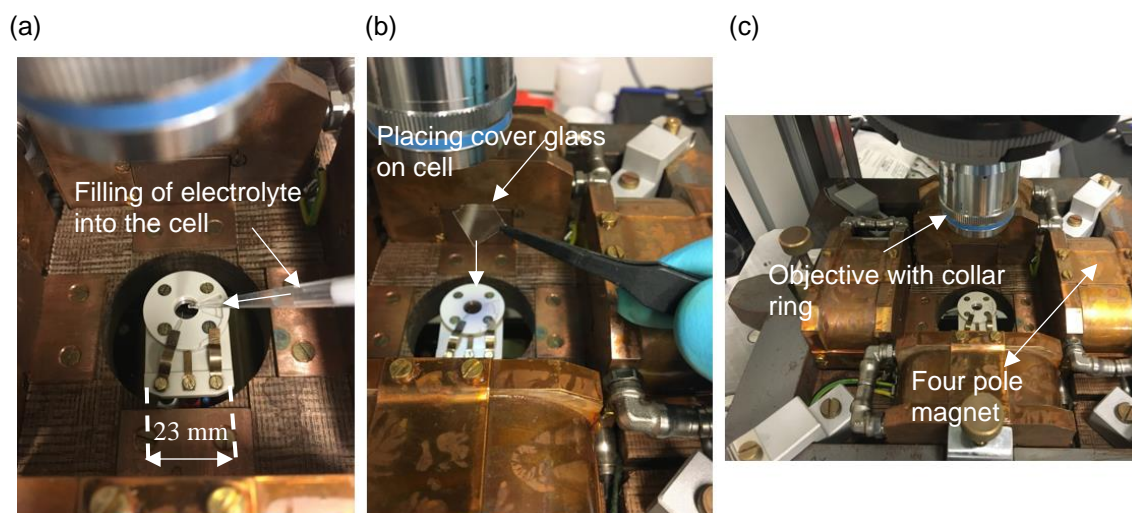


Figure 5.2. In situ electrochemical cell combined with the Kerr microscope.
 (a) Filling of electrolyte into the electrochemical cell. (b) placing of cover glass on the cell. (c) fully assembled set up for in situ investigations.

Electrochemical cell operation and limits

In a first step, the correct electrochemical operation of the cell was tested via cyclic voltammetry. For this, the cell was assembled into a three-electrode array. Pt wires served as reference- and counter electrode. An FeO_x/Fe/Au sample served as working electrode and 1 M of LiOH was used as electrolyte. The recorded cyclic voltammogram in **Figure 5.3** has a comparable shape as the cyclic voltammogram in Figure 3.4 which demonstrates the electrochemical functionality of the cell. The cyclic voltammogram in Figure 5.3 shows three cathodic peaks (Ia, IIa, IIIa) and three anodic peaks (Ic, IIc, IIIc) and a passivation regime. The electrochemical reactions which take place at the different anodic and cathodic peaks are listed in the inset of the cyclic voltammogram in Figure 5.3 and a listing of the occurring reactions can be found in [99].

Conclusion

In summary, the home-built electrochemical cell, fulfills all the requirements arising from electrochemical side and the microscopical side. The combination of the electrochemical cell with the Kerr microscope will be named in situ Kerr microscopy or in situ cell from here onwards.

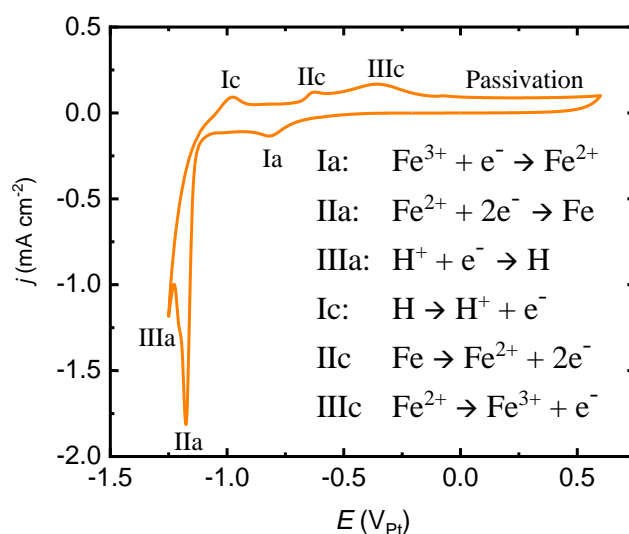


Figure 5.3. CV on FeO_x/Fe/Au thin film in 1 M LiOH in the developed cell. Electrochemical reactions are marked.

6 In-plane uniaxial anisotropy and blocked domain state in FeO_x/Fe thin films

The results of chapter 6 are published in [1] within the framework of this thesis. The respective paragraphs – with minor adjustments – are indicated in grey font. Reprint from [1] under Creative Commons Attribution (CC BY) license (<https://creativecommons.org/licenses/by/4.0/>)

6.1 Microstructure and composition

The cross-sectional layer architecture is examined by high-resolution transmission electron microscopy (HR-TEM) and shows a polycrystalline layered heterostructure (**Figure 6.1** (a)). The Fe grains show a thickness of around 5 nm. A native oxide layer with a thickness of 2-3 nm is observed which follows the shape of the Fe grains and penetrates deeper at the grain boundaries. The fast Fourier transformed (FFT) images of the individual layers show that the iron oxide (FeO_x-), iron (Fe-) and gold (Au) layers are all crystalline. As compared with the Fe layer, the FFT reflexes for the FeO_x are closer to the center due to the longer interatomic distances in real space. The FFTs indicate that the individual Fe grains align epitaxially with the underlying Au grains. Investigating the surface morphology, atomic force microscopy reveals also a polycrystalline nature of the film (see Appendix Figure 12.1). The average lateral grain size can be estimated to about 30 nm. Both is in accordance with the HR-TEM images. Raman spectroscopy identifies Fe₃O₄ as the dominant iron oxide phase (see Appendix Figure 12.2), which is expected after room temperature oxidation. [100–102]

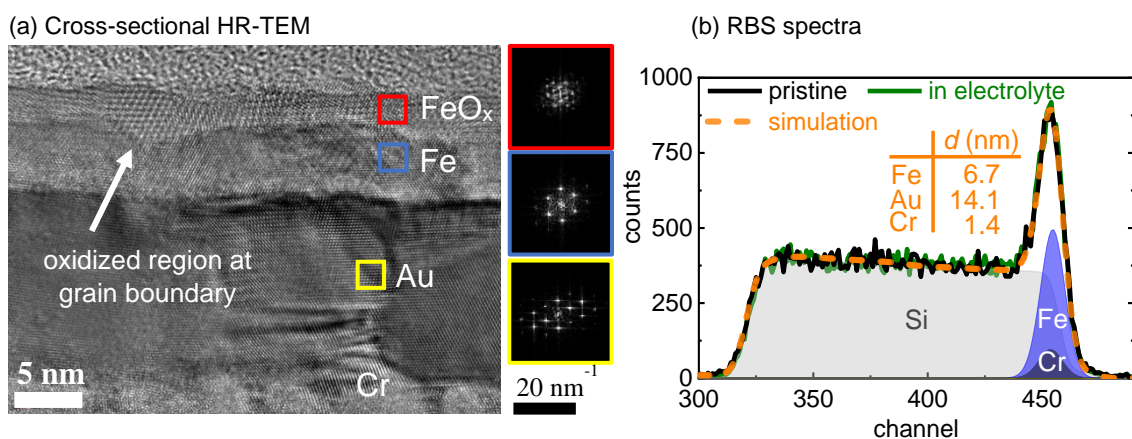


Figure 6.1: Microstructural and thickness characterization of pristine FeO_x/Fe thin film (a) Cross-sectional HR-TEM image and FFTs of the FeO_x/Fe/Au/Cr layers. (b) RBS spectra, derived elemental contributions, and extracted layer thicknesses d for the layer being in contact with air (black) and in the electrolyte (green). The deconvolution of the simulated fit in the elemental subspectra, used for the layer thickness calculation, is added. The fit is identical for both spectra, proving that no thickness change occurs upon addition of electrolyte solution.

The structure and orientation of the film was probed by x-ray diffraction (XRD) (see Appendix Figure 12.3) The planes which lie parallel to the surface are the fcc Au(111) and bcc Fe(110) planes. Pole figures (see Appendix Figure 12.3 (b), (c)) reveal a pronounced (111) fiber texture (intensity rings) of the Au thin film in accordance with the θ -2 θ scans. The previously indicated epitaxial relation of the Fe/Au grains derived from the FFT images (Figure 6.1 (a)) supports the interpretation from the XRD data that the individual Fe grains align epitaxially with the underlying gold grains. As the pole figure measurements reveal a random orientation of the Au grains in the film plane, we assume also an (110) in-plane fiber texture of the Fe grains.

To test the film thickness and the compatibility between the liquid electrolyte and the fabricated FeO_x/Fe thin films, in situ Rutherford backscattering spectroscopy was utilized. First, the layer thickness of the FeO_x/Fe thin film without being in contact with the electrolyte was determined. In a second step, 1 M LiOH electrolyte was added to the sample surface in a special in situ cell [94] and the layer system was measured again. A comparison of the measured RBS spectra in pristine state and in contact with the liquid electrolyte as well as simulated elemental contributions are presented in Figure 6.1 (b). To calculate the layer thicknesses, the areal density derived from the spectra was evaluated. The nominal Fe thickness of 6.7 +/- 0.5 nm, calculated from the RBS spectrum, matches the Fe thickness of about 5 nm as observed in the HR-TEM images after native oxidation, considering that about 1-1.5 nm of Fe is 'consumed' to form the FeO_x. Thus, the in-situ RBS measurement confirms that the FeO_x/Fe film is stable in contact with liquid electrolyte. It should be noted, that the areal densities of Fe and FeO_x are too similar and cannot be discriminated within the RBS measurement.

6.2 Magnetically blocked state in pristine FeO_x/Fe thin film

This section provides an overview of the magnetic characteristics of the FeO_x/Fe thin film. These characteristics are inherently connected to the polycrystalline and defect rich nature of the films which form the basis for interpreting the voltage triggered magnetic and structural changes thereof.

In-plane uniaxial anisotropy and hard axis anomaly

To investigate the influence of the FeO_x on the magnetic properties in the FeO_x/Fe thin film system, an Au/Fe/Au thin film is compared with an FeO_x/Fe thin film. The upper Au layer in the Au/Fe/Au film protects the Fe from oxidizing under ambient condition (see Appendix Figure 12.4). The Au/Fe/Au layer is taken as a reference for investigating the influence of the FeO_x on the magnetic properties in the FeO_x/Fe film. The in-plane angular dependency of M_R/M_S and H_c values is plotted in **Figure 6.2** for FeO_x/Fe thin film as compared to Au/Fe/Au layers. In both cases, the polar plots reveal a dominating uniaxial magnetic anisotropy. The angular dependencies of M_R/M_S and H_c qualitatively resemble

those expected from the Stoner-Wohlfarth model of uniaxial single-domain particles, [103] with the exception of the behavior very close to the hard axis (0°).

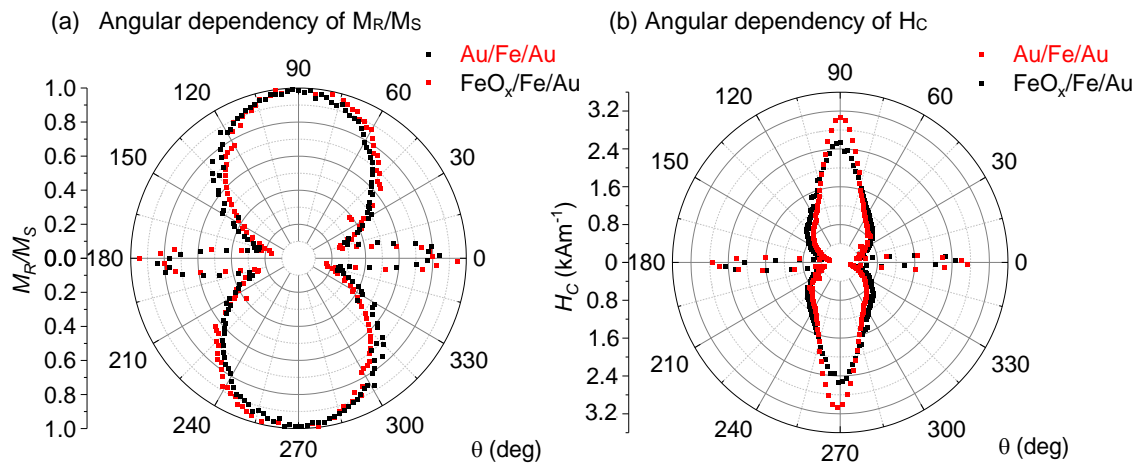


Figure 6.2: In-plane angular resolved measurements of a Au/Fe/Au and an FeO_x/Fe thin film. (a) M_R/M_S and b) H_c values of FeO_x/Fe/Au layers (black symbols) as compared to Au(10 nm)/Fe/Au layers (red symbols), as extracted from in-plane Kerr hysteresis loops measured at different applied magnetic field directions. (note: data points were measured from 0-180° and mirrored)

Such a deviation in the vicinity of the hard axis has been previously observed in polycrystalline films and has been attributed to local anisotropy fluctuations induced by different kinds of microstructural disorder in polycrystalline film and the associated formation of blocked state. [29,104,105]

Similar angle-dependent M_R/M_S and $\mu_0 H_c$ values are obtained for the Fe films capped with FeO_x and Au, except for slightly increased $\mu_0 H_c$ values in the vicinity of the easy axis (90°) for the Au/Fe/Au layers. From this, it can be concluded that in the present case there is a negligible effect of the native oxidation on the uniaxial anisotropy and the magnetization processes of the Fe films. It confirms previous observations that the uniaxial anisotropy arises from the oblique sputter deposition process. [106–109]. This type of anisotropy is usually traced back to a self-shadowing effect and an associated anisotropic-surface modulation [110] of the film. There is negligible contribution of the magnetocrystalline anisotropy of bcc Fe to the uniaxial anisotropy, because of the random in-plane orientation of the Fe grains that is inherited from Au grains (see Appendix Figure 12.3). In addition, in nanocrystalline films the magnetocrystalline anisotropy is averaged out, to a large degree, by exchange interaction according to the random anisotropy model. [111] The observed in-plane uniaxial anisotropy in the FeO_x/Fe films from the present study is consistent with previous work on Fe thin films prepared by oblique sputter deposition, [106,108,109] and can thus be attributed primarily to geometric surface/grain shape effects.

Hard axis magnetization reversal and blocked state

In order to understand the magnetization reversal process in more detail, we look at single magnetization curves. Along the easy axis, the shape of the curve is close to rectangular with $M_R/M_S \approx 1$. The hysteresis loop along the hard axis is more rounded, compared to the easy axis curve, with $M_R/M_S \approx 0.75$ and the H_C is comparable with the H_C along the easy axis, shown in **Figure 6.3** (a). An ideal hard axis of a uniaxial magnetic material would follow a linear magnetization reversal by uniform rotation with zero M_R and H_C , as depicted in Figure 2.3. Non-ideal hard axes, with high M_R and H_C , are reported for e.g. polycrystalline FeNi [29,112,113] or Co [105] thin films with uniaxial in-plane anisotropy. The underlying magnetization and domain processes when applying the field along the hard axis are known and can be described as follows (**Figure 6.3** (b)). [29] When the applied magnetic field is decreased from the saturated state (①), longitudinal fluctuations of magnetization (②) develop out of an incipient ripple structure [114]. Such magnetic fluctuations are caused by statistical perturbations from the random distribution of crystal anisotropy in polycrystalline films, inhomogeneous strain, texture, or non-magnetic impurities. [115] On decreasing the magnetic field further, the amplitude of the fluctuation of the magnetization becomes larger and, eventually, the magnetization splits in narrowly-spaced magnetic domains separated by domain walls (see also **Figure 6.4**). [29,113,116]

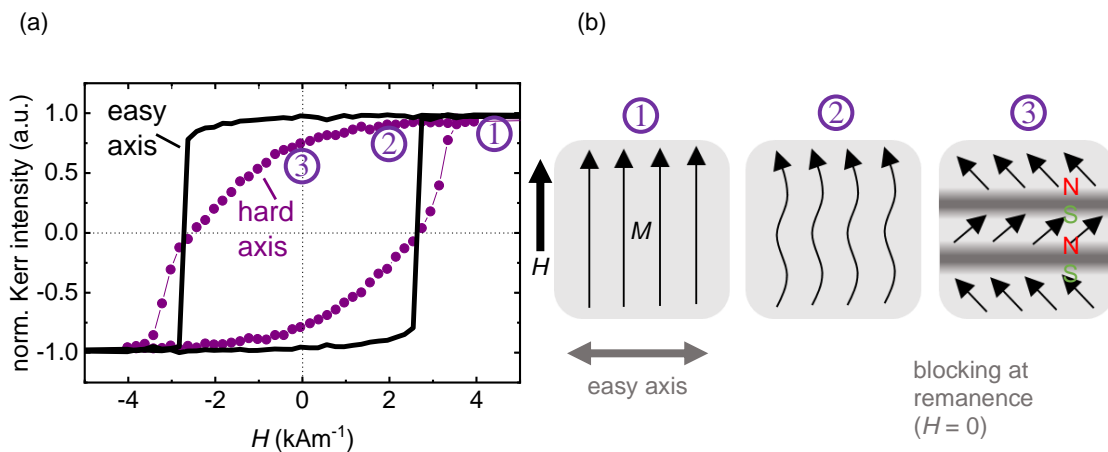


Figure 6.3: Magnetization curves and schematic of magnetization reversal along the hard axis.

(a) In-plane magnetization curves along the easy axis and the hard axis as measured by Kerr magnetometry. (b) Schematics of the development of the blocked state in a magnetic field along the (horizontal) hard axis. Starting from the saturated state (①), a fluctuating magnetization (②) forms that leads to the development of the blocked magnetic state (③) with high M_R/M_S ratio. The magnetic charges of the interacting Néel walls are marked by magnetic poles (N and S for North- and South pole, respectively).

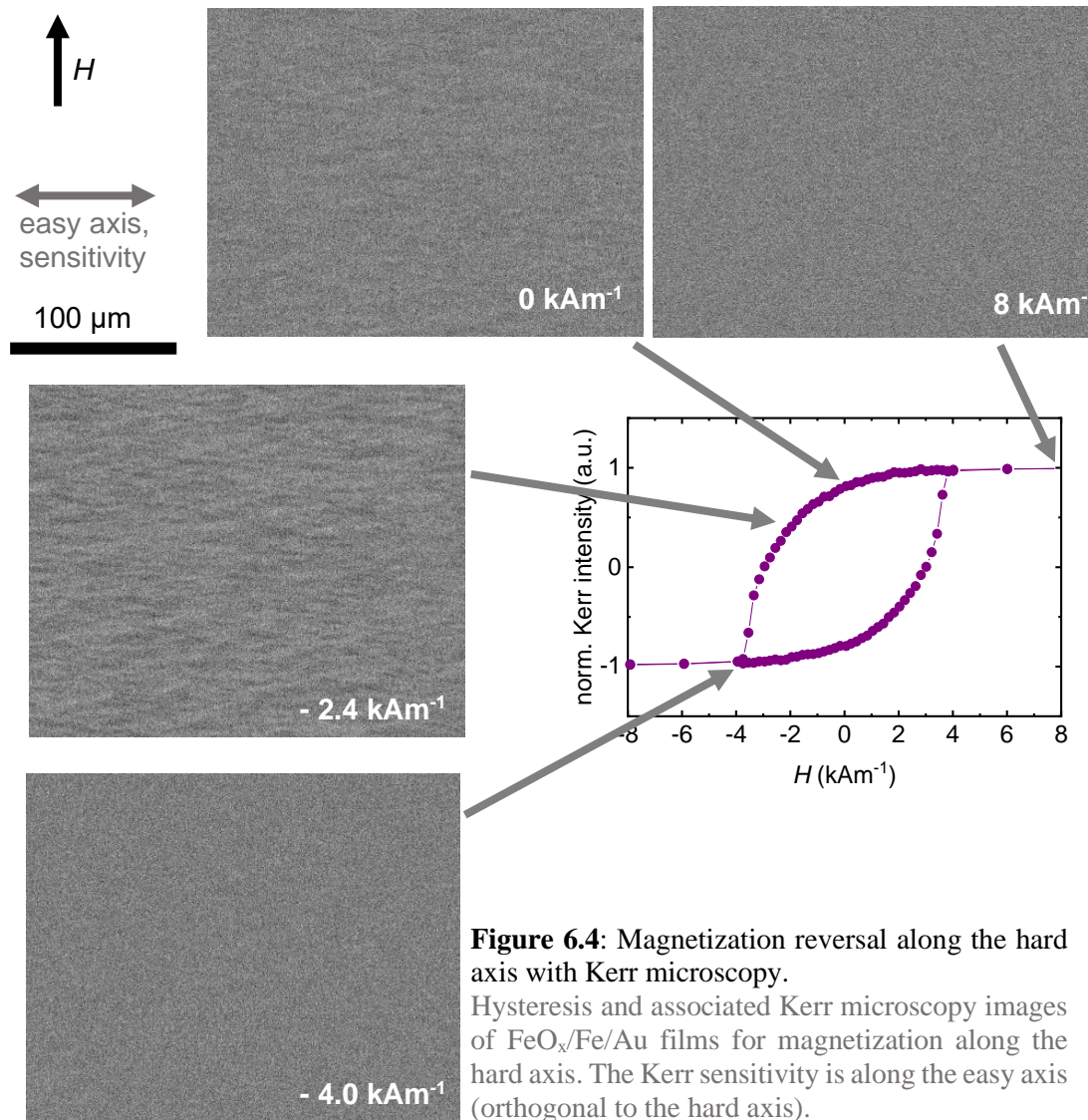


Figure 6.4: Magnetization reversal along the hard axis with Kerr microscopy.

Hysteresis and associated Kerr microscopy images of FeO_x/Fe/Au films for magnetization along the hard axis. The Kerr sensitivity is along the easy axis (orthogonal to the hard axis).

Anhysteresis for accessing anisotropy energy of hard axis magnetization curve

Anisotropy is a key factor for the evolution of H_C . As the hard axis magnetization curves shows M_R , it is not straight forward to derive the anisotropy energy (see also Figure 2.3). An alternative to measure anisotropy is to use anhysteretic curves. An anhysteretic curve represents the magnetization process with solely reversible changes. [117] **Figure 6.5** (a) shows the principle method to determine the anhysteretic magnetization curve. An anhysteretic curve is obtained by the application of a biasing direct current (DC) magnetic field and a superimposed alternating current (AC) magnetic field. The AC field strength saturates the sample and decays in amplitude. This process is repeated for every DC field strength. [117] Figure 6.5 (b) shows a comparison of the hysteresis and anhysteresis along the hard axis and the determination of the anisotropy. The anhysteretic magnetization curves (Figure 6.5) consist of a linear part at lower magnetic fields and a partly non-linear contribution at higher magnetic fields until saturation; the two parts identify homogenous

and inhomogeneous anisotropy contributions, respectively. [118] The anhysteresis allows the determination of the anisotropy energy and the type of domain wall.

Néel domain walls in FeO_x/Fe thin films

In extended permalloy films with an anisotropy parameter $Q = 2.5 \cdot 10^{-4}$ (being defined as $Q = K_u/K_d$ with $K_d = 0.5\mu_0 M_S^2$ being the stray-field energy coefficient [29]) the Bloch-Néel transition occurs around $12\sqrt{A/K_d}$. [119] This calculation can be applied also for the Fe films from the present study, because they exhibit a similar anisotropy parameter $Q = K_u/K_d = 1.8 \cdot 10^{-4}$ (with $K_u = 3.3 \cdot 10^2 \text{ Jm}^{-3}$ estimated from the anhysteresis in Figure 6.5 (a) and $K_d = 0.5\mu_0 M_S^2 = 1.8 \cdot 10^6 \text{ Jm}^{-3}$). Taking, as an approximation, the exchange constant of bulk Fe, $A = 1.98 \cdot 10^{-11} \text{ J/m}$, [120] the Bloch-Néel transition is expected to occur at a thickness of 40 nm. Thus, the present Fe films, with a much smaller film thickness of just 5 nm, are expected to exhibit Néel walls. **Figure 6.6** shows high-resolution longitudinal Kerr microscopy images of the FeO_x/Fe/Au films in the AC-field (20 Hz, 16 kAm⁻¹) demagnetized state. The Kerr sensitivities are along the easy axis on the left and (approximately) along the hard axis on the right. Wide, irregular domains with an average magnetization direction along the easy axis are seen in the image on the left. In the image on the right, the domain contrast (almost) disappears as the Kerr sensitivity is transverse to the domain magnetization. Under this condition, the Néel domain walls appear as the contrast reveals black and white segments according to the simultaneous presence of clockwise and counterclockwise magnetization rotation across the walls. It is expected that the Néel walls consist of a narrow core and extended tails (see Figure 2.2). The tails are not visible in the images, but could be viewed at a higher lateral resolution, i.e. by using Lorentz Transmission Electron Microscopy. [29] In that case, the ripple pattern would show up with a characteristic texture, from which the local magnetization direction could be derived.

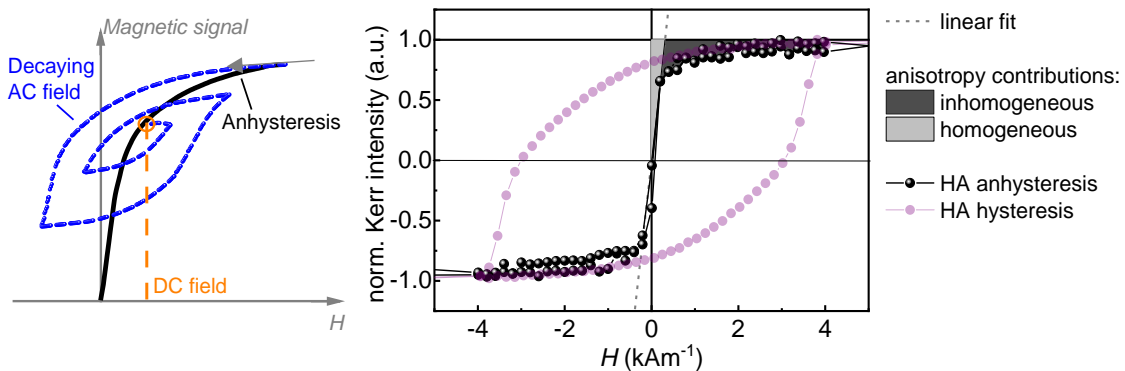


Figure 6.5: Anhyseretic measurement.

(a) Principle method for obtaining the anhyseretic magnetization curve by the superposition of a DC and AC magnetic field, adapted from [117]. (b) Hard axis hysteresis and associated anhyseresis. The anisotropy contributions are marked with marked anisotropy contributions.

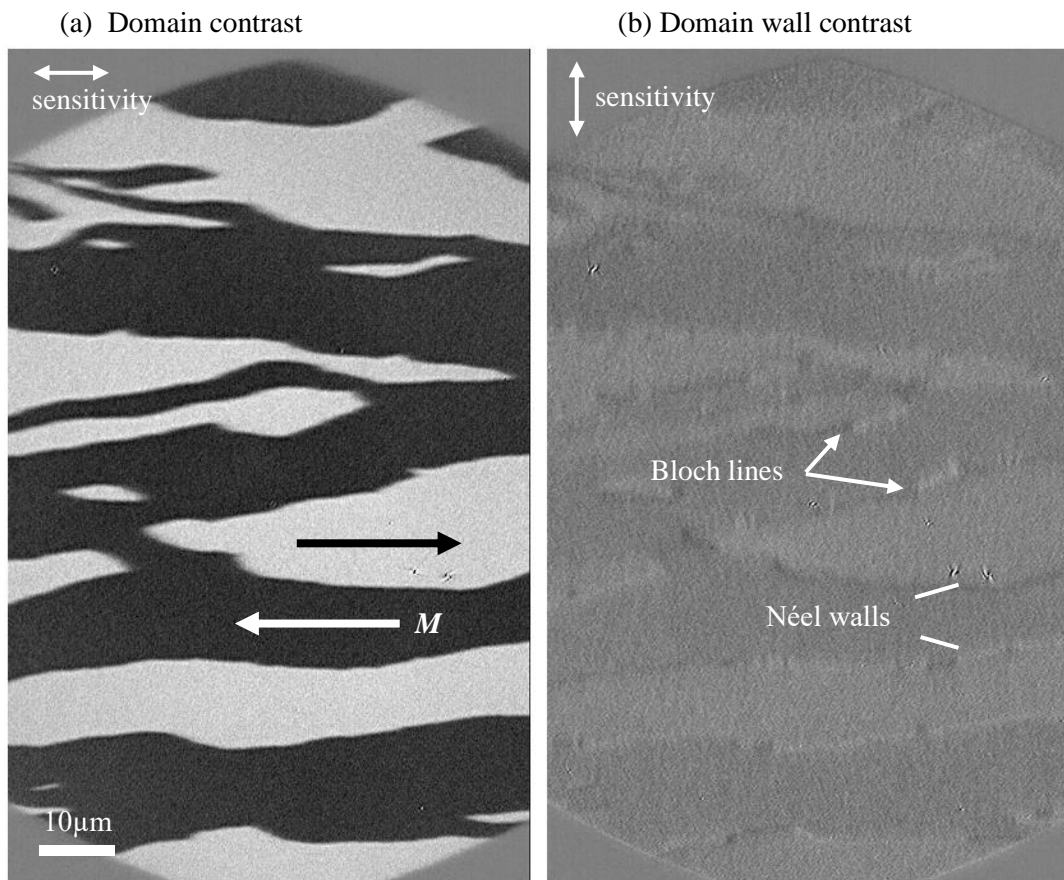


Figure 6.6: High resolution Kerr microscopy image of $\text{FeO}_x/\text{Fe}/\text{Au}$ thin films.

High resolution Kerr microscopy image of $\text{FeO}_x/\text{Fe}/\text{Au}$ films in the demagnetized state obtained by applying a decaying AC magnetic field along the hard axis. The image on the left reveals the magnetization components along the easy axis, while that on the right reveals the magnetization components along the hard axis (with some residual longitudinal contrast superimposed).

7 Voltage control of FeO_x/Fe thin films with in-plane uniaxial anisotropy

The results of chapter 7 are published in [1] within the framework of this thesis. The respective paragraphs – with minor adjustments – are indicated in grey font. Reprint from [1] under Creative Commons Attribution (CC BY) license. (<https://creativecommons.org/licenses/by/4.0/>)

In this part, the voltage control of magnetization reversal via an electrochemical reaction of the ferromagnetic layer in the FeO_x/Fe thin film system is achieved and discussed. The basic electrochemical mechanism is revealed by in situ Raman spectroscopy. Selected in plane directions and angle resolved magnetization measurements resolve a voltage induced collapse of H_C and M_R close to the hard axis during the reduction process. Anhysteretic measurements reveal an inverse scaling of coercivity and anisotropy upon reduction. By consulting the magnetic microstructure, a voltage induced change of the domain arrangement is found. Combining these results points to a de-blocking mechanism which originates from changes of the Néel wall interactions and also hints to changes in microstructural pinning sites. Afterwards, 180° magnetization reversal is achieved in a biased magnetic field but triggered by a voltage. The energy efficiency and the application potential are discussed.

7.1 Voltage control of hysteresis by electrochemical reduction of FeO_x

Reversible electrochemical reduction/oxidation reactions in the FeO_x/Fe layer are expected when specific external voltages [99] are applied via the electrolyte. In-situ Raman measurements (**Figure 7.1** (a)) confirmed a voltage-induced phase transformation in the FeO_x/Fe films. In the pristine state, the characteristic peak at 665 cm⁻¹ identifies Fe₃O₄ in the native iron-oxide layer, which is expected after room temperature oxidation. [100] After addition of the electrolyte, a Raman measurement was first carried out in the open circuit potential (ocp) state, i.e., the state of the FeO_x/Fe layer in the electrolyte without additional external voltage applied. In this ocp state, the Fe₃O₄ peak can still be clearly observed despite the increased electrolyte-induced background level in the in-situ Raman measurement. When a reduction potential of -1.10 V is applied, the Fe₃O₄ peak vanishes, evidencing a voltage-induced FeO_x to metal Fe transformation. The complete disappearance of the Raman signature of Fe₃O₄ indicates that a full transformation of Fe₃O₄ to Fe metal occurs. This is in line with the evaluation of the transferred charge during the reduction (see **Figure 12.5** in Appendix), The Fe₃O₄ peak re-appears after re-oxidation of the reduced metal state, which establishes the reversibility of the reduction reaction.

To characterize the voltage-dependency of the reduction reaction and to reveal associated electrochemical changes, the current density j and the magnetic properties of the FeO_x/Fe films were measured simultaneously at selected cathodic potentials E . For each voltage

step, E was applied for 60 seconds and a new pristine sample was used in each case to exclude the effects of previous treatments. The magnetization curve measurement was performed through the electrolyte by MOKE magnetometry in a dedicated in-situ Kerr microscopy setup (Figure 7.1 (b) and chapter 5). The implemented electrochemical cell was assembled in a three-electrode arrangement with the FeO_x/Fe films as the working electrode. Figure 7.1 (c) shows a comparison of the easy and hard axis in their pristine state and in the ocp state. Figure 7.1 (d) shows the observed E -dependency of j (black data points) and H_C (blue data points), respectively, along the in-plane easy axis. The coercivity in the ocp state, $H_{C,ocp}$, lies at 2.4 kAm^{-1} .

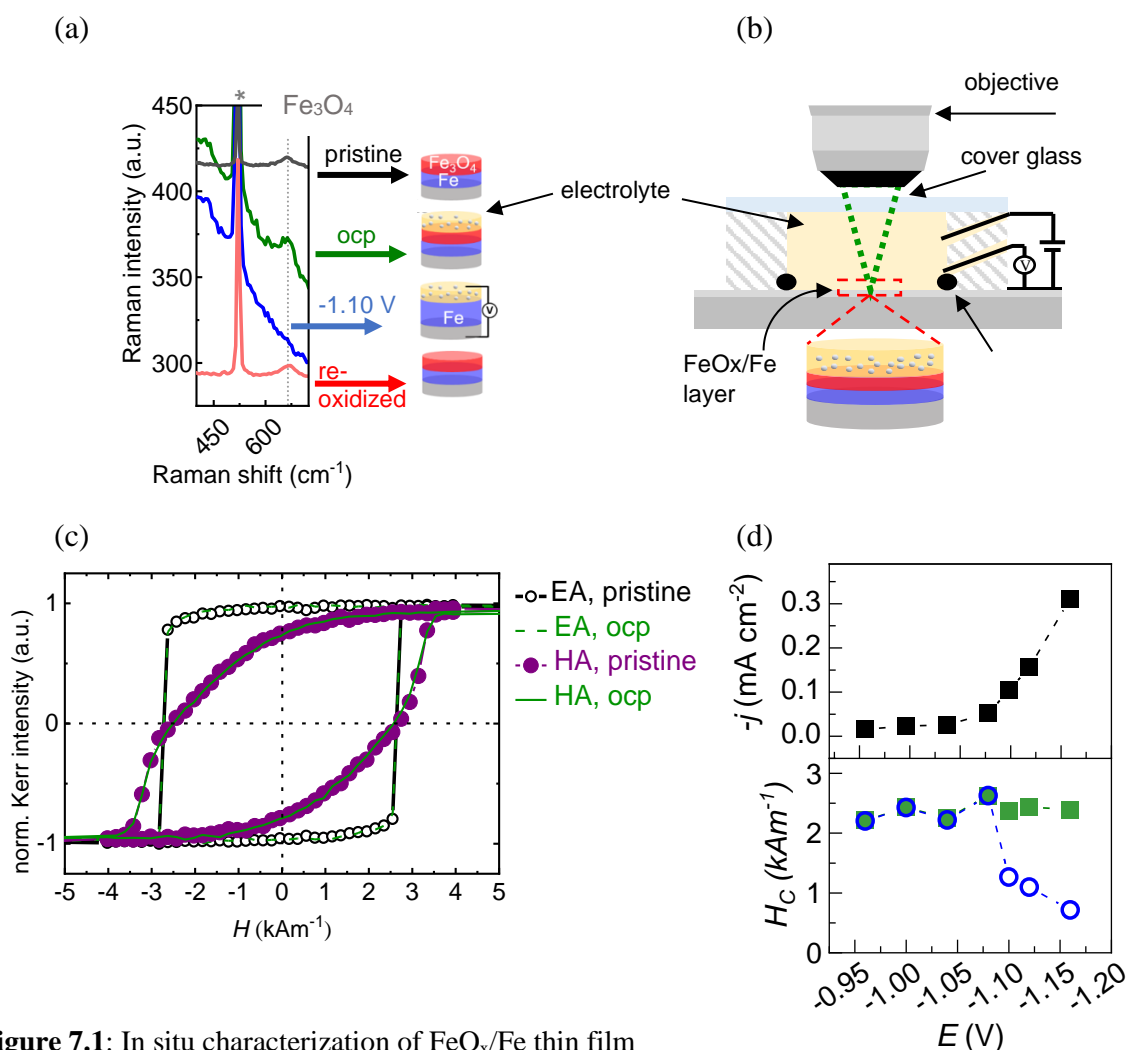


Figure 7.1: In situ characterization of FeO_x/Fe thin film

Voltage-control of the H_C by electrochemical reduction of FeO_x . (a) Raman spectra for the same $\text{FeO}_x/\text{Fe}/\text{Au}$ layer in the pristine state, in the electrolyte at the ocp state, in the electrolyte at a reduction potential $E = -1.10 \text{ V}$, and after re-oxidation and electrolyte removal. The asterisk indicates the substrate peak. The native Fe_3O_4 peak vanishes during the reduction (oxide to metal transformation at -1.10 V) and re-appears during re-oxidation (metal-to-oxide transformation). Schemes for the different states are displayed on the right. (b) Sketch of the electrochemical cell combined with a wide-field Kerr microscope. (c) Comparison of easy and hard axis in the pristine state and at the ocp state. (d) Reduction current density $-j$ (black data points) and simultaneously measured relative H_C change along the in-plane easy axis (blue data points) in dependence of the applied potential

No significant changes in current density and H_C are observed up to $E = -1.08$ V. The strong increase of the cathodic (negative) current density below -1.08 V indicates the onset of the reduction of the FeO_x to metallic Fe. Simultaneously, a drastic decrease in H_C is measured. At -1.10 V the H_C decreases to 1.3 kAm^{-1} , corresponding to 53 % of the initial value at the ocp state. For more negative potentials, a further decrease in H_C down to 30 % is reached but, at the same time, the H₂ evolution reaction becomes a dominant side reaction and hinders the stable operation of the cell. The simultaneous change of current density and H_C below the threshold potential of the FeO_x-to-Fe-transformation reaction confirms that the voltage-induced change in H_C originates from this electrochemical transformation. By contrast, changes caused by capacitive charging mechanisms should scale linearly with the potential and would not require a threshold potential. The drastic change of H_C is a first sign of the significant voltage-tunable magnetism that is possible in the present system.

We measured the impact of the reduction at $E = -1.10$ V and re-oxidation at $E = -0.02$ V on the magnetic properties along different in-plane magnetic field angles with respect to the pristine state (**Figure 7.2**). For all three axes – (0°), easy (90°), and intermediate (45°) – the application of the reduction potential leads to a strong decrease in H_C (**Figure 7.2** (a-c)). Close to the hard axis, both H_C and M_R almost vanish. Upon re-oxidation, the hysteresis loops nearly recover to those of the pristine state for all three directions. The reversibility of this process for 10 cycles is shown as a representative of the H_C change along the intermediate axis in **Figure 7.2** (d) (top). The associated change in Kerr intensity difference ΔI (**Figure 4d** (bottom)) reversibly increases and decreases by about 15-20 % upon reduction and re-oxidation, respectively. For a rough estimate, an increase of 11 % in overall M_S is expected for the full reduction of a Fe₃O₄ (3 nm)/Fe (5 nm) bilayer to a single Fe (7 nm) layer. The observed change in ΔI is qualitatively consistent with this, and also with previously observed changes in M_S for FeO_x/Fe films polarized in alkaline electrolytes. [121]

The in-plane angular distribution of H_C and M_R/M_S ratio, respectively, was extracted from angle-resolved Kerr measurements from 0° to 180° in steps of 10° for both pristine (black symbols and grey area) and reduced state (blue symbols and blue area) (**Figure 7.2** (e,f)). The dominant two-fold symmetry reflects the mentioned uniaxial anisotropy. Consistent with such anisotropy, H_C and M_R/M_S ratio both decrease when turning the field from the easy axis (90°) toward the hard axis (0°, 180°). In the vicinity of the hard axis, the sudden and strong increase in the M_R/M_S ratio and H_C in the pristine state is consistent with the proposed formation of the blocked state by Néel wall interactions and the pinning of Bloch lines in the nanocrystalline FeO_x/Fe films (see discussion in section 6.2). This deviation from expected ‘ideal’ hard-axis behavior constitutes a peak of M_R/M_S ratio and H_C in an angle range of ca. $\pm 10^\circ$ around the hard axis (**Figure 7.2** (e,f)).

Remarkably, the voltage-induced reduction leads to a strong decrease in H_C for all field directions (**Figure 7.2** (e)). In an extended angle range around the easy axis (50° - 130°), H_C drops to 30-50% of the initial value. The strongest voltage-induced effect on H_C occurs in the vicinity of the hard axis. Additional measurements with a higher angular resolution close to the hard axis confirm a drastic voltage-induced decrease in H_C to 5%

of the initial value (see Appendix Figure 12.6 (a)). For the M_R/M_S values (Figure 7.2 (f)), changes upon voltage-induced reduction are negligible for angles close to the easy axis, whereas a significant decrease in M_R/M_S to 10% of the initial value (see Appendix Figure 12.6 (b)) is measured when approaching the hard axis. To summarize, the strongest voltage-induced H_C and M_R/M_S ratio changes are achieved when magnetic fields are applied close to the hard axis, where a blocked magnetic state is initially present. In Figure 7.2 (e) and (f), this is reflected in a change in the peak feature representing the deviation from ‘ideal’ hard-axis behavior around 0° and 180° : in the reduced state at -1.10 V, the magnitudes of the deviations and/or the angular widths of the peak around the hard axis become smaller, indicating a voltage-induced magnetic de-blocking.

The comparative study of FeO_x/Fe/Au and Au/Fe/Au layers (see Figure 6.2) rules out the possibility that the change in magnetic behavior originates solely from the voltage-induced increase of the Fe layer thickness [121,122] or the removal of a specific FeO_x. Instead, the massive change in the close-to-the hard-axis behavior indicates that the factors that are key to the evolution of coercivity and the blocked state, namely anisotropy and magnetic microstructure, are modified during the reduction process.

7.2 Inverse scaling of coercivity and anisotropy revealed by anhysteresis

Anisotropy is a key factor for the evolution of coercivity. Magnetoelectric effects are often explained via the direct proportionality between voltage-induced anisotropy and coercivity changes. [53,115,123] Therefore, we studied the anisotropy and the anisotropy fluctuations in both pristine and reduced states in greater detail. The similar shapes of the angular H_C - and M_R/M_S ratio distributions for the pristine- and reduced states in Figure 7.2 (e,f) confirm that uniaxial anisotropy continues to predominate. However, larger relative angle-dependent M_R/M_S and H_C changes are observed in a normalized plot (Figure 12.6 (c,d)), which indicates that the magnitude of the uniaxial anisotropy increases in the reduced state.

Clearly, homogeneous anisotropy increases strongly upon reduction. The anisotropy field, obtained by extrapolating the linear part of the anhysteretic magnetization curve to saturation, changes from 0.3 kAm^{-1} in the pristine state to 1.1 kAm^{-1} in the reduced state. The associated uniaxial anisotropy constants (K_u) of 326 Jm^{-3} and 1202 Jm^{-3} for the pristine and reduced state, respectively, are estimated from the respective areas of the homogeneous anisotropy contribution depicted in Figure 7.3 by assuming the saturation magnetization of (bulk) Fe, $M_{S,Fe} = 1710 \text{ kAm}^{-1}$. The complex evolution of the anisotropy in nanocrystalline two-phase systems currently prevents us from unambiguously determining why the anisotropy increases upon reduction. We speculate that the increase could be attributed to an anisotropic change in the grain shapes/sizes or roughness of Fe upon electrochemical FeO_x reduction. In addition, an electronic-charge-induced modulation of the interface PMA of the Fe layer, [54] caused by superposed electrochemical double-layer formation at the reduction potential, may play a minor role.

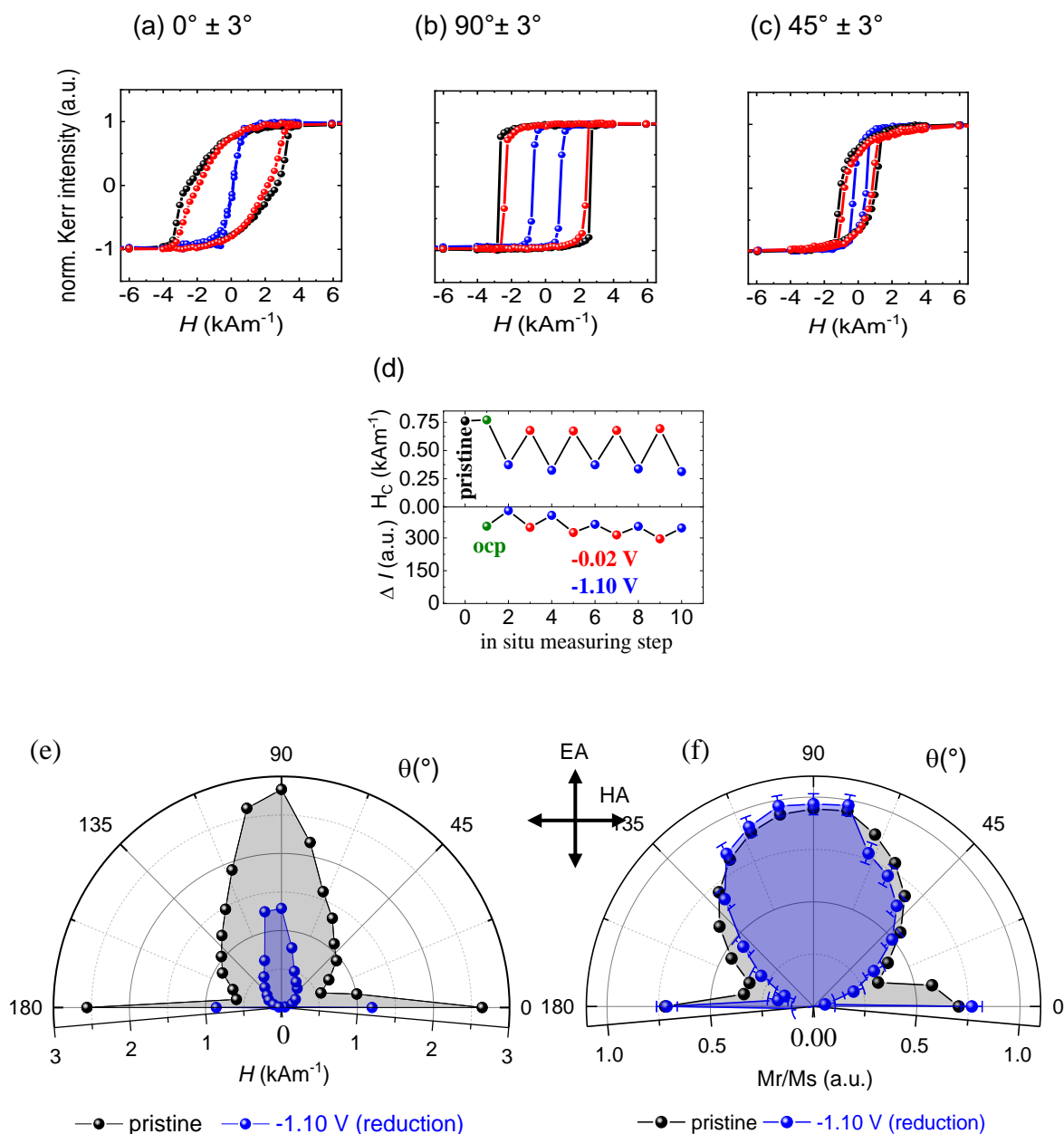


Figure 7.2: Electrochemical control of magnetization curves in FeO_x/Fe thin films

Reversible angle-dependent voltage control of magnetic hysteresis up to ON/OFF switching of coercivity and remanence (magnetic de-blocking). a – c) Magnetization curves of FeO_x/Fe films in the pristine state at -1.10 V (reduction) and -0.02 V (oxidation) measured by Kerr magnetometry with an in-plane magnetic field close to (a) the hard axis ($0^\circ \pm 3^\circ$), (b) the easy axis ($90^\circ \pm 3^\circ$), and (c) an intermediate axis ($45^\circ \pm 3^\circ$). d) Reversible coercivity change along the intermediate axis when repeatedly switching between reduced (-1.10 V) and oxidized (-0.02 V) state. e, f) Angular dependence of coercivity (e) and M_R/M_S ratio (f) in the pristine state and at -1.10 V (reduced state).

An increase of in-plane uniaxial anisotropy resulting from a voltage-induced decrease of interface PMA has been reported for vicinal Fe films, even considerably thick ones (35 monolayer). [124] However, at this thickness, the effects are significantly smaller than those observed in the present films. This can explain the observed decrease in the inhomogeneous anisotropy contributions. The increase of homogeneous anisotropy occurring simultaneously with the drastic decrease in coercivity upon reduction shows that the direct proportionality between anisotropy and coercivity, which is often used as a simple model for magnetoelectric effects, [11,53,125] is not applicable here. Instead, it is likely that changes in microstructure or magnetic domain structure dominate over direct anisotropy effects, as discussed in the next section.

7.3 Voltage control of magnetic domains

The magnetic domain observations were made with an in-situ Kerr microscopy setup, which resolves the magnetic domains concurrently with electrochemical polarization in the liquid electrolyte. **Figure 7.4** (a-d) shows the AC-demagnetized states, which resemble domain states close to zero-field equilibrium, for a pristine FeO_x/Fe film and for the same film in the electrolyte at the ocp, reduction (−1.10 V), and oxidation (−0.02 V) states. For all images, the demagnetizing is carried out along the hard axis and the

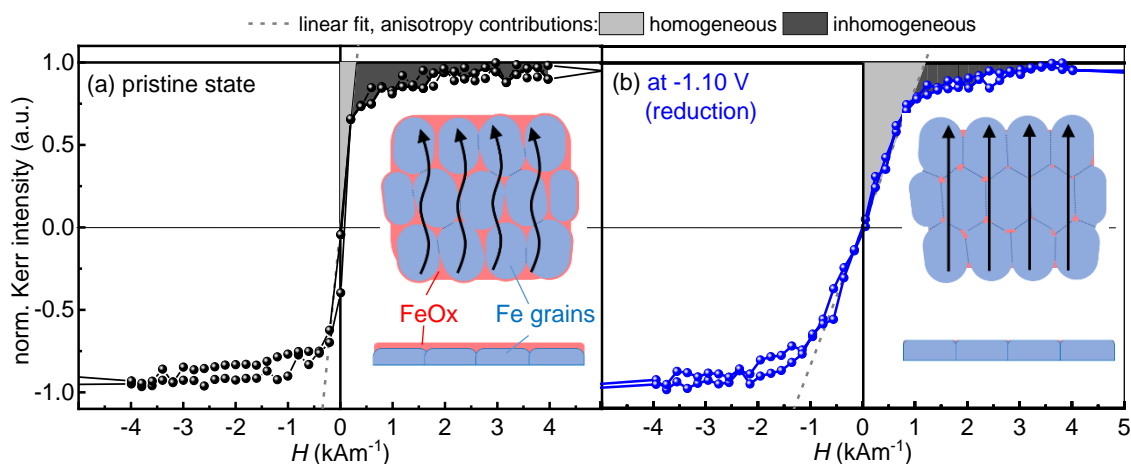


Figure 7.3: (In situ) anhysteretic measurements of FeO_x/Fe thin film.

Determination of voltage-induced anisotropy change. a, b) Anhysteretic magnetization curves of FeO_x/Fe films as measured by Kerr magnetometry along the in-plane hard axis for the pristine state (a) and at -1.10 V (reduced state) (b). Separation of homogeneous and inhomogeneous anisotropy contributions by a linear fit in the low magnetic field region. The sketches in both panels illustrate the proposed microstructural origin. In the natively oxidized state (a), strong anisotropy fluctuations can result from an inhomogeneous microstructure and grain boundary FeO_x, which partially decouple the individual Fe grains and yield local variations of the easy axis. In (b) the decrease of the anisotropy fluctuations can be explained by the reduction of the grain boundary oxides into Fe, which homogenizes the microstructure and allows better coupling between the Fe grains.

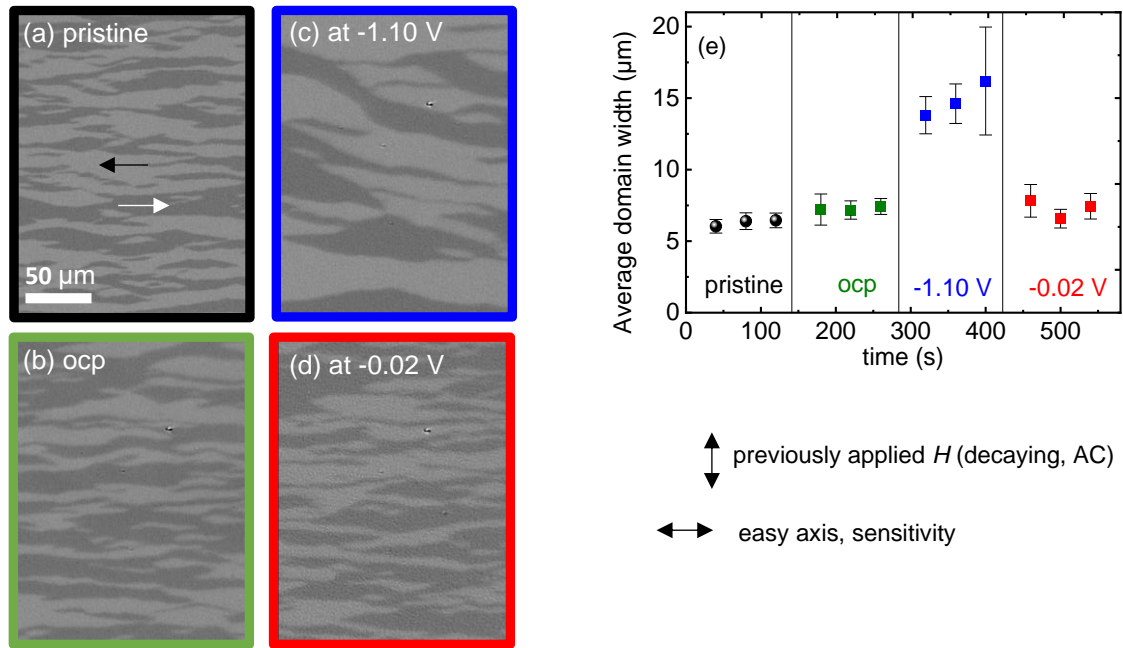


Figure 7.4: Voltage control of magnetic domain size

a-d) Magnetic domains observed by in-situ Kerr microscopy in the pristine state (a), in the ocp state (b), at -1.10 V (reduction) (c), and at -0.02 V (oxidation) (d). The images were acquired after a decaying 20 Hz AC field was applied perpendicularly to the easy axis. Arrows on the right indicate easy axis, Kerr sensitivity, and magnetic field directions. e) Average domain size, extracted from the domain images for the four states (a-d). For each state, the AC routine and domain image acquisition was repeated three times.

Kerr sensitivity is set along the easy axis. The domains are observed to extend along the easy axis and their somewhat irregular shape is typical for polycrystalline thin films with uniaxial anisotropy and Néel walls. [29] The average magnetization in the domains is aligned along the easy axis (marked exemplarily with the black and white arrows in Figure 7.4 (a)). As expected, the magnetic domain character and width are not altered by the electrolyte contact (pristine versus ocp state). While applying the reduction voltage of -1.10 V, the shape of the domains remains comparable but a strong increase in domain width is observed. During re-oxidation (-0.02 V), the average domain size decreases again and the domain image resembles that of the pristine and ocp states. For the pristine-, ocp- and re-oxidized states, all of which are characterized by the presence of an FeO_x cover layer, the average domain width is around 6 μm (Figure 7.4 (e)). By contrast, the average domain width in the reduced state is around 14 μm. An example for the domain width analysis is given in the Appendix in Figure 12.7.

The observations described above point clearly to a significant voltage-induced change of the equilibrium magnetic domain width upon oxidation/reduction. This increase of domain size could be caused by an increase in domain-wall energy, which results in an energy-saving decrease in the number of domain walls. We calculate the change in the domain-wall energy upon reduction by accounting for an increase in Fe-layer thickness

Table 1: Exchange constant A , saturation magnetization M_S , anisotropy constant K_u , Fe layer thickness d and calculated wall core width a and surface energy density for a Néel wall in for pristine and reduced (at -1.1 V) state

	Pristine state	Reduced state
A (Jm^{-1})	$2.0 \cdot 10^{-11}$	
M_S (Am^{-1})	$1.71 \cdot 10^6$	
K_u (Jm^{-3})	326	1202
d (m)	$5 \cdot 10^{-9}$	$7 \cdot 10^{-9}$
a (m)	$1.1 \cdot 10^{-6}$	$5.7 \cdot 10^{-7}$
γ (Jm^{-2})	$4.9 \cdot 10^{-3}$	$7.0 \cdot 10^{-3}$

from 5 nm to 7 nm, which is expected during the reduction process, [122] and by considering the measured changes in K_u (see Figure 7.3). With the thickness of the Fe films of 5 nm (7 nm) in oxidized (reduced) state, the films are in the ultrathin limit [31,126], where the wall core thickness can be approximated with Equation 5. The parameters used for the calculations according to equations (1, 2) and the calculated core wall thicknesses and surface energy densities obtained from the two equations for the pristine (oxidized) and reduced (-1.1 V) state are given in Table 1. The results show that a 40% increase in surface energy of the Néel wall can be expected due to the voltage-induced changes in film thickness and anisotropy during the reduction process. Additional wall energy contributions are associated when interactions of the Néel walls occur. However, no significant change is expected here, since the measured domain size and film thickness remains in the same order of magnitude for pristine and reduced state (compare Figure 3.77 in Ref. [29]).

This calculation shows that an increase in domain-wall energy of ≈ 40 % can be expected during the reduction process, which could explain the decrease in the number of domain walls and the associated increase in the equilibrium domain size.

7.4 Magnetic de-blocking due to change of Néel wall interactions

Based on the results presented above, we propose a consistent mechanism that connects the voltage-induced changes in hysteresis, anisotropy, and domain size with the reduction/oxidation process. Since the magnetization processes are distinctly different for fields along the hard and easy axis, both are addressed individually.

For the hard-axis case, the impact of oxidation and reduction on the hysteresis can be explained by the interplay of the anisotropy change and the specific properties of the magnetically charged Néel walls. The blocked state, which causes the large H_C and M_R along the hard axis in the pristine (oxidized) state (Figure 6.3), originates from the interaction between the extended tails of the Néel walls. The tail width w_{tail} depends strongly on the anisotropy, [29] which implies that the voltage-induced change in K_u also changes w_{tail} . For symmetric Néel walls, w_{tail} is determined by a balance between the

magnetic charge distribution, described by the maximum stray field energy density (K_d) and the anisotropy energy (K_u) [29]:

$$w_{tail} = e^{-\gamma} d_{Fe} K_d(Fe) / K_u(Fe) \approx 0.56 d_{Fe} K_d(Fe) / K_u(Fe) \quad (\text{see also Equation 6})$$

where $\gamma = 0.577$ is the Euler-Mascheroni constant and d is the film thickness. For the present case, we use the K_u values obtained from the anhysteretic measurements and Fe-film thicknesses of 5 and 7 nm for the pristine (oxidized) and reduced state, respectively, in equation (1). With those values, we obtain tail widths of 24.1 μm and 8.4 μm for the pristine (oxidized) and reduced state, respectively. This indicates that w_{tail} decreases concurrently with the increase in domain size upon reduction. For parallel walls, wall interactions play a role as soon as an overlap of the Néel wall tails occurs, i.e. when the domain width $< 2 w_{tail}$. [29] For the oxidized state, strong interaction is expected as the average domain width of around 6 μm is much smaller than $2 w_{tail} = 48 \mu\text{m}$. This is consistent with the emergence of a strong blocking. Upon reduction, the values for the average domain size of 15 μm and $2 w_{tail} = 16 \mu\text{m}$ are similar. Even though this comparison is carried out on the basis of equilibrium domains, a qualitatively similar trend is expected and observed (**Figure 7.5**) for the domains present in the remanent state. In **Figure 7.5** the magnetic domain images of FeO_x/Fe/Au films in LiOH solution obtained by in situ Kerr microscopy during magnetization reversal along the hard axis are compared for the state at ocp (oxidized state) and at -1.10 V (reduced state). For in the ocp state, the fine domain structure, which is characteristic for the blocked state (see also **Figure 2**) is observed. In contrast, at -1.10 V, larger domains are observed, with irregular nature connected to pinning. The striking difference in the domain size is in line with the de-blocking mechanism proposed in the manuscript. In agreement with the significantly decreased H_C at -1.10 V, the saturated state is achieved at lower reverse magnetic fields than in ocp state. We expect that significantly fewer interactions between the walls will occur in the reduced state, which is consistent with the observed de-blocking. We can thus conclude that the voltage-induced switching from a blocked state to a ‘close-to-ideal’ hard-axis behavior with negligible M_R and H_C , and vice versa, results from a change in amplitude of the Néel wall interactions. This change in wall interactions, in turn, originates from anisotropy-related decrease/increase in Néel wall tail width in combination with the coarsening/refinement of the magnetic microstructure. If the field is applied along the easy axis, the decreased H_C (see **Figure 7.2 (a-e)**) upon reduction, concurrent with an increased anisotropy, seems unexpected at first glance. However, this need not be the case if we bear in mind that H_C is an extrinsic property and depends on both, anisotropy and microstructure. In the present study, the voltage-induced K_u and H_C vary inversely, which implies that microstructural effects dominate over the anisotropy effects. We propose that this is due to the electrochemical modification of the grain boundary oxides, which can act as pinning centers for the magnetic domain walls in the pristine state. Upon reduction, the defective FeO_x centers will transform to ferromagnetic Fe and thereby lose the pinning functionality. In addition, the homogenization of the ferromagnetic Fe surface and better exchange coupling of the individual Fe grains are

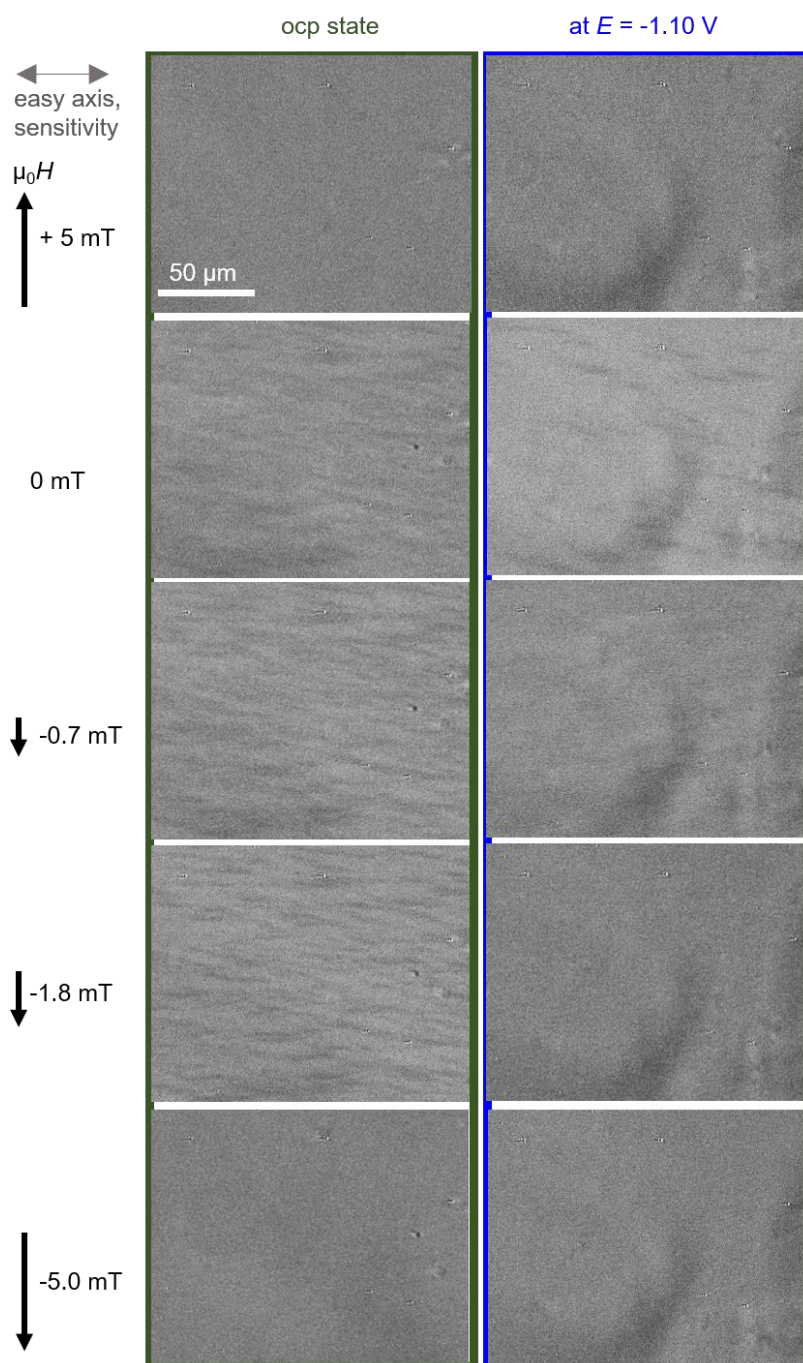


Figure 7.5. Magnetic domain images of $\text{FeO}_x/\text{Fe}/\text{Au}$ films in LiOH solution during magnetization reversal along the hard axis in ocp state (left) and at -1.10 V (right).

expected, which is in agreement with the measured increased homogeneity of anisotropy in this study. All three effects can contribute to the drastic decrease in H_C along the easy (and also intermediate) axis.

Until now, similar effects have been well known for magnetic materials in which grain boundaries are altered in an irreversible way. For example, a decrease of H_C is observed when switching from decoupled nanogranular structures to coalesced FePt films [127]. Also, for Nd₂Fe₁₄B magnets, the control of H_C and M_R relies on the tuning of the exchange coupling between the Nd₂Fe₁₄B grains, which is achieved by the optimization of the nature and distribution of intergranular phases. [128] The present study demonstrates that similar H_C control can be achieved in a reversible way by voltage-induced FeO_x reduction and re-oxidation at grain boundaries in thin films. The magnetic changes in our FeO_x/Fe thin-film system are reversed within seconds (see following section) and are also fully reversible during several voltage switching steps.

7.5 Switching of magnetization by a low voltage and energy efficiency

Magnetization switching by 180°, induced by an electrical field instead of magnetic fields, is of general interest in magnetic devices and is desired for such applications as logical operation modes. [129] The reversible collapse of H_C by voltage-triggered reduction that we document from the present study offers a direct route to voltage-induced switching of magnetization by 180° in the presence of a small magnetic bias field. This is demonstrated in **Figure 7.6** as compared with conventional magnetic-field switching along the magnetic easy axis.

The starting point is the ocp (oxidized) state, which is saturated at $H = +15.9 \text{ kAm}^{-1}$ and which exhibits a H_C of 2.9 kAm^{-1} . Conventional M -switching under magnetic field control (green curve in Figure 7.6 (a)) was probed via in-situ Kerr microscopy. The magnetization reversal can be followed from the Kerr micrographs, starting with the saturated state (upper image in Figure 7.6 (b)), followed by the switching via nucleation and growth of reverse domains (middle image), and ending with the fully switched state with reverse magnetization (bottom image). To demonstrate E -induced switching, the same sample, again after saturation in $H = +15.9 \text{ kAm}^{-1}$, is held at $H = -1.6 \text{ kAm}^{-1}$. In this state, the magnetization is still fully aligned in the direction of the previously applied positive magnetic field. The application of $E = -1.10 \text{ V}$ leads to a reduction of H_C and consequently to magnetization reversal, which can be followed by the domain images in Figure 7.6 (c). The voltage is applied after 10 s at a magnetic field of -1.6 kAm^{-1} . At this time, the fully saturated state is probed (upper image in Figure 7.6 (c)). After about 30 s at -1.10 V , reverse domains nucleate and grow (middle image). Full switching occurs within 2 seconds (bottom image). This M -switching is unambiguously caused by the voltage application: a control experiment for the same sample at -1.6 kAm^{-1} at ocp showed that no change in magnetic state occurs within 120 seconds without applied voltage (see video in [1]).

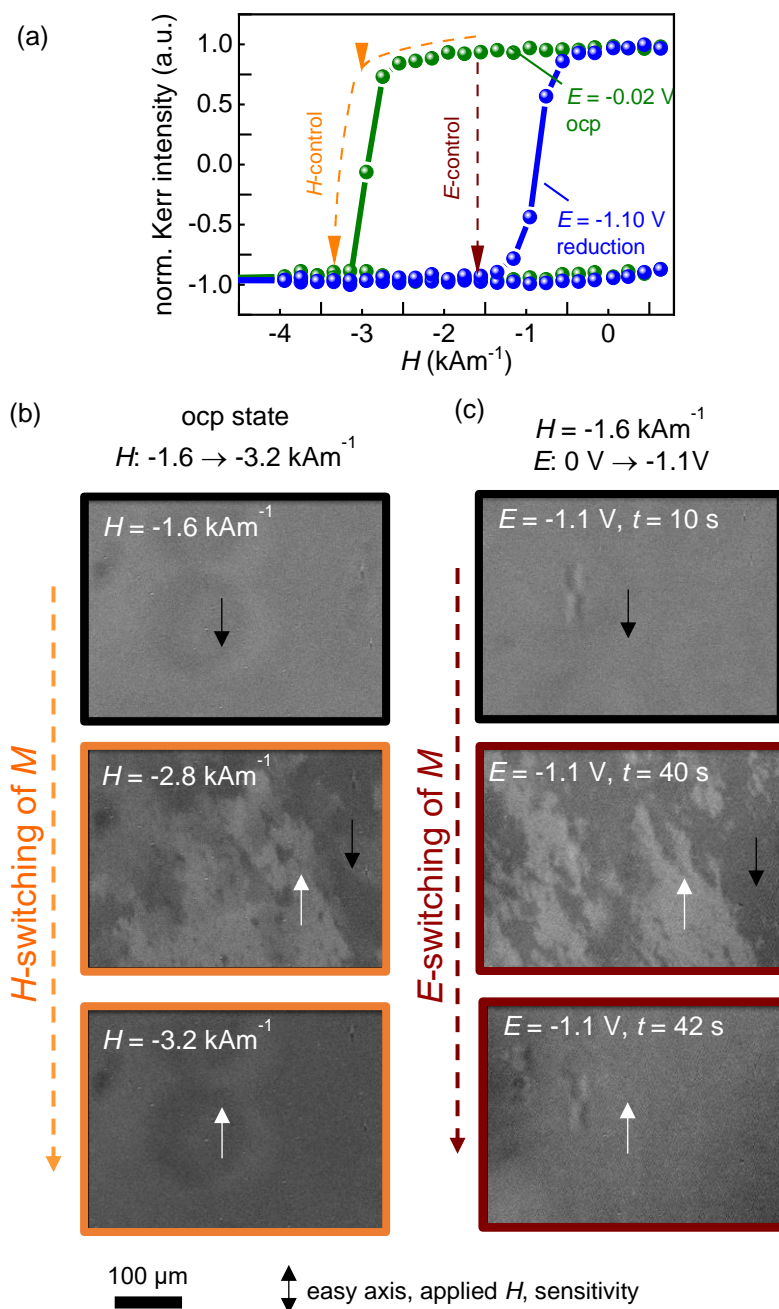


Figure 7.6: E-induced 180° switching of magnetization by a low voltage.

a) Pathway for E -induced magnetization reversal based on the voltage-induced change from a high H_C -state (o.c.p. state, green curve) to a low H_C -state (-1.10 V, reduced state, blue curve) at a small bias field of -1.6 kAm^{-1} . The conventional magnetic field-controlled magnetization reversal is indicated for comparison. b, c) Domain evolution at the same sample position during the H -induced (b) and the E -induced (c) magnetization reversal. These in-situ Kerr images were extracted from a video camera monitoring the switching processes. The sample was saturated at $+15.9$ kAm^{-1} prior to switching in both cases.

After the voltage-induced M -switching, a hysteresis with significantly lower H_C , as expected for the reduced state, is measured (blue curve in Figure 7.6 (a)). Remarkably, the E - and H -controlled magnetic reversal proceed in a similar manner. This becomes evident from the comparison between the domain images during the switching processes (Figure 7.6 (b,c)), which show similar locations and shapes of the growing reverse domains. This indicates that the nucleation sites and the local distribution of pinning sites that affect the reverse domain growth do not change substantially during the reduction process. However, the E -induced switching proceeds at much lower (constant) H , which points to a substantially reduced pinning strength. These observations can be explained considering the electrochemical effect on the grain boundaries as pinning sites. The local distribution of the grain boundaries remains similar upon reduction/oxidation processes, since the boundaries between the randomly oriented grains do not disappear. Their pinning strength, however, decreases strongly from the oxidized (non- or weakly-magnetic) to the non-oxidized (magnetic) state during the voltage-triggered reduction process (as discussed in Section 7.4). The voltage-induced change of equilibrium domain size indicates that at a local scale, the voltage-induced switching of magnetization should proceed even without an additional external magnetic field.

Currently, this effect cannot be resolved because of the very fine magnetic microstructure at remanence, in conjunction with the limited resolution of our in-situ Kerr microscope set up (which relies on objective lenses with long working distance, i.e. limited resolution and magnification). However, the effect may be observable by in-situ magnetic force microscopy. The voltage-induced displacement of the domain walls, either by modified domain-wall interactions or a change of the pinning strength, could be of interest for domain-wall logic concepts [130]. In comparison to domain size modulations achieved by capacitive electronic charging in a sub-nanometer Co layer when applying ± 10 V [67], the present ionic mechanism for domain size control requires a much lower voltage (1 V) and opens the door to a non-volatile setting of the local magnetization.

7.6 Energy efficiency and application potential for data storage and actuation

In the electrochemical approach presented here, voltage-induced changes in phase and microstructure allow the reversible tuning of technologically important magnetic properties at room temperature. For example, during the process of writing in magnetic storage devices, the state with low H_C and associated easy magnetization switching, could be set by voltage. As compared with heat-assisted magnetic recording, where the decrease in H_C and switching of magnetization are controlled by laser heating, the control of H_C by voltage is a more energy-efficient and possibly simpler setup, even though addressing a single bit by an electric field remains an engineering challenge. We evaluate the switching energy required for changing H_C , M_R , and the direction of magnetization from the time integral of the measured electric current multiplied by the applied voltage. An energy of 121 mJ is calculated for switching the large area (38.5 mm²) and for the switching time of 60 s. To facilitate

comparison with current memory devices, the energy per typical bit area was evaluated within a simple model assuming a linear dependency between switching energy and device area. For a circular area with a diameter of 50 nm (3 nm), typical for high density longitudinal (perpendicular) magnetic recording media, this calculation yields a switching energy of 618 fJ (5 fJ). These energy values approach the order of magnitude of the lowest reported switching energies, namely 6 fJ for a magnetic tunnel junction device with 50 nm diameter, switched in a much shorter time of 0.5 ns. [131–133] Previous studies on memristive systems have shown that reduction/oxidation based mechanisms [132,133] can also yield switching times down to the sub-ns regime. This indicates that the presented electrochemical mechanism can yield an improvement in the energy efficiency of several orders of magnitude. The ionic mechanism could be applied imminently to magnetic films with higher and/or perpendicular magnetic anisotropy to achieve stable magnetization at small bit size. For example, for a granular high density FePt media, a reduction/oxidation-tunable FeO_x/Fe overlayer [13] could be exploited in a similar manner to achieve voltage-induced decoupling and coupling of the FePt grains and, thus, tunable H_C . As an alternative, higher anisotropy and stability of magnetization may be possible via the exchange-bias effect achieved in combination with an antiferromagnetic underlayer.

The demonstrated energy-efficient switching of H_C and M_R , both of which are key parameters for the energy product of magnetic materials, could also be applied in micro- and nanoactuation. At present, integrated electromagnets offer flexibility in field strength as well as easy ON/OFF switching at the microscale, but they require sophisticated coil design, are limited in field strength, and cause undesired Joule losses. [134] Further, the energy consumption of microelectromagnets increases strongly with decreasing dimension, which impedes their use at the nanoscale. [135] Our study points to a fundamentally new route toward tunable nanomagnets with voltage-programmable energy product and associated magnetic stray fields, and thus toward a low power alternative to microelectromagnets.

The ionic mechanism presented here works for films covered by native oxide layer and thus does not require specific preparation or surface treatment. This robustness presents a key advantage over other magnetoelectric tuning mechanisms. Moreover, large reversible effects are obtained in ferromagnetic metal films beyond the ultrathin limit in ambient conditions and at room temperature, a combination that is not yet possible with conventional magnetoelectric approaches.

7.7 Interim conclusion

We demonstrate a fully reversible low-voltage-induced collapse of H_C and M_R in FeO_x/Fe thin films at room temperature, accompanied by large anisotropy and domain structure changes. The magnetic changes are induced by the reversible reduction and re-oxidation of the FeO_x layer. Detailed analysis of the impact of this phase change on the magnetic hysteresis and domains indicates a voltage controlled de-blocking mechanism, connected to changes in the microstructure and the structure of magnetic domains.

In the initial (oxidized) state, a blocked state that exhibits a large hysteresis for the hard axis direction is stabilized by Néel wall interactions. Upon reduction of the FeO_x, the

increase in anisotropy and Fe-layer thickness can lead to a larger domain wall energy, and thereby cause the observed increase in domain size. As a result of the coarsening of the magnetic microstructure, the domain-wall interactions are weakened, and the magnetically blocked state is suppressed. This is followed directly by the voltage-induced switching from a large hysteresis along the hard axis to ‘close to ideal’ hard-axis behavior. The decreased pinning strength of the grain boundaries upon FeO_x reduction can cause the collapse of the H_C along all other directions.

The apparent contradiction that a decreased H_C is obtained at increased anisotropy can be resolved by accounting for the role of the microstructure and the magnetic domains. H_C and anisotropy thus do not need to necessarily scale with each other, an important consideration for the electrochemical control of materials involving changes in phase and microstructure. This consideration opens a route beyond the state-of-the-art of electrochemical control of thin-film, in which extrinsic properties such as H_C are usually changed by controlling the intrinsic perpendicular magnetic anisotropy. The voltage-induced modification of local defects presents a paradigm change in ionic control of magnetism, which so far commonly affect the interface or the bulk of the material as a whole. For the local control of defects only a small portion of the material needs to be affected. This promises a higher energy efficiency and faster speed than conventional magneto-electric approaches. The electrochemical mechanism presented in this paper fulfills the important requirements of room temperature and ultralow power operation of future magnetic devices, especially in the fields of magnetic memory, domain wall logic, neuromorphic computing, and magnetic actuation devices. The mechanism of voltage-controlled defects may be transferrable to many other defect-controlled materials, such as type II superconductors or materials with specific mechanical properties.

With chapter 5, 6 and 7, we fulfilled the first objective of the presented thesis, namely: To directly observe, for the first time, magnetic microstructure changes of magnetic thin films with in-plane magnetization in a liquid electrolyte during simultaneous voltage-triggered electrochemical reactions. These findings provide new insights into the mechanisms of voltage controlled magnetic properties by electrochemical reactions.

8 Voltage control of FeO_x/Fe/IrMn thin films with in-plane unidirectional anisotropy

The results of chapter 8 are also published in [2] within the framework of this thesis. The respective paragraphs – with minor adjustments – are indicated in grey font. Reprint from [2] under permission from © 2019 WILEY-VCH Verlag GmbH & Co. KGaA, Weinheim

So far, we were able to demonstrate significant voltage-induced magnetic changes of a FeO_x/Fe thin film system with in-plane uniaxial anisotropy. Within this section, a ferromagnetic (FM) FeO_x/Fe layer is placed in contact with an underlying antiferromagnet (AFM) IrMn. This combination gives rise to a unidirectional anisotropy and finally tunable exchange bias (EB).

8.1 Characterization of the pristine state exchange biased thin films

The typical layer architecture and morphology of the FeO_x/Fe/IrMn system after preparation is shown in the cross-section bright-field transmission electron microscopy (TEM) image in **Figure 8.1 (a)**. The film consists of columnar IrMn and Fe grains which are covered by a native FeO_x. The native oxidation leads to a decrease in the Fe layer thickness d_{Fe} by ≈ 2 nm in comparison to the nominal Fe layer thickness $d_{\text{Fe,nom}}$. This is as expected for room temperature oxidation of Fe in ambient conditions. [136] The magnetization curves of the pristine exchange bias (EB) systems with $d_{\text{Fe,nom}} = 5, 7, 9, 11,$ and 13 nm are displayed in **Figure 8.1 (b)**. All exhibit an EB with a full shift of the magnetization curves. A systematic shift of the curves towards smaller $|H_{\text{EB}}|$ is observed upon increasing $d_{\text{Fe,nom}}$. The same trend holds for the H_{C} for $7 \text{ nm} \leq d_{\text{Fe,nom}} \leq 13 \text{ nm}$. This superposition of similar trends for $-H_{\text{EB}}$ and H_{C} leads to the situation that for different Fe thicknesses, that there is a significant difference in the field shifts for the individual hysteresis branches towards negative saturation, whereas the difference in the shift of the hysteresis branches towards positive saturation is less strongly pronounced. The hysteresis for the system with $d_{\text{Fe,nom}} = 5$ nm differs from the systems with larger $d_{\text{Fe,nom}}$ with regard to both curve shape and H_{C} . The inset in **Figure 8.1 (b)** reveals that, as expected for the interface-dominated EB effect, [36] H_{EB} is inversely proportional to d_{Fe} , where d_{Fe} is approximated as $d_{\text{Fe}} = d_{\text{Fe,nom}} - 2$ nm based on **Figure 8.1 (a)**. The smaller EB at larger $d_{\text{Fe,nom}}$ can thus be directly explained by the weaker impact of the Fe/IrMn interface in comparison to that of the film volume. In addition, H_{C} also almost inversely scales with d_{Fe} for all $d_{\text{Fe,nom}} > 5$ nm. This is a reasonable behavior, as additional anisotropy and thus H_{C} contributions in EB systems are known to originate from the FM/AFM interface. [137] Similar trends for H_{EB} and H_{C} have been observed in FeCo/IrMn [138] and Fe/MnPd [137] EB heterostructures. The deviation observed at $d_{\text{Fe,nom}} = 5$ nm indicates that at this thickness, a limitation for the FM/AFM layer model is reached in the present case. This is understandable since the intergranular oxidation (see **Figure 8.1 (a)**) at this small $d_{\text{Fe,nom}}$ is expected to result in separated Fe nanoislands and thus a fundamentally different morphology.

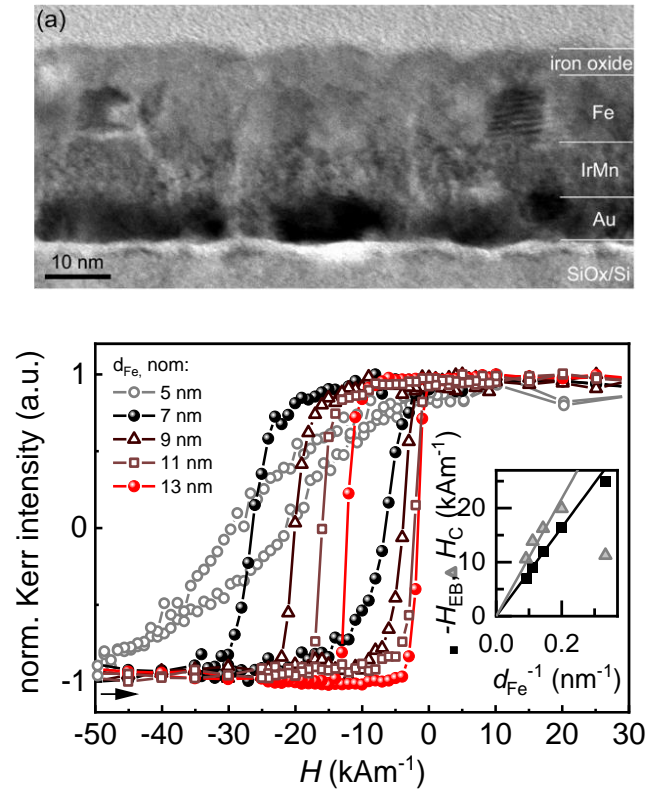


Figure 8.1: Layer architecture and ferromagnetic layer thickness dependence of the FeO_x/Fe/IrMn exchange bias systems.

a) Cross-sectional bright field TEM image of the as-deposited layer stack with $d_{\text{Fe,nom}} = 13$ nm. b) In-plane magnetization curves for systems with different nominal Fe layer thicknesses. The inset shows $-H_{\text{EB}}$ and H_{C} scaled at d_{Fe}^{-1} and respective linear fits to the data (for $7 \text{ nm} \leq d_{\text{Fe,nom}} \leq 13 \text{ nm}$). Error bars for $-H_{\text{EB}}$ and H_{C} are below the symbol size.

The strong correlation between the EB and the Fe layer thickness offers an elegant means for the voltage-control of the EB by electrochemical modification of the top Fe layer. Previous studies on Fe thin films concluded that approximately 2 nm of an FeO_x layer can be transformed into approximately 1.5 nm of an Fe layer, and vice versa, by electrolyte gating. [139] Such a thickness variation, according to Figure 1b, should yield significant changes in H_{EB} and H_{C} in the present EB systems, with larger effects expected at smaller d_{Fe} .

8.2 Electrochemical modification of EB – voltage dependency

For the potential (E)-induced manipulation of the FM layer thickness and, consequently, the EB, an aqueous alkaline electrolyte ($1 \text{ mol l}^{-1} \text{ LiOH}$) is chosen, in which the electroreduction of FeO_x layers to metallic Fe layers can be achieved at room temperature. [139,140] The electrochemical treatment and the magnetic measurements are simultaneously carried out in an in situ Kerr microscope setup (chapter 5).

The electrochemical behavior of the FeO_x/Fe/IrMn system in the electrolyte is characterized by cyclic voltammetry (see appendix, Figure 12.8). **Figure 8.2** (a) shows the current density-potential-curve $j(E)$ in the potential range of $-0.95 \text{ V} > E > -1.1 \text{ V}$, in

which the reduction of Fe occurs. The increase of the cathodic j confirms the enhancement of the reduction reaction when polarizing in the cathodic (negative) direction.

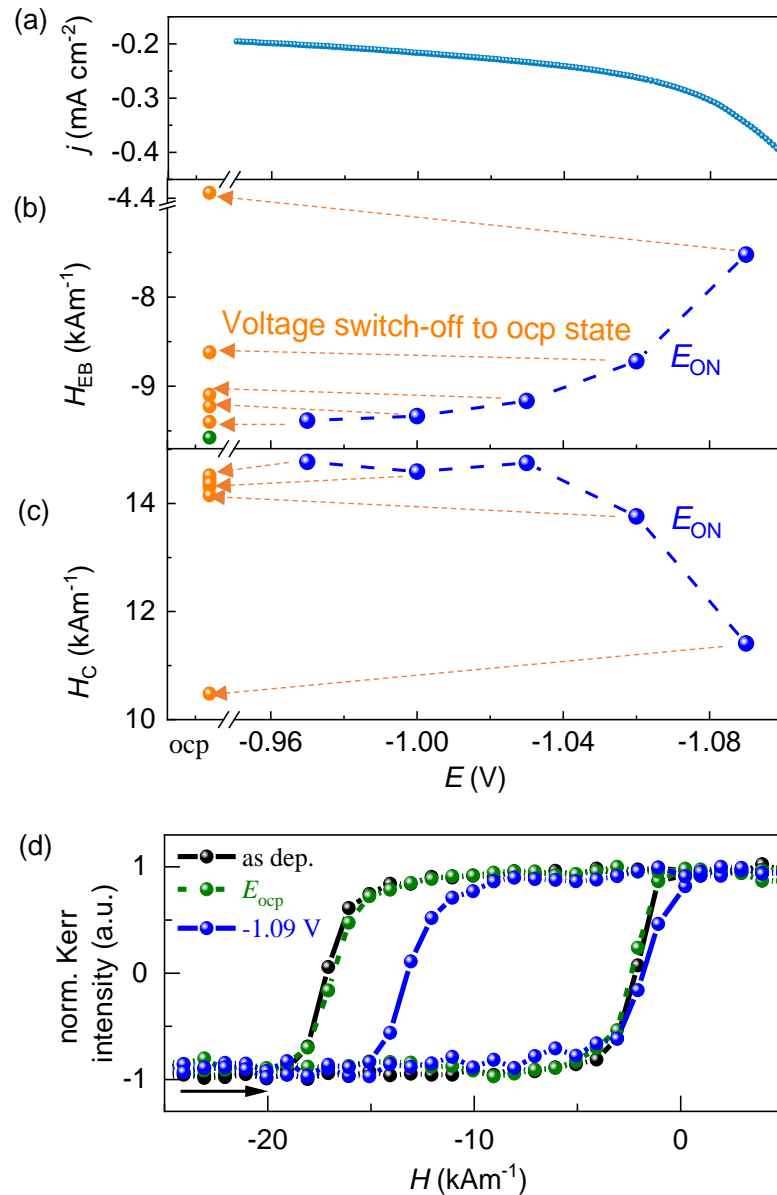


Figure 8.2: Electrochemical modification of EB in FeOx/Fe(11nm)/IrMn systems.

(a) $j(E)$ -curve measured at a rate of 10 mV/s. (b) H_{EB} and (c) H_C obtained during (blue dots) and after (orange dots) potentiostatic polarization at selected E for 60 s. Error bars for H_{EB} are below the symbol size and the dashed lines are a guide to the eye. (d) Magnetization curves for the film in as-deposited, ocp and polarized states showing the voltage-induced EB shift obtained at $E = -1.09$ V. All data in (b, c, d) is collected in the exact same sample area. bars for H_{EB} and H_C are below the symbol size.

The magnetic property changes upon electrochemical reduction of an FeO_x/Fe/IrMn EB system are shown in **Figure 8.2** (b,c), and e for $d_{\text{Fe,nom}} = 11$ nm. The measurements were carried out in situ on the exact same area. First, the magnetization curve is measured in the pristine state and after electrolyte addition in the open circuit potential (ocp) state. The comparison of these two magnetization curves (**Figure 8.2** (d)) reveals that the films are stable in the electrolyte and that the pure electrolyte contact does not alter the magnetic properties. Selected reduction potentials are then applied in a stepwise potentiostatic routine, starting at $E = -0.97$ V and ending at $E = -1.09$ V. The potentials are held for 60 s, which is the time required for acquiring a single magnetization curve measurement. After each potential step, E is switched off and the magnetization curve is measured again to probe the (non)volatility of the E -induced changes. Magnetization curves of the pristine state and during/ after voltage application are exemplarily depicted for $E = -1.06$ V in the appendix (**Figure 12.9**). The extracted H_{EB} and H_{C} values are plotted in **Figure 8.2** (b) and (c), respectively, as a function of E . In the polarized state, lower $|H_{\text{EB}}|$ values are measured towards more cathodic (negative) E . **Figure 8.2** (d) shows the strong hysteresis change observed when applying $E = -1.09$ V.

For E more positive or equal to -1.06 V, the voltage-induced H_{EB} shifts are retained after the voltage is turned off (orange symbols), revealing the nonvolatile nature of the modification. For $E = -1.09$ V, the EB strongly reduces further after voltage switch-off. For H_{C} , similar nonvolatile behavior as for H_{EB} is observed.

The observed voltage-induced magnetic modifications are discussed in the following section with respect to the electrochemical mechanisms. The E -induced reduction of an FeO_x layer in alkaline solution has been shown to start at the FeO_x/Fe interface and not at the electrolyte/FeO_x interface. [140] As a consequence, the reduction process is expected to lead to an increase in the FM layer thickness d_{Fe} , which, in conjunction with **Figure 8.1**, could directly explain the decrease of EB upon electrochemical reduction. The larger H_{EB} change observed at a more cathodic E is consistent with the increased cathodic j and thus the higher reduction reaction rate.

The stability of the E -induced H_{EB} modification for E being more negative or equal to -1.06 V after the voltage was turned off shows that this electrochemical routine can be employed to set specific H_{EB} values by utilizing E as a control parameter. One explanation for the stability of the partially reduced state is that the remaining FeO_x protects the underlying, modified, Fe layer. This hypothesis is supported by previous TEM investigations of epitaxial FeO_x/Fe/FePt heterostructures, in which an increased Fe layer thickness protected by FeO_x is observed after the electrochemical reduction process. [139] For $E = -1.09$ V, this stability is no longer present. The instability might be associated with proton reduction, which becomes pronounced as a side reaction at more cathodic potentials. [141] In this case, a more complex electrode/electrolyte situation is expected, involving, e.g., a local pH increase [142] and hydrogen absorption and embrittlement [143], where both processes could lead to an irreversible modification of the EB heterostructure.

8.3 Electrochemical modification of EB – time dependency

To prevent film instability, $E = -1.03$ V is chosen for the reduction in the following experiments. **Figure 8.3** shows that the H_{EB} and H_C changes can be substantially increased when the reduction time t_r is prolonged. This indicates that after 60 s (**Figure 8.2**), only a partial transformation of the native FeO_x layer occurred. For a full transformation of 3 nm FeO_x (as estimated from **Figure 8.1** (a)), an increase of d_{Fe} by 2 nm can be expected. For this situation, the required charge is compared with the measured electrochemical data in the following section. For the electrochemical reduction of Fe ions to a metallic Fe layer with a thickness d_{Fe} , according to the reaction $Fe^{z+} + ze^- \rightarrow Fe$, the charge density q can be calculated via Faraday's law:

$$Q' = m_{Fe} z F M^{-1} \quad (1) \quad \text{and} \quad q = Q'/A_A = \rho_{Fe} d_{Fe} z F (M)^{-1} \quad (2)$$

where Q' is the electrical charge, m is the mass of Fe, ρ_{Fe} is the density of Fe, the layer area $A_A = 1$ cm², F is the Faraday constant and (M) is the molar mass of Fe. It is widely agreed that Fe ions of a valence of 2+ and 3+ are present in a native oxide layer after room temperature oxidation of polycrystalline Fe in ambient air. [136,144,145] Therefore, two limiting cases with $z = 2$ and $z = 3$ are calculated. This calculation yields 2.7 mC cm⁻² (in the case of Fe²⁺ ions) and 4.0 mC cm⁻² (in the case of Fe³⁺ ions) as the charge density required to form one nanometer of the metallic Fe layer. In **Figure 8.3** (b), these values are compared to the experimental q extracted from the $j(t_r)$ curves by integration. The comparison shows that the transferred q is sufficient for the formation of several nanometers of metallic Fe when the reduction time is sufficiently long. Within the first 60 s of reduction, $q = 5.2$ mC cm⁻² is transferred. This corresponds to a maximum possible Fe layer thickness between 1.3 nm (assuming Fe³⁺ reduction) and 1.9 nm (assuming Fe²⁺ reduction) when 100% current efficiency is assumed. The calculation overestimates the transformed thickness because it cannot account for proton reduction as a side reaction, which lowers the current efficiency. However, the estimate still proves that the full transformation of the native oxide layer, involving the formation of a 2 nm thick Fe layer, cannot proceed within the first 60 s at $E = -1.03$ V and requires prolonged reduction times. This agrees with the observed t_r -dependence of the EB (**Figure 8.3** (a,c)), where after $t_r = 60$ s the E -induced shift in the EB is still small. However, when prolonging t_r , the E -induced H_{EB} observed in the heterostructure with $d_{Fe,nom} = 11$ nm indeed approaches the H_{EB} of an as-deposited film with a 2 nm larger thickness, i.e., $d_{Fe,nom} = 13$ nm. In contrast to the EB(t_r) behavior, the E -induced H_C values at longer t_r (**Figure 8.3** (d)) decrease well below the H_C of the as-deposited heterostructure with $d_{Fe,nom} = 13$ nm. This can be understood, as the H_C values not only depend on the FM/AFM interface but are also strongly linked to the microstructure of the FM layer. The pronounced E -induced decrease in H_C indicates that the reduction process alters the microstructure of the FM layer. In the present granular films the reduction of grain boundary oxides, and hence a resulting decreased number of domain wall pinning sites in the Fe layer, may explain the larger

decrease of H_C . A similar mechanism was recently proposed for electrolyte infiltrated nanoporous CoPt, in which a partial reduction of CoO to Co resulted in a decreased H_C . [146]

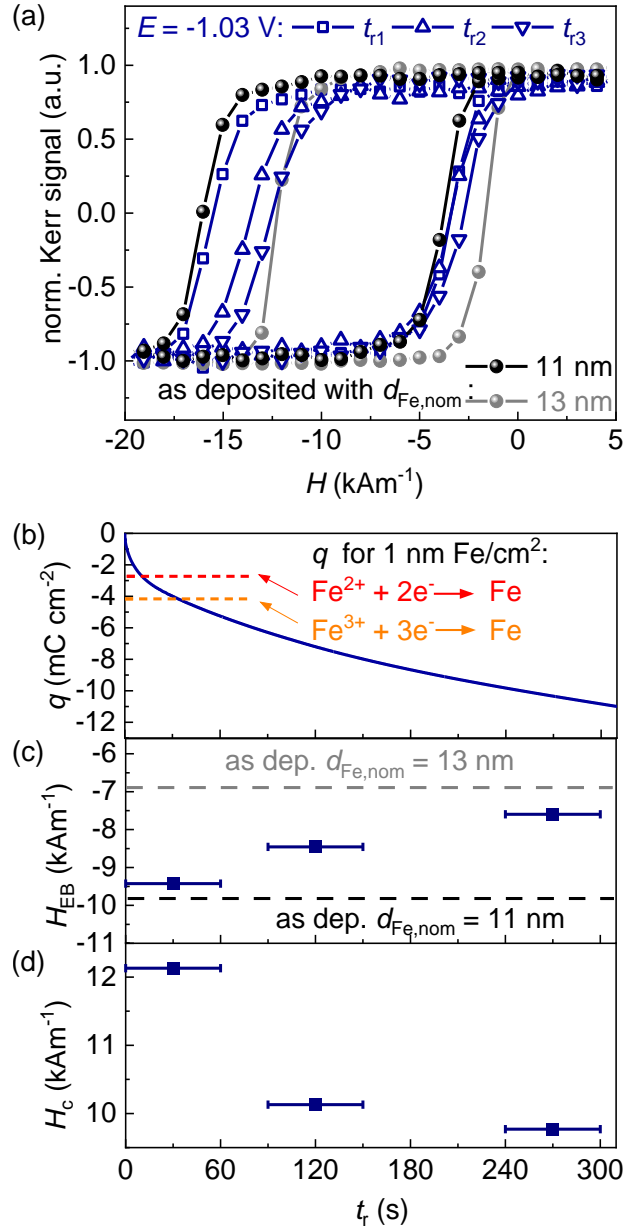


Figure 8.3: Control of the magnetic properties of an EB system by the reduction time.

(a) Magnetic hysteresis of an FeO_x/Fe/IrMn system with $d_{\text{Fe,nom}} = 11$ nm in as-deposited state and during continuous polarization at $t_{r1} = 0$ -60 s, $t_{r2} = 90$ -150 s and $t_{r3} = 240$ -300 s after the start of the voltage application. The data is collected in the exact same sample area. The magnetic hysteresis of an as-deposited FeO_x/Fe/IrMn heterostructure with $d_{\text{Fe,nom}} = 13$ nm is added for comparison. (b) Transferred charge density q as a function of t_r . For comparison, q required to form a 1 nm thick Fe layer from Fe²⁺ or Fe³⁺ ions is indicated. (c) H_{EB} and (d) H_C as extracted from (a) plotted as a function of t_r in comparison to the as-deposited states (dashed lines). Error bars for H_{EB} and H_C are below the symbol size.

At this point, it can be concluded that, E and t_r can be independently employed to control the amount of transformed FeO_x within certain potential limits. Thus, the electrochemical mechanism promises to be a versatile method for a voltage-programmable EB.

For a direct comparison of the effects due to electrochemical polarization and the Fe layer thickness, the electrochemical modification of the EB was investigated for different $d_{\text{Fe,nom}}$. In a simple layer model, the electrochemical reduction is expected to transform a similar thickness of FeO_x into Fe independent of the thickness of the underlying Fe layer. This is consistent with the measured $j(t)$ and transferred q that are similar for the different Fe thicknesses $d_{\text{Fe,nom}}$ (**Figure 8.4** (a)). Figure 8.4 (b) and (c) shows that the application of -1.03 V in all cases induces a decrease in $|H_{\text{EB}}|$ and, except for $d_{\text{Fe,nom}} = 5$ nm, also a decrease in H_{C} . In line with expectations, the E -induced EB shift strongly increases when proceeding towards smaller $d_{\text{Fe,nom}}$.

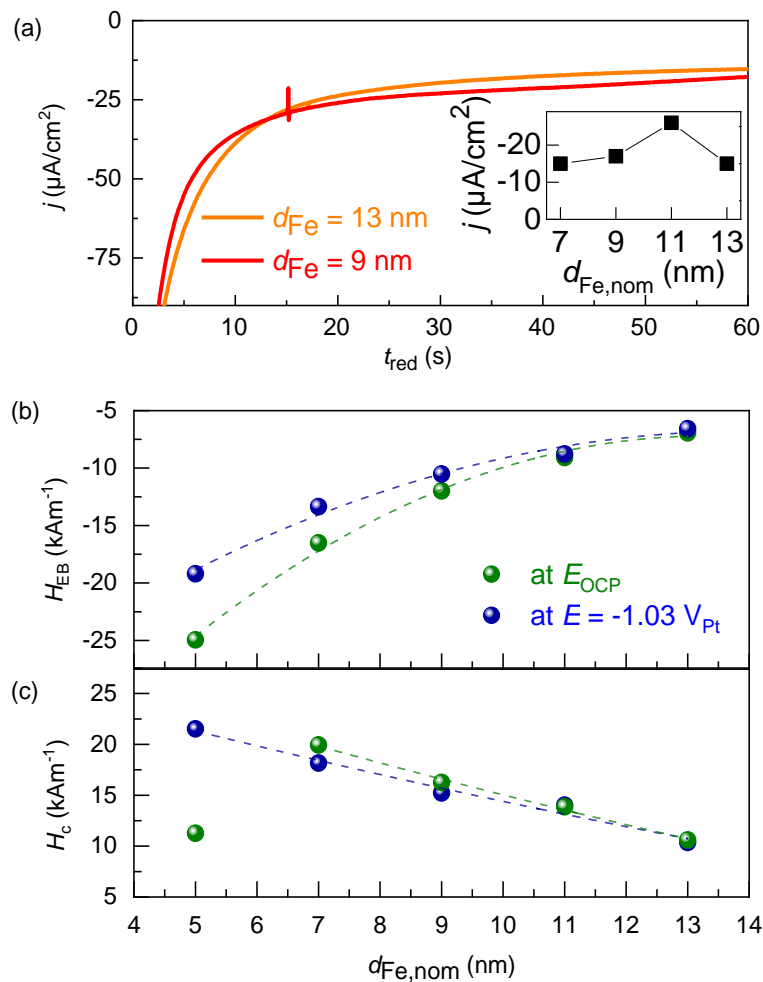


Figure 8.4: FM layer thickness dependence of E -induced EB and H_{C} change.

(a) Exemplary $j(t_r)$ curves obtained at $E = -1.03$ V for different $d_{\text{Fe,nom}}$; the inset depicts the charge q transferred after 60 s as a function of d_{Fe} . E -induced (b) H_{EB} and (c) H_{C} obtained for different $d_{\text{Fe,nom}}$ in comparison to the states at E_{OCP} . Error bars for H_{EB} and H_{C} are below the symbol size. Dashed lines are a guide to the eye.

8.4 Model for voltage control of EB by electrochemistry

By using a simple model for the EB, the FM layer thickness dependence of H_{EB} can be described analytically by considering the FM layer properties (M_{Fe} as the saturation magnetization of the FM) and the AFM/FM coupling constant J_B [36].

$$H_{EB} = -\frac{J_B}{\mu_0 M_{Fe} d_{Fe}} \quad (3)$$

Note that the actual Fe layer thickness d_{Fe} set by the electrochemical reduction cannot be directly probed in situ. However, because the reduction reaction proceeds at the FeO_x/Fe interface, [140] the FM/AFM interface and the AFM properties defining J_B [36] can be assumed constant. Thus, according to equation (3), no change in the slope of H_{EB} (d_{Fe}^{-1}) is expected for the electrochemical manipulation of the FM layer thickness. In **Figure 8.5**, different scenarios from no to a full transformation, are compared. The plot of the voltage-induced H_{EB} vs. d_{Fe}^{-1} reveals that the slopes differ in comparison to the ocp states for the two limiting cases: (I) that all FeO_x is reduced to Fe ($d_{Fe} = d_{Fe,nom}$) and (II) that no FeO_x is reduced to Fe ($d_{Fe} = d_{Fe,nom} - 2 \text{ nm} = d_{Fe,ocp}$). Case (II) even yields unreasonable nonlinear behavior. A fit with the same slope of H_{EB} (d_{Fe}^{-1}) as for the ocp states is obtained when assuming that the reduction leads to an increase of the Fe layer thickness by 1.1 nm within 60 s. This is quite reasonable with regard to previously observed t_r -dependence of H_{EB} and the analysis of q (**Figure 8.3** (a) and (b)).

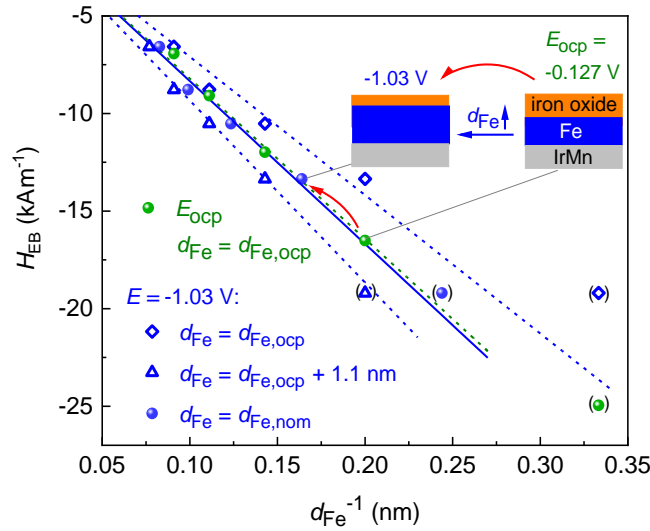


Figure 8.5: Correlation of the electrochemical EB modification with a partial reduction of the FeO_x and associated Fe layer thickness increase.

The E -induced H_{EB} shift from Figure 8.4 b is scaled at d_{Fe}^{-1} for three cases: (I) d_{Fe} set as $d_{Fe,nom}$, corresponding to a full reduction of FeO_x, (II) d_{Fe} set as $d_{Fe,ocp}$ corresponding to no reduction of FeO_x and (III) d_{Fe} set as $d_{Fe,ocp} + 1.1 \text{ nm}$, corresponding to a partial reduction of FeO_x. The EB states at E_{ocp} with $d_{Fe} = d_{Fe,ocp} = d_{Fe,nom} - 2 \text{ nm}$ are given for comparison. The lines are linear fits to the data (intercept at zero, not considering the data for $d_{Fe,nom} = 5 \text{ nm}$ marked with brackets). For the data obtained for $d_{Fe,nom} = 7 \text{ nm}$, the sketch visualizes the proposed E -induced change in d_{Fe} .

It can be concluded that within the time frame of 60 s, the complete FeO_x layer is not transformed. The nonvolatility observed after voltage application and switch-off (Figure 8.2 (b)) can then be explained by the remaining oxide which functions as a protective layer. This agrees with a previous study [139] in which a protecting oxide that is thinner than the oxide formed by natural oxidation was imaged after electrochemical reduction of the native FeO_x on Fe layers. In this study, [139] imaging was carried out after electrolyte removal and handling in air, which confirms that this thinner oxide is protective and does not thicken when in contact with ambient conditions. In the present case, the remaining oxide freezes in the E -programmed EB states and thus acts as a key to achieve nonvolatility.

An analysis of the influence of t_r and $d_{\text{Fe,nom}}$ revealed that the reduction process is consistent with a t_r -dependent increase of d_{Fe} underneath a protecting oxide layer within the time frame of several tens of seconds. This offers the possibility that, in addition to E , t_r can be employed as a control parameter to set different EB states in a nonvolatile manner.

8.5 Non-volatile and reversible voltage control of exchange bias

The presented concept, of the Fe layer thickness change, is confirmed by subsequently polarizing an FeO_x/Fe/IrMn film with $d_{\text{Fe,nom}} = 13$ nm at $E = -1.03$ V for different t_r and measuring the magnetic properties during voltage application and voltage switch-off. Selected magnetization curves are presented in the Appendix in Figure 12.9. **Figure 8.6** (a) shows that a stepwise and nonvolatile change in H_{EB} can be achieved by a repetitive voltage application even if it is intermittent due to a voltage switch-off of several minutes. The switch-off states were always held until E_{ocp} reached the initial value again. In this time frame, some fluctuations of the H_{EB} values occur, but the stepwise change in H_{EB} when comparing the consecutive switch-off steps can still be clearly attributed to the previously applied voltage. The nonvolatility was confirmed after complete removal of the electrolyte. A partly reversible EB change is observed during additional measurements for the second and third polarization steps in Figure 8.6 (a). Here, the decrease of $|H_{\text{EB}}|$ during voltage application ((1) → (2)) is followed by partial recovery of H_{EB} after voltage switch-off ((2) → (3)). Respective magnetization curves are plotted in Figure 8.6 (b). This reversibility can be understood by considering the long (accumulated) reduction time. When the reduction process proceeds for a sufficiently long time, the full FeO_x layer will be transformed at some point and lead to unprotected Fe being present at the electrode/electrolyte interface. In the polarized state, this metallic Fe is stabilized by the reduction potential (-1.03 V). However, during voltage switch-off, reoxidation of the Fe surface takes place and, compared to the state at -1.03 V, causes a decrease in d_{Fe} and an associated increase in H_{EB} . The re-oxidation in this case is faster than the reduction because it starts at the Fe surface in direct electrolyte contact, whereas the reduction process relies on ionic migration through the initially 3-4 nm thick oxide

layer. [140] During the third reduction step in Figure 8.6 (a), an even further decrease of $|H_{EB}|$ is recorded, followed again by a reversible behavior after voltage switch-off. This behavior indicates that the full reduction of FeO_x and thus contact of metallic Fe to the electrolyte does not occur at the same time throughout the whole sample surface but may proceed in a nonuniform manner. This is reasonable for the granular morphology and associated local variation of FeO_x thickness Figure 8.6 (c) shows that full reversibility can be achieved when subsequent to the reduction potential, instead of voltage switch-off, an oxidation potential ($E = -0.02\text{V} > E_{ocp}$) is applied. In this case, voltage-induced re-oxidation of previously transformed metallic Fe and the formation of a thicker FeO_x layer is expected and can explain the associated increase of both $|H_{EB}|$ and H_C . H_{EB} and H_C can be repeatedly switched by this routine (Figure 8.6 (d)). Reversibility for several hundreds of cycles can be expected in this electrochemical system [147] but may require careful adjustment of reduction/oxidation potential and potential switching routines. [141] The observed reversible behavior of EB indicates that the Fe/IrMn interface, which is responsible for the EB, remains unchanged.

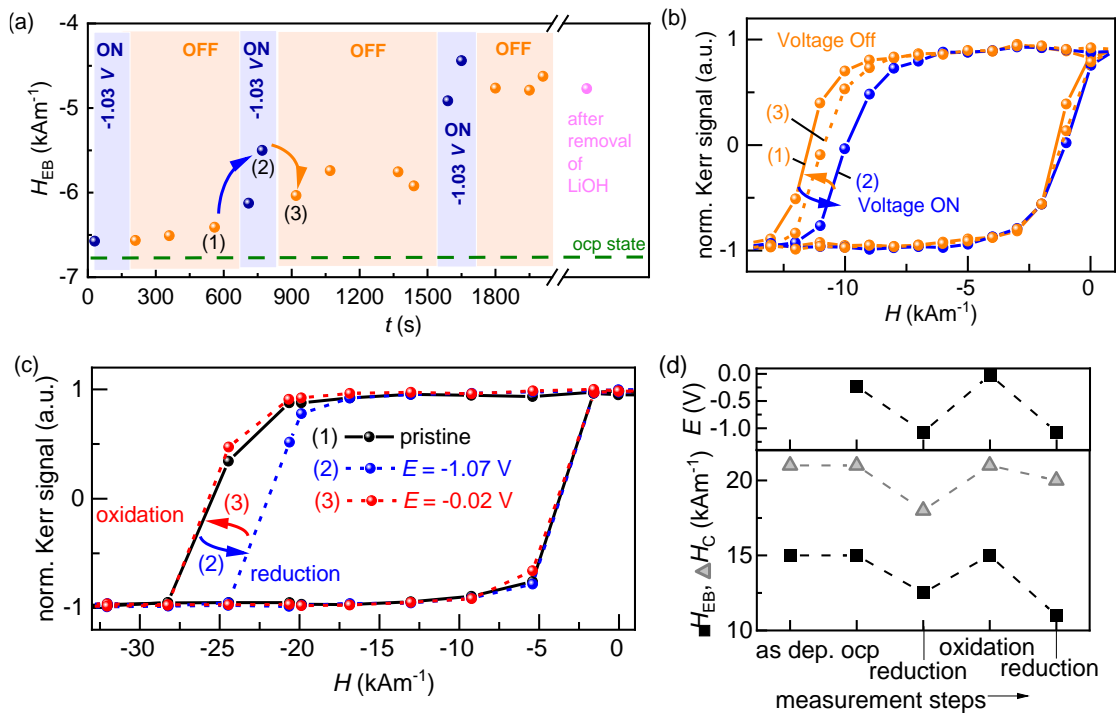


Figure 8.6: Non-volatile and partly reversible setting of EB by voltage.

a) EB evolution during a sequence of voltage ON/OFF switching obtained for an FeO_x/Fe/IrMn heterostructure with $d_{Fe,nom} = 13$ nm. Arrows mark the partly reversible change of H_{EB} when switching the voltage ON and OFF. b) The partial reversibility of the E-induced change of EB is depicted by a comparison of the hysteresis obtained after 150 s in ON state (2) and those obtained in the previous (1) and subsequent (3) OFF states (orange full and dashed lines, respectively). c) Magnetization curves exhibiting a fully reversible change of H_{EB} and H_C when subsequently applying reduction (2) and oxidation (3) voltages. The hysteresis of the pristine state is added for comparison. d) H_{EB} and H_C values obtained by repeated reduction and oxidation in comparison to pristine and ocp states. Error bars are below the symbol size and all data is collected in the exact same areas of the two samples utilized for (a,b) and (c,d).

8.6 Nonvolatile change of oxidation state and layer thickness

Angle-resolved X-ray photoelectron spectroscopy (XPS) was carried out to probe the non-volatile change of the oxidation state induced by the electrochemical reduction and subsequent voltage switch-off. In **Figure 8.7** (a,b) sections of Fe electron binding energy spectra measured in the same area before and after electrochemical reduction and voltage switch-off are compared. Prior to electrochemical polarization, a large FeO_x component is measured and a small contribution of metallic Fe is only detected for the highest incidence angle (75°). After prolonged treatment at -1.03 V, a strong increase of the peak related to metallic Fe is measured for all incidence angles. This proves the voltage-induced reduction of the native FeO_x layer to metallic Fe and the presence of a thinner yet protective FeO_x layer after voltage switch-off. At the FeO_x/Fe layer surface after electrochemical treatment, Mn impurities are detected by XPS, with a decreasing intensity at higher angles of incidence and after sputtering part of the FeO_x/Fe layer. A possible explanation is that at a few defective sites in the large treated area (38.5 mm²) Mn dissolution into the electrolyte followed by redeposition on the surface occurred. On a local scale, cross-sectional TEM images of the treated area in comparison to the untreated as-deposited area outside the electrochemical cell reveal that the layer structure is still intact (**Figure 8.7** (c,d)).

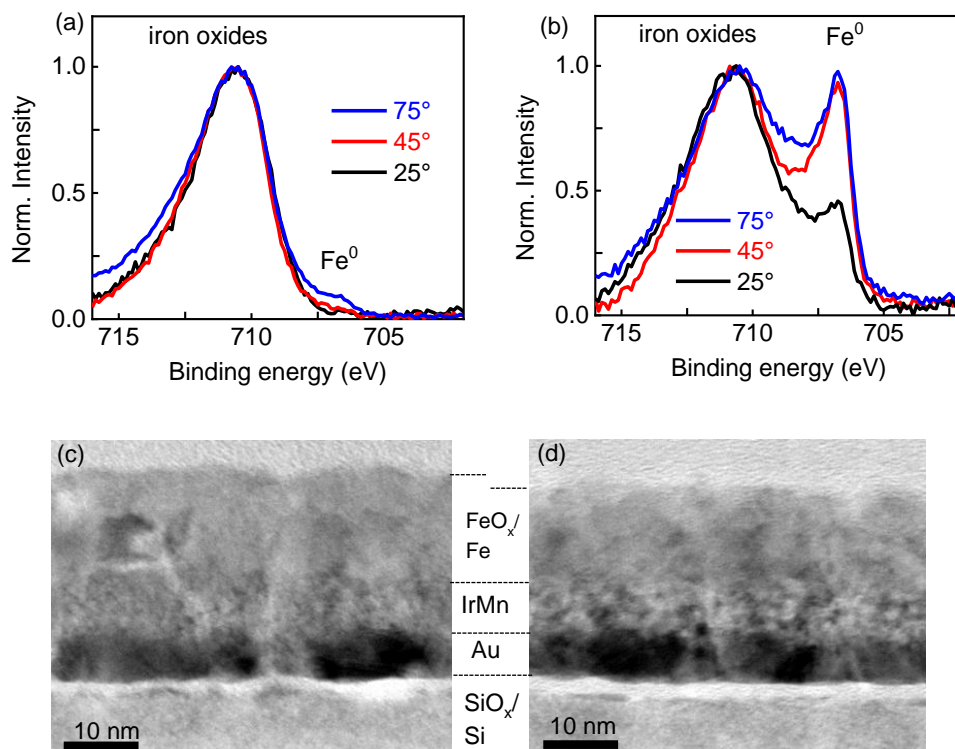


Figure 8.7: Non-volatile voltage-induced change of oxidation state and layer thickness for an FeO_x/Fe/IrMn exchange bias system with $d_{\text{Fe, nom}} = 13$ nm.

(a,b) Angle-resolved Fe2p_{3/2} XPS spectra in the same area (a) before and (b) after electrochemical polarization at -1.03 V for 600 s. (c,d) Cross-section bright-field TEM images obtained (a) in the

outer unaffected area, and (b) in the inner area which has been modified by the electrochemical routine displayed in Figure 8.6 a.

The observed decrease of the FeO_x/Fe layer thickness in Figure 8.7 (d) is in accordance with the expected volume reduction during the transformation of FeO_x to Fe. The interface between metallic Fe and FeO_x cannot be identified unambiguously, which seems mainly related to the very small grains present in the layers. One reason for grain refinement by the electrochemical phase transformation may be the presence of Li ions in the electrolyte. Li-assisted transition metal (M) oxide reduction reactions are known to induce grain refinement after several potential switching steps. [148] Because this reaction involves the electrolyte/FeO_x/Fe interfaces, this mechanism would mainly modify these interfaces, and is not expected to degrade the Fe/IrMn interface. Nevertheless, it should be noted that grain size and transformation stress/strain-related effects, in addition to the proposed layer thickness effects, might also play a role in the voltage-induced EB and especially the H_C changes. The influence of antiferromagnetic FeO (Néel temperature $T_N \sim 200$ K) [136], which may be present at the FeO_x/Fe interface, is considered negligible for the EB variations due to the room temperature operation (see Appendix Figure 12.10).

8.7 Electrochemical patterning of EB and magnetic domain state

Lateral magnetic patterning of a thin film can be envisioned by this procedure because the electrochemical reduction only proceeds in the area subjected to contact with the electrolyte. In the present case, the voltage-modified area is defined by the diameter of the electrochemical cell placed onto the EB film. The magnetic properties across the sample have been probed to confirm that local variations in pristine state are significantly smaller than the electrochemically induced changes in the patterning experiment (see Appendix Figure 12.11). In Figure 8.8, the lateral positions are described in a sketch and the associated magnetization curves and typical domain images are displayed for the two areas after the electrochemical routine as in Figure 8.6 (a) had been applied. For the same applied magnetic field H , different domain states are present for the voltage-modified and as-deposited area. When a reversed magnetic field of -12 kAm^{-1} is applied after saturation in positive H , the magnetization of the untreated area is switched by approximately 50% (point 1 in Figure 8.8) which corresponds to the coercive field, whereas the magnetization of the electrochemically treated area is almost fully switched (point 2 in Figure 8.8). This can be clearly followed by the observed domains, which for point 1 includes white and black domains equally distributed and portioned, whereas only a few dark domains are visible for point 2. Even more interesting is the behavior for the M_R after saturation in the negative field direction. In the as-deposited case, the hysteresis is fully shifted, a full 180° magnetization switching has already occurred, and a fully saturated state with no domains is reached (point 3 in Figure 8.8). However, in the voltage-treated area, approximately 70% of the magnetization is switched, and accordingly, magnetic domains are still clearly visible. This experiment proves that voltage-induced setting of magnetic

domain states is possible by exploiting reduction/oxidation reactions in the ferromagnetic layer of an EB system. Because the modification is especially large in terms of the M_R , a magnetic field will not necessarily be required for the stabilization of different domain patterns. In the present experiments, a (negative) reduction potential was utilized as a control parameter to modify the ferromagnetic layer thickness. Further versatility of the approach is expected when utilizing an anodic (oxidation) potential as an additional control parameter, after or instead of the reduction procedure. For one specific anodic potential this could already be shown (Figure 8.6 (c,d)). The careful adjustment of the oxidation potential and the potential switching regimes are promising routes towards even more variability in voltage-programmable states and long term reversibility of the proposed approach, because the nature and thickness of the protecting oxide layer on Fe are known to depend upon the electrochemical potential sequence applied. [149]

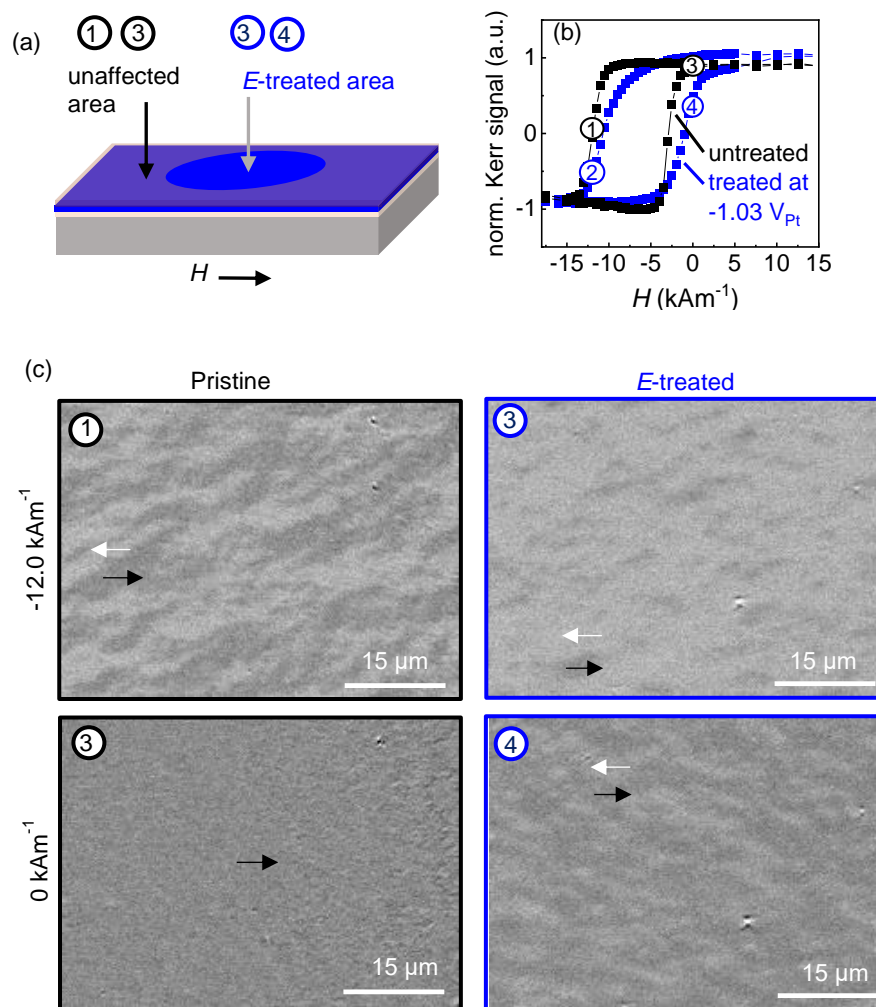


Figure 8.8: Lateral patterning of EB and magnetic domain state by voltage.

a) In situ Kerr microscopy analysis with longitudinal sensitivity is carried out on one sample by choosing lateral positions within the voltage-treated area and in the outer, unaffected area. b) Magnetic hysteresis and c) magnetic domain images obtained after electrochemical treatment (routine at -1.03 V as in Figure 6a) in comparison to the as-deposited state. For both lateral

positions, magnetic domain images are acquired at $H = -12 \text{ kAm}^{-1}$ (after saturation in $+H$) and at $H = 0 \text{ kAm}^{-1}$ (after saturation in $-H$) as marked by the numbers 1-4 in the hysteresis.

The proposed electrochemical control of the EB can enable magnetic patterning via a lithographically defined mask or local magnetic domain writing down to submicrometer scale by electrochemical micromachining, [150] when utilizing a tool electrode with reduced dimensions. The advantages of electrochemical patterning over existing vacuum and thermal EB control methods [34,81,151–153] include the room temperature operation, energy-efficiency, compatibility with CMOS technologies, and the possibility for upscaling and modification of 3D geometries. The presented geometry and the use of liquid electrolytes is favorable because the gate electrode and electrolyte can be easily removed after EB modification.

In comparison to solid-state resistive switching-based electric control by reduction/oxidation reactions in an AFM oxide via a top gate, [89] in the present geometry, a metal AFM is at the bottom while the ferromagnetic layer is covered by a native oxide, both of which are manipulated via the top gate. In this geometry, the reduction/oxidation processes are decoupled from the antiferromagnet/ferromagnetic interface, and in consequence, the electric manipulation becomes independent of the AFM properties. AFM metals instead of AFM oxides can be utilized, which is beneficial for spintronic devices because of the large accessible EB fields, the high thermal stability and in view of AFM metals as hot candidates for AFM spintronics. [154] Another advantage over the electric control of top layer AFM oxides, which is often restricted to toggling between only two EB states, [89] is that the electrochemical transformation in the Fe and FeO_x layer enables continuous non-volatile tuning of the EB. This may become especially relevant for the electric tuning of domain patterns and associated dynamic stray field landscapes in liquids, and thereby open a novel and energy-efficient route for magnetophoretic devices.

8.8 Interim conclusion

In conclusion, the nonvolatile and partly reversible voltage-induced alteration of the EB is demonstrated in an Fe/IrMn based EB system via the electrochemical modification of the ferromagnetic layer. Large EB field changes of fully shifted hysteresis loops are obtained at low voltage (1 V) and room temperature. The EB values can be continuously programmed by the magnitude of the applied voltage and/or the time of voltage application. An Fe layer thickness-dependent study and the discussion in the frame of a simple model for EB indicates that the main underlying mechanism is an E -induced reduction of the native FeO_x to Fe, leading to a thickness change in the Fe layer. Nonvolatility is achieved as the reduction process starts at the buried FeO_x/Fe interface, which enables protection by the remaining oxide layer.

Furthermore, lateral patterning of the EB and magnetic domain state by electrical means is demonstrated in a continuous EB film. This is an important advantage over the solid-state ionic approaches for electrical EB control, which thus far require patterned elements. [87,88] The voltage-programming of magnetic domains in extended magnetic films provides the possibility of electrically controlled magnetophoretic devices that rely on laterally patterned artificial EB-induced domain structures.^[7] In contrast to conventional modification of EB via local temperature application or ion bombardment, for example, the presented electrical approach presents an energy-efficient method for reversible EB fine-tuning, which can be easily combined with standard lithography for micromagnetic domain engineering.

The versatile reduction/oxidation-based voltage-control of an EB system provides a new approach for the design of EB systems and development of future electrically controlled spintronic and magnetophoretic devices.

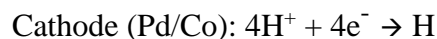
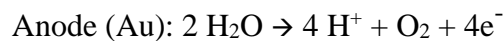
9 Voltage control of magnetic thin films with perpendicular unidirectional anisotropy

*The results of chapter 9 are published in [3] within the framework of this thesis. The respective paragraphs – with minor adjustments – are indicated in grey font. Reprinted with permission from [3]
(Copyright 2021, <https://doi.org/10.1103/PhysRevMaterials.5.L061401>) by the American Physical Society.*

In chapters 6, 7 and 8, we focused on magnetic thin films with the magnetization in the film plane. In particular, the thin films presented in chapter 8 showed a unidirectional anisotropy in the film plane. In chapter 9, we will focus on the voltage control of magnetic thin films with perpendicular unidirectional magnetic anisotropy. In addition, we will replace the liquid electrolyte (LiOH) with a solid-state electrolyte (GdO_x).

9.1 Co thin films with perpendicular unidirectional anisotropy

To achieve the perpendicular exchange bias thin film system, we use an ultrathin ferromagnetic Co layer (0.9 nm) to achieve perpendicular magnetic anisotropy and a NiO layer (30 nm) as the antiferromagnet. The complete layer stack is depicted in **Figure 9.1** (a). All layers were deposited by sputtering. The TEM cross-section image shows the individual layers in as-deposited state (Figure 9.1 (b)). We deposited an ultrathin Pd interlayer (0.2 nm) on top of the NiO layer, prior to Co deposition. However, the single layers of the trilayer Pd(5nm)/Co(0.9nm)/Pd(0.2nm) cannot be distinguished. Without this Pd interlayer, i.e., when the Co layer is in direct contact with the NiO layer, neither an out-of-plane (Figure 9.1 (c) grey line), nor an in-plane magnetization curve (not shown in Figure 9.1 (c)) is detected by MOKE magnetometry. Thus, the direct deposition of Co on the NiO layer most probably lead to the formation of non-ferromagnetic CoO_x. The introduction of the ultrathin Pd interlayer avoids this oxidation process and leads to the stabilization of the ferromagnetic Co phase. As a result, this layer stack exhibits the desired magnetization curve displaying perpendicular EB (Figure 9.1 (c) black curve). Upon gating, we expect the following electrochemical reactions at V_g = +3 V in the Au/GdO_x/Pd/Co/Pd electrochemical cell: [20], (see also Figure 3.5 and Figure 3.6)



9.2 Voltage control of EB in Co/Pd/NiO thin films

To achieve voltage tuning of the perpendicular exchange bias field (H_{EB}), we investigate the influence of hydrogen gating on the magnetic properties of the EB layer stack. **Figure 9.2** illustrates the influence of an applied voltage on the perpendicular magnetization curves. Figure 9.2 (a) shows the curve of the pristine state after hydration

of the GdO_x layer. The gate voltage is applied between the Au layer and the top Pd layer (see Figure 9.1(a) and Figure 3.5 Figure 3.6). When a gate voltage (V_G) of $V_G = +3$ V is applied, a continuous change in the magnetization curves occurs which reflects a decrease in the perpendicular anisotropy [20] (Figure 9.2 (b-d)). After 138 s at +3 V (Figure 9.2 (d)), the closed magnetization curve with vanishing $M_R/M_{79.6\text{kAm}^{-1}}$ ratio and H_C reveals a fully in-plane anisotropy state. When the applied voltage is set back to 0 V, the hysteresis loop recovers to an out-of-plane state (Figure 9.2 (e)-(g)). With this transition from the out-of-plane to the in-plane state and vice versa, the perpendicular EB vanishes and recovers. The absolute value of the EB field of the recovered state ($|H_{\text{EB}}| = 6.6 \text{ kAm}^{-1}$ in Figure 9.2 (g)) compared to the pristine state ($|H_{\text{EB}}| = 12.0 \text{ kAm}^{-1}$ in Figure 9.2 (a)) is decreased. In contrast, the H_C of the recovered loop is larger than that of the pristine loop.

In order to study the reversibility on the observed electrochemical control of EB, 11 switching cycles with repeated application of $V_G = +3$ V and $V_G = 0$ V were measured. The out-of-plane $M_R/M_{79.6\text{kAm}^{-1}}$ ratio, H_C and (negative) exchange bias field for this voltage sequence are shown in Figure 9.3 (a-c), where the grey shaded areas mark the times with $V_G = +3$ V and the white areas mark the times with $V_G = 0$ V. In Figure 9.3 (c), the (negative) exchange bias field values are only plotted for the states at 0 V, for which an appreciable perpendicular EB occurs. To exclude that the effects are related to the consecutive cycling of the magnetic field, the hysteresis loop of the same sample was continuously measured for about 250 s before the voltage was applied. In this case, no change in magnetic properties and EB occurred (grey data points in Figure 9.3 (c)). In contrast, the voltage-induced change between out-of-plane state (high $M_R/M_{79.6\text{kAm}^{-1}}$ and H_C) and in-plane state (low $M_R/M_{79.6\text{kAm}^{-1}}$ and H_C) is observed for all subsequent switching cycles. After the first cycle, in accordance with the results in Figure 9.2, a decreased (negative) exchange bias field and increased H_C is observed in the recovered state (0 V), in comparison to the pristine state. In the subsequent cycles, a further moderate decrease in $|H_{\text{EB}}|$ and a further marginal increase in H_C are measured for the recovered states (0 V). Further, the time which is necessary to switch $|H_{\text{EB}}|$ and/or H_C off decreases after the first cycle.

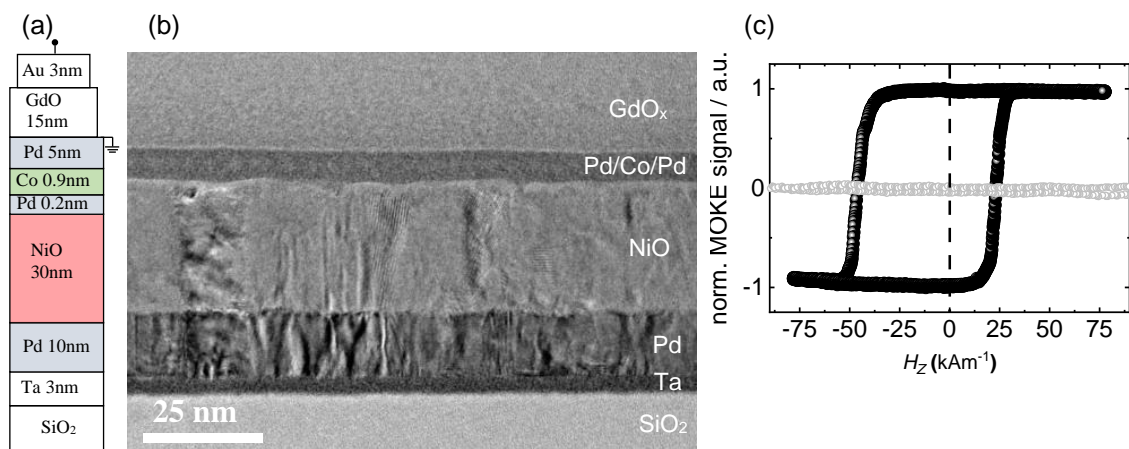


Figure 9.1: Pd/Co/(Pd)/NiO thin film system – crosssection and magnetization curve

(a) Schematic illustration of the sputter deposited layer architecture with nominal layer thicknesses, including the electrode connections. (b) Cross-section bright-field TEM image of the layer stack depicted in (a). (c) Magnetization curves for layer stacks with (black symbols) and without (grey symbols) a 0.2 nm Pd interlayer between the NiO and Co layers as measured by polar laser MOKE magnetometry.

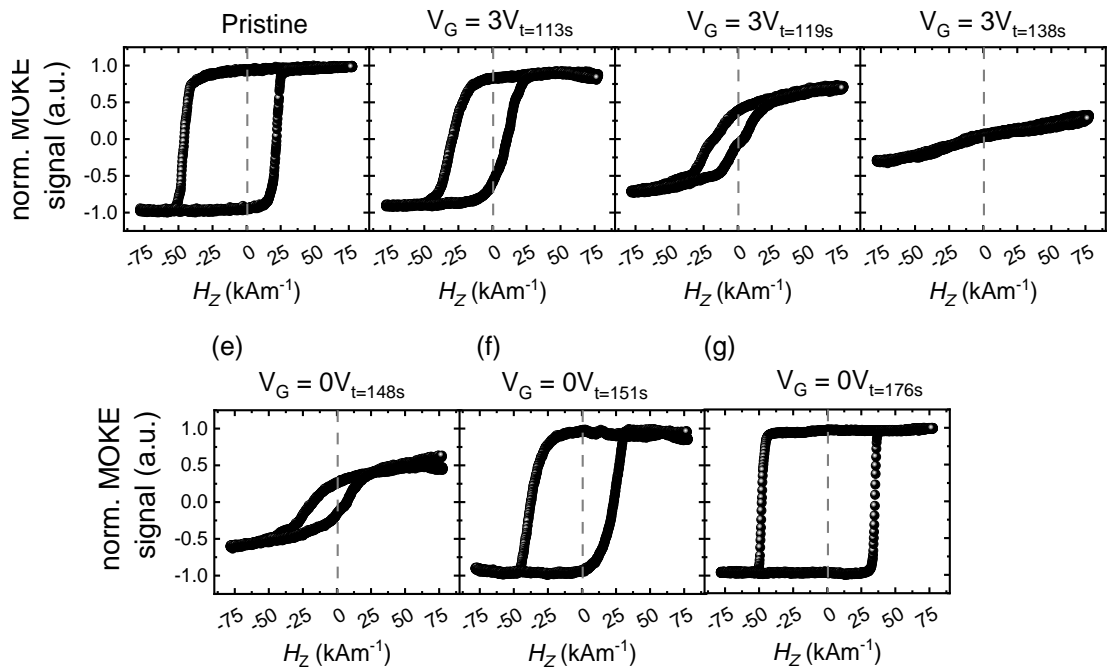


Figure 9.2: Electrochemical controlled switching of EB

Magnetization curves at (a) pristine state, (b)-(d) at $V_G = +3$ V, showing the decreasing perpendicular anisotropy over time, and (e)-(g) at $V_G = 0$ V showing the recovery of perpendicular anisotropy and exchange bias over time.

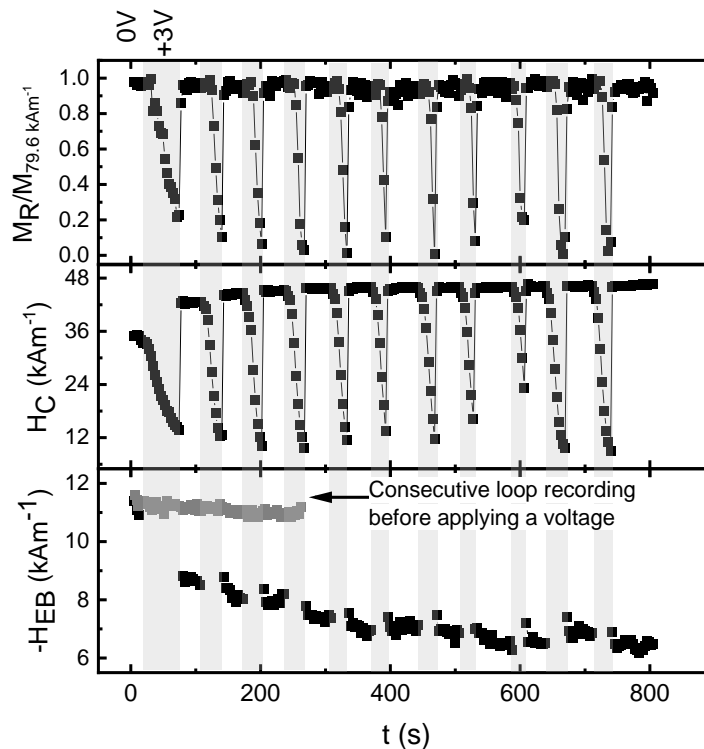


Figure 9.3: Voltage induced changes of magnetic properties in EB system.

Out-of-plane M_R/M_S ratio (3a), H_C (3b) and EB (3c) versus time as V_G is repeatedly set between +3 V (grey shaded area) and 0 V.

As a possibility to further control the EB in the recovered states during several switching cycles, we investigate the influence of a superposed (out-of-plane) magnetic field during voltage gating.

Figure 9.4 shows the influence of a superimposed magnetic field of $\pm 159.2 \text{ kAm}^{-1}$ during gating at $V_G = +3 \text{ V}$ on the exchange bias field measured afterwards for the recovered state (0 V) for different measurement steps (n). The black open data point in **Figure 9.4** equals $|H_{EB}|$ of the last measurement step in **Figure 9.3 (c)**. Then, a positive magnetic field of $+159.2 \text{ kAm}^{-1}$ and simultaneously $+3 \text{ V}$ were applied for 10 s . After setting the voltage back to 0 V , the recorded hysteresis loop exhibits an increase in $|H_{EB}|$ by about 10% . The measurements sequence was repeated, but with the superposition of -159.2 kAm^{-1} . In this case, after voltage-switch off, a decrease of $|H_{EB}|$ by about 15% is obtained with respect to the starting state (black data point on the left in **Figure 9.4**). This measurement procedure was repeated three times and resulted in a similar increase/decrease of the exchange bias field for positive/negative applied magnetic fields. After this routine the sample was saturated in $+159.2 \text{ kAm}^{-1}$, rested in remanent state and measured again after 5 min . This results in a positive shift of $|H_{EB}|$. Almost the same $|H_{EB}|$ is measured in this sample after 24 days without further voltage- or magnetic field application, showing good long-term stability. In order to understand the electrochemical control of EB, the cross-section of the EB layer stack was characterized by high resolution transmission electron microscopy before and after the voltage-gating procedure (**Figure 9.5**). In the pristine state (**Figure 9.5 (a)**), an amorphous Pd/Co/Pd layer is observed on top of the crystalline NiO layer. In contrast, after the voltage-gating (after cycle $n = 8$ in **Figure 9.4**), a crystalline structure is observed for the Pd/Co/Pd layer which shows epitaxial alignment to the NiO layer (**Figure 9.5 (b)**). In addition, crystallized areas are also visible within the $\text{Gd}(\text{OH})_3$ after gating.

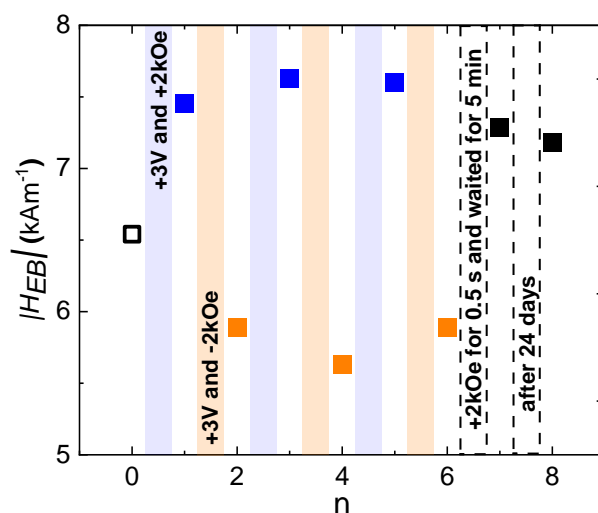


Figure 9.4: Exchange bias switching by voltage and magnetic field.

Influence of a superimposed magnetic field during gating steps (n) on the exchange bias field of the recovered state afterwards. In addition, the long term stability of the exchange bias field after 5 min and 24 days is included.

Discussion

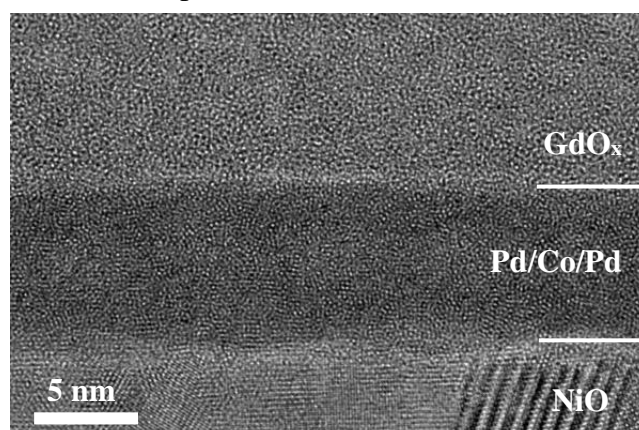
We achieve voltage-control of perpendicular EB by applying hydrogen-based electrochemistry to a tailored magnetic layer stack. For this, we introduced an antiferromagnetic NiO underlayer in a Gd(OH)₃/Pd/Co heterostructure, in which the Co layer is known to be susceptible to hydrogen-based electrochemical control. [20] An ultrathin Pd interlayer is introduced between the Co and NiO layer to avoid loss of magnetic properties due to Co oxidation. In such Gd(OH)₃/Pd/Co/Pd/NiO architectures perpendicular EB is achieved. The Pd interlayer thus does not impede the interfacial coupling between the antiferromagnetic NiO and the ferromagnetic layer. The reason could be the formation of a Co-Pd alloy at the interface. This is consistent with the HR-TEM images of the pristine state (Figure 9.5 (a)), in which the individual Co and Pd layers cannot be distinguished.

Upon voltage gating, a decrease of H_C and M_R/M_S ratio occurs and the perpendicular EB vanishes. This behavior is reversible and can be directly explained by the decrease of perpendicular anisotropy of the Co layer due to voltage induced H⁺ migration through the Gd(OH)₃ and subsequent H adsorption at the Co layer. [20] The first-time switching process is distinct from the subsequent cycles. It shows a slower kinetics until full in-plane switching is achieved and the changes in H_C and $|H_{EB}|$ between pristine and recovered (0 V) state after the first cycle are larger than during subsequent cycles. After the first gating step (Figure 9.3, 15-80 s), a decrease in $|H_{EB}|$ is observed, while at the same time H_C significantly increases (+22 %). This inverse scaling of H_C and $|H_{EB}|$ is unusual. In common EB systems, H_C and $|H_{EB}|$ scale with each other, because the EB gives an intrinsic contribution to H_C . [137] Thus, in the present case, the H_C increase cannot be caused by the change of the EB, but must have a separate origin.

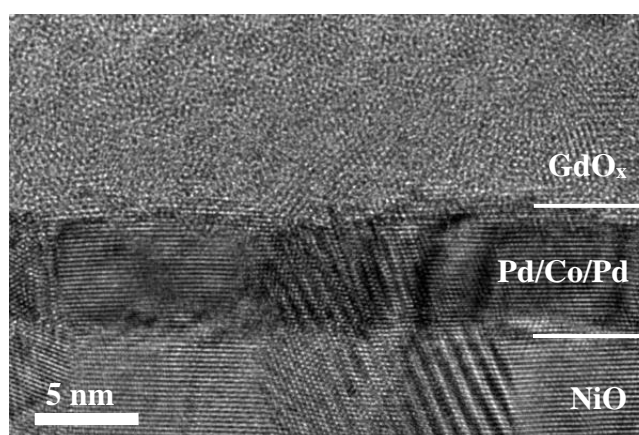
Our results indicate that the distinct feature of the first cycle, namely the slow kinetics and the increase of H_C , are related to a microstructural activation/transformation process. Upon voltage-gating, hydration of the Pd layer is known to occur, which will lead to expansion and straining of the initial Pd layer. This could induce magnetoelastic effects in the Co layer and thereby impact H_C . However, in the initial state, the Pd/Co/Pd structure is amorphous (Figure 9.5 (a)) and the magnetoelastic interactions are expected to be small due to the microstructural randomness. [155–158]

In contrast, we propose that the observed amorphous to crystalline transformation of the Pd/Co/Pd layer region (Figure 9.5) provides a direct explanation for the increase in H_C . We propose that crystallization is triggered when hydrogen enters the structure for the first time. Such hydrogen-induced crystallization of amorphous metals has indeed been reported previously. [159,160] Amorphous layers in general show softer magnetic properties (i.e. lower H_C) compared to their crystalline counterparts. [27,29] This can be easily understood by the introduction of grain boundaries in crystalline layers which add pinning sites to the system and thus to an increased H_C . Further, the increased H_C after the first gating step is assigned to the newly existing grain boundaries. We propose that the solid-state crystallization process occurs during the first-time hydrogenation process.

a) Pristine sample (BFTEM)



b) Gated sample (BFTEM)



c) Gated sample (BFTEM)

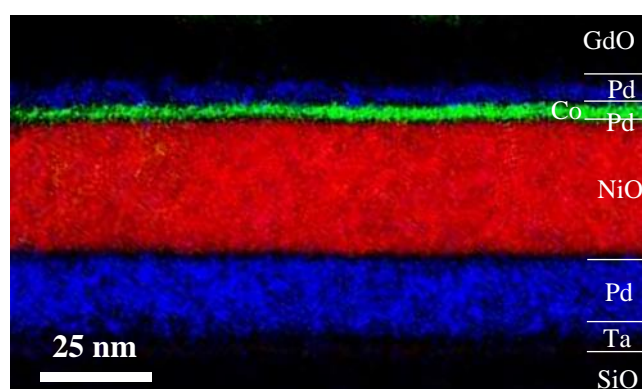


Figure 9.5: Cross-sectional TEM on SiO/Ta/Pd/NiO/Pd/Co/Pd/GdO_x system.

(a) Pristine sample exhibiting amorphous Pd/Co/Pd layer and (b) sample after voltage-gating, exhibiting crystalline Pd/Co/Pd layer. The cross-sectional elemental map obtained by Energy-filtered TEM in (c) shows a larger area of the cross-section, of the same lamella as in (b), of the film after gating with colored coded elements (Pd (blue), Ni(red) and Co(green)). The Co layer is clearly visible.

This is consistent with the prolonged switching time required during the first step. The marginal change in H_C during the subsequent cycles (see Figure 9.3 (b)) indicates that crystallization is completed after the first cycle. The partial solid-state crystallization of the $\text{Gd}(\text{OH})_3$ might also lead to the prolonged switching time during the first measurement step.

As a trend, the $|H_{EB}|$ of the recovered states (0 V) decreases with increasing cycle numbers, the rate of change slows down and almost settles after cycle number 8 (ca. 500s in Figure 9.3 (c)). We discuss this behavior in the following with regard to two possible mechanisms, a voltage-induced training effect and a thermal after-effect.

The training effect describes the decrease in $|H_{EB}|$ and H_C when cycled in a magnetic field. [34,161] The training effect is divided into an athermal and a thermal part. [162,163] The athermal training only occurs after the first magnetic field cycle and triggers, assuming a hysteresis with $-H_{EB}$, a significant shift of the descending branch (H_L in Figure 2.4 (b)) in such a way that $|H_{EB}|$ and H_C are decreasing. This effect is temperature independent. In cubic antiferromagnets (e.g. NiO), the athermal training effect is assigned to a spin flop relaxation leading to a uniaxial spin arrangement in the antiferromagnet after the first magnetic field cycle of the ferromagnet. [164] On the other hand, the thermal training effect sets in after the first magnetic field cycle and is characterized by smaller changes in $|H_{EB}|$ and H_C for subsequent loops. The thermal training effect arises from thermally instable antiferromagnetic spin ordering within in the antiferromagnetic grains. [162]

The thermal after effect is similar to the thermal training effect but, here the $|H_{EB}|$ changes over time in remanent magnetic field. At high enough temperature, the magnetic ordering in the antiferromagnetic grains overcome a certain energy barrier which allows for switching their magnetic orientation. [165–168] This reorientation occurs independently in the AFM grains, as they do not exchange couple among each other, following a Néel-Arrhenius law of time relaxation. [169]

In the present case, a pronounced training effect is absent when cycling the system through consecutive hysteresis loops without voltage application (compare Figure 9.3 (c) grey data points). Thus, the observed effect must arise from a mechanism during the voltage-gating process. A voltage-induced training effect on EB was previously observed in $\text{CoPt}/\text{Cr}_2\text{O}_3$ system and related to voltage-triggered spin reorientation in the magnetoelectric antiferromagnet Cr_2O_3 . [170,171] The presented electrochemical case differs from this in a conceptual way, because the NiO antiferromagnetic layer is not magnetoelectric, and thus the voltage does not directly impact the antiferromagnetic layer. Instead, we propose that the voltage-triggered spin reorientation in the ferromagnetic layer adjacent to the antiferromagnetic domains can trigger relaxation processes in the surface antiferromagnet spin states. Voltage-induced H adsorption affects the perpendicular spin ordering of the ferromagnet, which couples to the AFM. The perpendicular spin ordering of the ferromagnet vanishes upon H adsorption and re-establishes at voltage-switch-off. During these reorientation processes in the ferromagnet, the adjacent unstable AFM spins might experience a reorientation process and metastable spins (e.g. rotatable spins) will fall into a more stable state which reduces $|H_{EB}|$. In order

to describe the potential training effect in the present case, we averaged the EB values of each voltage switching step and plotted them over the measurement steps (Figure 9.6 (a)), assuming time independency of the applied gate voltage for each step [163]. The fit for a model of exchange bias training effects (solid blue line in Figure 9.6 (a)) [36] shows good agreement (see Appendix on page 104). This indicates that the results could be explained in the frame of a training effect model.

Besides a voltage-induced training effect, a voltage-induced thermal after-effect may play a role. In this case, thermal energy introduced during voltage application may lead to thermal activation and associated spin relaxation in the antiferromagnet. To describe this effect, the averaged $|H_{EB}|$ data is plotted against the measurement time in logarithmic scale (Figure 9.6 (b)). The linear behavior in this case fits to a voltage-induced thermal after effect [165,167,172–174]. We conclude that training effects and thermal after effect activation could explain the evolution of the exchange bias during repeated voltage-switching, when described within a very simplified picture of stable and unstable spin elements within the antiferromagnet. [36,175,176]

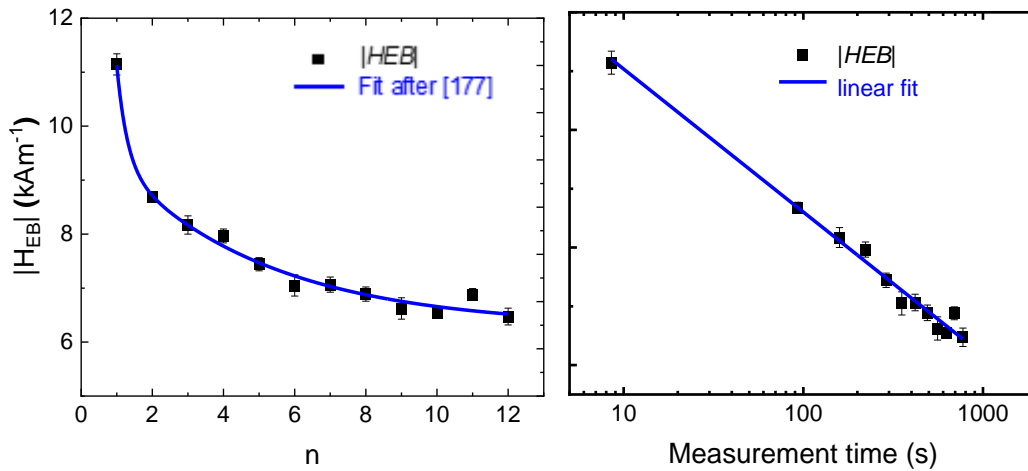


Figure 9.6: Model for change in exchange bias field

(a) Decrease of $|H_{EB}|$ with measurement steps and a fit to the data after [177]. (b) Decrease of $|H_{EB}|$ over the logarithmic measurement time and a fit to the data in the frame for the thermal after effect, $R^2=0.98$.

9.3 Interim conclusion

In conclusion, voltage-gating, utilizing hydrogen pumping, has been demonstrated for a perpendicular exchange bias system. During voltage-gating, the perpendicular magnetic anisotropy and associated perpendicular M_R , H_C and $|H_{EB}|$ of the ferromagnetic layer vanish. The process can be reversed by voltage-switch off, and is repeatable for several cycles. For the first cycle, the voltage-gating process is slower and a distinct increase in H_C yet decrease in EB is observed for the recovered state in comparison to the initial one. These features are explained by a hydrogen-induced crystallization process of the initially amorphous ferromagnetic layer. The absolute exchange bias field continuously decreases with the voltage cycling steps, indicating a voltage induced exchange bias training effect and/or thermal after effect. A combined voltage- and magnetic field routine allowed to overcome this effect and control the value of H_{EB} . The mechanism for setting the exchange bias was explained in a simple picture of unstable spin elements within the antiferromagnet which are changed towards more stable states due to thermal relaxation processes upon voltage gating the ferromagnet. The possibility to tune the exchange bias by superposing an electric as well as a magnetic field could replace post annealing treatments and adds functionality to the device. The herein presented procedure is much faster and can also be combined with on/off switching of perpendicular anisotropy. The additional electric field might also offer a reduced energy consumption compared to a pure external magnetic field setting of the exchange bias [178]. The herein presented effects locally affect the exchange bias in a reversible manner, which goes beyond irreversible modification by laser or ion radiation. [80,179] This work may show a path towards electrochemical control of exchange bias as well as antiferromagnetic devices via a voltage in general [180].

9.4 Voltage control of ferrimagnetic GdCo/Pd/NiO thin film

Ferrimagnets became popular in recent years with respect to their e.g. fast dynamics of domain walls [181,182] and the appearance of skyrmions at room temperature. [183] A dominant sublattice switching in $GdO_x/Pd(10nm)/Gd_{45.7}Co_{54.3}(10nm)/Pt(6nm)/Ta(4nm)/SiO_2$ films upon hydrogen loading has been recently found. [184] The mechanism is based on hydrogen insertion into the GdCo which leads to a shift in the compensation temperature, the temperature at which the two sublattice moments cancel each other, of the GdCo film. The shift of the compensation temperature changes the initial dominant sublattice from Gd dominant to Co dominant. Upon removal of hydrogen, the process is reversed. Exploiting the effect of a dominant sublattice switching in an exchange bias film structure, might enable an inversion of $|H_{EB}|$. The author of the presented thesis fabricated a Gd-dominant GdCo thin film on top of an antiferromagnet. The optimized stack is shown in **Figure 9.7** (a) In order to obtain a Gd-rich GdCo structure exhibiting exchange bias, every attempt failed which brought the GdCo layer in

direct contact with the NiO layer. This is probably due to the higher affinity of oxygen to Gd compared to Ni. Thus, the Gd might be oxidized when GdCo is in direct contact with the NiO. Similar to the NiO/Pd/Co/Pd films (see Figure 9.1), by placing a thin Pd interlayer (nominal 0.1-0.2 nm in thickness) between the NiO and the GdCo layer, it was possible to obtain a Gd-rich GdCo structure GdO_x(15nm)/ Pd(5nm)/ GdCo (10nm)/ Pd(0.2nm)/ NiO(30nm)/ Pd(5nm)/ Ta(3nm)/ SiO₂. The magnetization curve of a Gd dominant GdCo thin film, measured via a red laser-MOKE, is inverted, see the orange magnetization curve in Figure 9.7 (b). This is due to the sensitivity of the red light to the transition metal (Co). [184,185] Upon gating such a structure, we were able to demonstrate the principle dominant sublattice switching effect, as explained above, of an exchange biased Gd-dominant NiO/Pd/GdCo film. Figure 9.2 (b) shows the pristine magnetization curve with a Gd-dominant sublattice (orange) and the magnetization curve with a Co-dominant sublattice (grey).

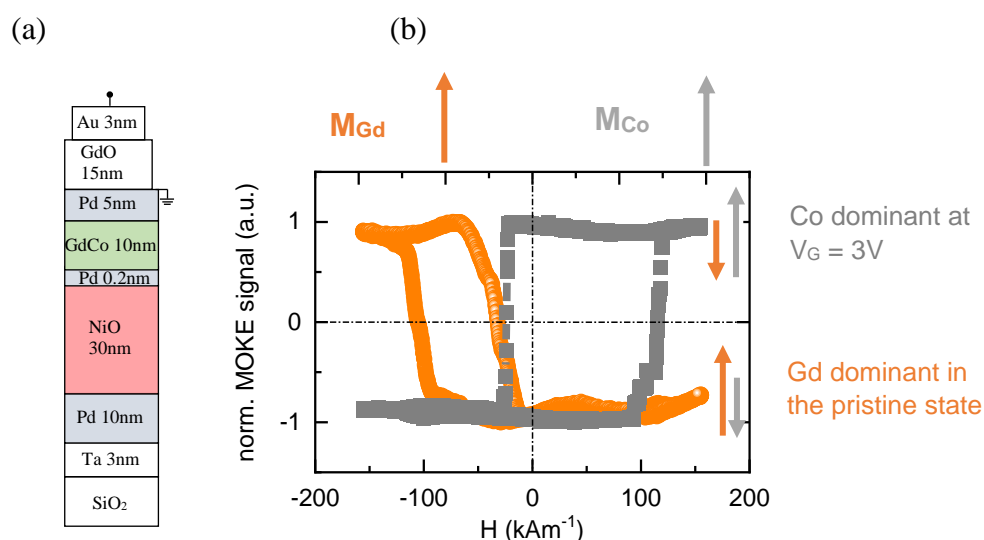


Figure 9.7: GdCo exchange bias stack and dominant sublattice switching

(a) Layer stack of a Gd-rich GdCo film in contact with an antiferromagnet. (b) Sublattice switching of a Gd-rich GdCo exchange biased film. The orange arrow indicates the magnetic moments of the Gd and the grey arrow indicates the magnetic moment of the Co.

With chapter 8 and 9, we fulfilled the second objective of the presented thesis, namely: To demonstrate novel concepts on the tuning of exchange bias at room temperature based on electrochemical reactions. These findings provide new insights into the mechanisms of voltage controlled magnetic properties by electrochemical reactions.

10 Evaluation with regard to perspective applications

The immense research on voltage control of magnetism is triggered almost exclusively by the desire to reduce joule heating effects in the information and technology sector. In the following section, the potentials and challenges of the electrochemical control of magnetic materials for the application in different technologies is evaluated with a focus on the systems studied in the present work. Since the technology readiness of this emerging topic is still at the fundamental research levels 1-2 (1-basic principles observed, 2-technology concept formulated [186]). The discussion also involves more fundamental aspects regarding the material properties. It does not include issues related to industrial device fabrication requirements, such as integrability into fabrication processes (temperature treatments etc.).

Application potential – data technology

Conventional magnetic memories involve high current densities either due to spin-polarized electric currents or due to microcoils to generate magnetic fields. In these systems, energy dissipation due to Joule heating becomes increasingly problematic, especially in view of the rise of Big Data and the Internet of things. Electrochemical control of magnetism would present an energy-efficient alternative approach, as electrical voltage is the control parameter and different magnetic states can be set in a non-volatile manner. Very low current densities (in the present work $\approx 0.25 \text{ mA/cm}^2$ for the FeO_x to Fe transformation) only occur during the setting.

The limiting factors for applicability in data technology might be in the first place, the reversibility and the switching speed. In order to compete with state of the art technology, a stability over $>10^{15}$ cycles and switching speeds between 10 ms (hard drive HD) and 10 ns (spin transfer torque random access memory STTRAM) are necessary. [187] So far, the most promising (academic) magnetic devices which rely on electrochemical switching can be cycled for 2000 times with a speed of 100 ms [20] This is achieved by the use of hydrogen in the all-solid state Au/GdO_x/Co/Pt architecture. [20] In addition, first attempts for decreasing the switching speed can be achieved by further engineering the gating oxide, such as doped YSZ in a Au/YSZ/Co/Pt structure. [188] The switching speed decreased to 1 ms but the reversibility was only shown for 1000 cycles. [188] Nevertheless, these systems approach are promising to meet the required switching speeds and reversibility, while at the same time they promise a much higher energy efficiency than HD and STTRAM. [20]

The structures studied in chapter 9 (Au/GdO_x/Pd/Co or GdCo/Pd/NiO/Pd/Ta/SiO₂) rely on the same gating structure and hydrogen-based mechanism. Thus, even though the investigation of the switching speed was not the focus here, a similar range of switching speed and reversibility are expected.

Oxygen-ion based gating mechanisms for magnetic materials, like the ones presented in chapter 7 and 8 so far show switching speeds in the range of seconds and reversibility

up to 10 cycles (see Figure 7.2, Figure 7.6). Nevertheless, studies on memristive devices, which rely on oxygen ion transport, indicate switching times up to sub-ns, if the ion transport pathways are further engineered [131–133]. In addition reversible cycles up to 10^8 are reported. [189] In the light of future achievements with regard to the switching speed and reversibility, the electrochemical induced changes in the magnetic microstructure (see Figure 7.4, Figure 7.5, Figure 8.8) as shown for the FeO_x/Fe based thin films in chapter 7 and 8, might offer the possibility to reduce the power consumption in electrical-current based magnetic domain-wall logic devices [130,183,190,191]. We calculated a switching energy of 121 mJ for switching the magnetization in FeO_x/Fe thin films. Assuming a linear relation between the switching energy and the device diameter, we would already achieve a switching energy of 5 fJ in FeO_x/Fe thin films which is comparable to the lowest reported switching energies, namely 6 fJ for magnetic tunnel junctions (see also discussion in subchapter 7.6).

The stack architecture and concepts for electrochemical voltage control of magnetic devices are in some aspects comparable to those of neuromorphic computing devices [192]. Ion-based concepts to control magnetism might also be interesting for bioinspired ionic systems for neuromorphic computing, in which multiple ions in artificial (neuromorphic) systems are utilized to mimic biological signal transport processes via the application of a voltage (e.g. synapses). [193] Liquid electrolytes might be a good candidate for using multiple ions (and thus brain inspired computing), while this might be more challenging for solid state electrolytes.

In summary, the application potential arises mainly due to the energy efficiency. However, before industrial application in data storage and computing comes within reach, an increase of switching speed and reversibility must be accomplished.

Application potential – actuation technology

For magnetic actuation devices the use of electromagnetic coils leads to an associated energy loss. This becomes problematic particularly when downscaling to the microscale, as here, high current densities are required to achieve sufficient magnetic field strength. [135] Here, electrochemically induced magnetic changes could present an energy-efficient alternative, especially as the demand for switching speeds is less crucial than for data storage devices.

For instance, in some magnetophoretic devices magnetic particles are immersed in a liquid above a 10-15 nm magnetic thin film with in-plane magnetization. [16,17] In these cases, an external magnetic field, so far realized by electromagnets, is used to manipulate the magnetic domain patterns and thereby enable the transport of the magnetic particles in solution by magnetic actuation. The magnetic control occurs on a time scale of seconds, similar to the speed of the magnetization switching observed for the FeO_x to Fe transformation in chapter 7 (see Figure 7.6). Electrochemically induced magnetic changes could thus potentially be used in such devices to switch on and off the magnetic field or/and assist the magnetic field control of the magnetic film.

Application potential – material design and patterning

So far, ion bombardement of magnetic thin films is a common approach and partly applied in start-ups, like *Spin-ION Technologies* [194], to irreversibly change the magnetic properties and magnetic domain structure of materials. The electrochemical patterning of the magnetic microstructure, as demonstrated in chapter 8 (see Figure 8.8), shows that electrochemical controlled approaches may present a new concept here. In comparison to common patterning concepts such as ion-beam induced patterning [34,81,194], electrochemical patterning would offer the advantages of operation in ambient conditions without the need of vacuum equipment. Further, in the case of reversible modification, a reprogramming of domain patterns and material properties may be within reach.

Further application potential can be expected in the future by investigating a possible electrochemical tuning of the frequency performance of magnetic films for, e.g. transformers [195]. In such transformers, also films with uniaxial in-plane anisotropy, as studied in the present work (chapter 6) are applied. For instance, the frequency tuning in [195] is achieved by sputtering films under different angles to achieve different values for the in-plane uniaxial anisotropy. Thus, the frequency performance of a film, deposited under an given angle, is fixed. The electrochemical post-fabrication control of the in-plane uniaxial magnetic anisotropy might also offer the possibility to tune the frequency of the same film.

11 Summary

In this thesis, we studied the voltage control of magnetic thin films with uniaxial and unidirectional anisotropy by electrochemical reactions. We studied solid/liquid and all-solid systems. For the solid/liquid system, we developed an electrochemical cell which is compatible with a Kerr microscope (chapter 5).

Voltage-induced de-blocking by electrochemical reactions in FeO_x/Fe films results in a reversible collapse of coercivity and remanence. The analysis of the inverse changes of coercivity and anisotropy, and the magnetic domains reveals modulations of the Néel-wall-interactions, and of the microstructural domain-wall pinning sites as the origin. The estimated switching energy for 180° magnetization reversal is promising for ultralow power devices (chapter 6 and 7). [1]

Non-volatile, continuous and reversible voltage-tuning of exchange bias (EB) is achieved via electrolytic gating at low voltage (1 V) and at room temperature. The mechanism is based on a buried redox reaction and associated thickness change in the ferromagnetic layer. A lateral voltage-induced patterning of EB and magnetic domain state is demonstrated as unprecedented route for the future design and electrical control of EB systems. [2]

Films with perpendicular exchange bias in a $\text{GdO}_x/\text{Pd}/\text{Co}$ -or- $\text{GdCo}/\text{Pd}/\text{NiO}$ based structure are for the first time successfully fabricated. The subsequent voltage-induced changes of the exchange bias properties of the $\text{Pd}/\text{Co}/\text{Pd}$ films are explained by a training effect. A sign change of the exchange bias in the $\text{Pd}/\text{GdCo}/\text{Pd}$ film upon voltage-gating is demonstrated for the first time in chapter 9.

The aforementioned results are reported for the first time within the framework of this thesis. These findings provide new insights into the mechanisms of voltage controlled magnetic properties by electrochemical reactions.

In situ Kerr cell (Chapter 5)

In Chapter 5, we develop an electrochemical cell which is compatible with a Kerr microscope. This home built electrochemical cell demonstrated their electrochemical functionality and is used for experiments on liquid/solid systems, such as $\text{LiOH}/\text{FeO}_x/\text{Fe}$ in chapter 7 and $\text{LiOH}/\text{FeO}_x/\text{Fe}/\text{IrMn}$ in chapter 8.

Blocked state in FeO_x/Fe thin films (Chapter 6)

The sputter deposited polycrystalline FeO_x/Fe thin films show an in-plane uniaxial anisotropy, owed to the oblique deposition technique. Using a Kerr microscope, we

performed anhysteretic measurements to quantitatively access the magnetic anisotropy. Further, angle-dependent magnetization curves were measured. They revealed that the magnetization curve along the hard axis exhibits an increased coercivity and remanence, and thus deviates from an “ideal” hard axis magnetization reversal by uniform rotation of magnetization. This behavior is ascribed to a blocked state arising from interacting Néel walls. The use of anhysteretic measurements for assessing the anisotropy energy in such films, as performed in this work, has not been reported yet. The method of measuring angle dependent in-plane magnetization curves with a Kerr microscope and a rotating field, instead of a rotating sample, has also not been reported yet.

Voltage control of FeO_x/Fe thin films with uniaxial anisotropy (Chapter 7)

Chapter 7 builds the core chapter of the presented thesis and answers the first objective of the presented thesis. In Chapter 7, we demonstrate voltage controlled magnetic de-blocking by electrochemical reactions in the FeO_x/Fe thin films with in-plane uniaxial magnetic anisotropy. A visual summary is shown in **Figure 11.1**. We conclude by restating the interim conclusion from subchapter 7.7. We demonstrate a fully reversible low-voltage-induced collapse of coercivity and remanence in FeO_x/Fe thin films at room temperature, accompanied by large anisotropy and domain structure changes. The magnetic changes are induced by the reversible reduction and re-oxidation of the FeO_x layer. Detailed analysis of the impact of this phase change on the magnetic hysteresis and domains indicates a voltage controlled de-blocking mechanism, connected to changes in the microstructure and the structure of magnetic domains.

In the initial (oxidized) state, a blocked state that exhibits a large hysteresis for the hard axis direction is stabilized by Néel wall interactions. Upon reduction of the FeO_x, the increase in anisotropy and Fe-layer thickness can lead to a larger domain wall energy, and thereby cause the observed increase in domain size. As a result of the coarsening of the magnetic microstructure, the domain-wall interactions are weakened, and the magnetically blocked state is suppressed. This is followed directly by the voltage-induced switching from a large hysteresis along the hard axis to ‘close to ideal’ hard-axis behavior. The decreased pinning strength of the grain boundaries upon FeO_x reduction can cause the collapse of the coercivity along all other directions.

The apparent contradiction that a decreased coercivity is obtained at increased anisotropy can be resolved by accounting for the role of the microstructure and the magnetic domains. Coercivity and anisotropy thus do not need to necessarily scale with each other, an important consideration for voltage control of materials involving changes in phase and microstructure. This consideration opens a route beyond the state-of-the-art of electrochemical control of thin-films, in which extrinsic properties such as coercivity are usually changed by controlling the intrinsic perpendicular magnetic anisotropy. The voltage-induced modification of local defects presents a paradigm change in ionic control of magnetism, which so far commonly affect the interface or the bulk of the material as a whole. For the local control of defects only a small portion of the material needs to be affected. This promises a higher energy efficiency and faster speed than conventional magneto-electric approaches. The voltage induced mechanism presented in this paper

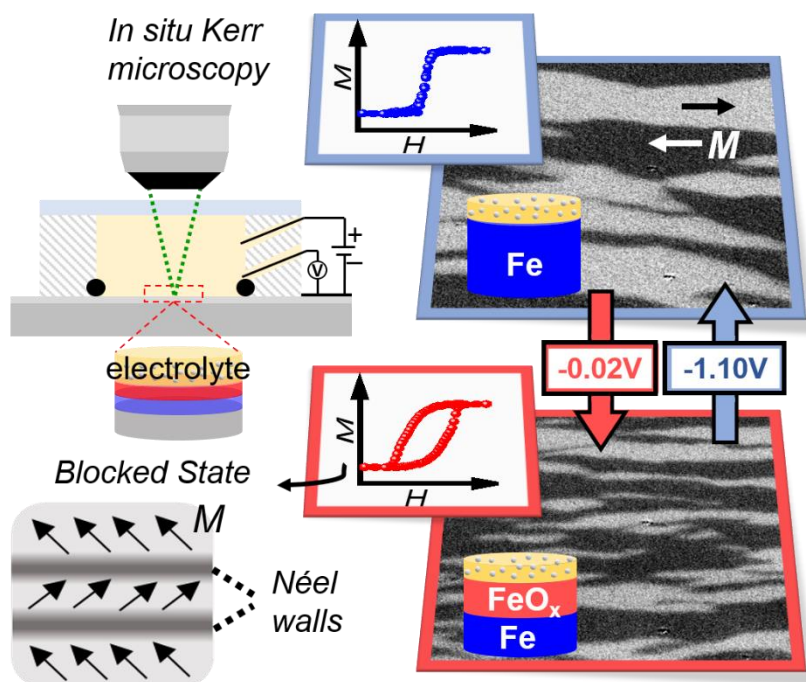


Figure 11.1: Visual summary of the findings in chapter 7

fulfills the important requirements of room temperature and ultralow power operation of future magnetic devices, especially in the fields of magnetic memory, domain wall logic, neuromorphic computing, and magnetic actuation devices. The mechanism of voltage-controlled defects may be transferrable to many other defect-controlled materials, such as type II superconductors or materials with specific mechanical properties.

With chapter 5, 6 and 7, we fulfilled the first objective of the presented thesis, namely: To directly observe, for the first time, magnetic microstructure changes of magnetic thin films with in-plane magnetization in a liquid electrolyte during simultaneous voltage-triggered electrochemical reactions.

Voltage control of $\text{FeO}_x/\text{Fe}/\text{IrMn}$ thin films with in-plane unidirectional anisotropy (Chapter 8)

In chapter 8, we exploit the FeO_x to Fe transformation in an exchange biased thin film. A visual summary is shown in **Figure 11.2**. We achieve non-volatile, continuous and reversible changes of the exchange bias at a low voltage and at room temperature. The proposed mechanism is based on a thickness change in the ferromagnetic layer. The thickness change was confirmed by XPS measurements and is consistent with a simple model for exchange bias. A proof of principle of electrochemical patterning of the domain structure has successfully been demonstrated. Based on these results, a voltage-reconfigurable domain pattern and stray field landscape, due to head-to-head domains, might be within reach.

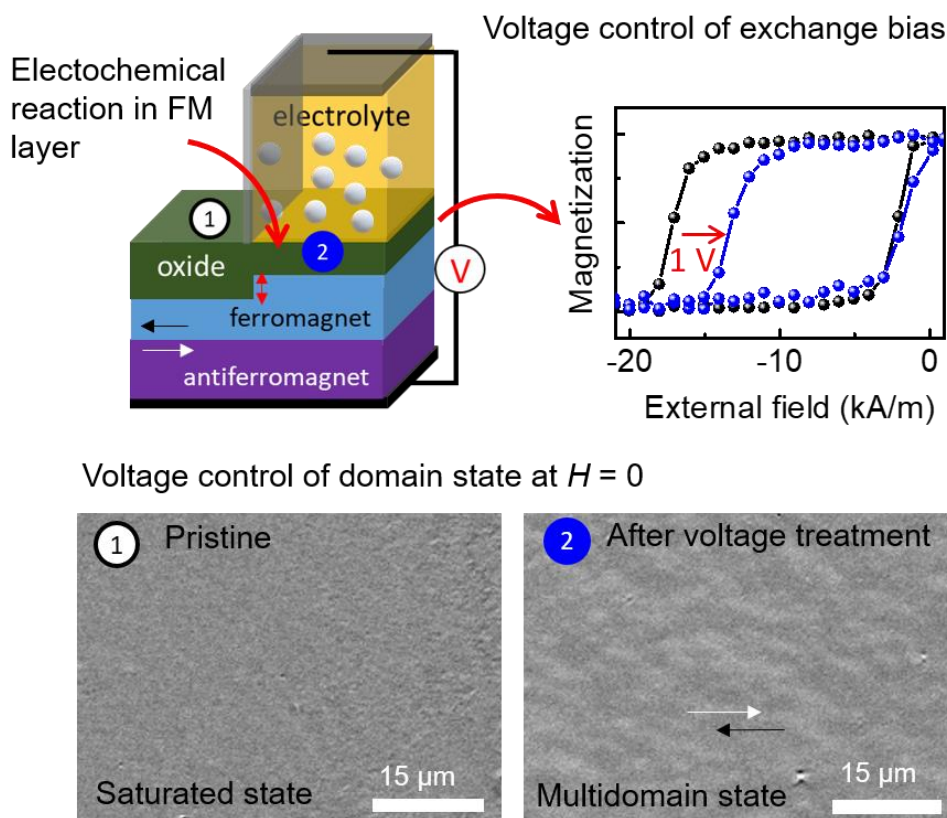


Figure 11.2: Visual summary of the findings in chapter 8

Voltage control of magnetic thin films with perpendicular unidirectional anisotropy (Chapter 9)

Chapter 9 continues with the investigation of voltage control of exchange bias phenomena in films with perpendicular anisotropy. We reported, for the first time, the successful fabrication of thin films with perpendicular exchange bias in a $\text{Au}/\text{GdO}_x/\text{Pd}/\text{Co}/\text{Pd}/\text{NiO}/\text{Pd}/\text{Ta}/\text{SiO}_2$ and in a $\text{Au}/\text{GdO}_x/\text{Pd}/\text{GdCo}/\text{Pd}/\text{NiO}/\text{Pd}/\text{Ta}/\text{SiO}_2$ structure. Such exchange bias structures are achieved with the help of a thin Pd interlayer, which stabilizes the metallic character of the Co or GdCo. The first gating step in the Pd/Co/Pd/NiO leads to a crystallization of the initially amorphous Pd/Co/Pd layer. The electrochemically induced magnetic changes lead to an on/off switching of the perpendicular exchange bias. The decrease of the exchange bias field with several gating steps is similar to the training or/and thermal aftereffect which is discussed as the possible origin of the observed changes in the Pd/Co/Pd/NiO structure. Upon gating a Pd/GdCo/Pd/NiO film, a sublattice switching of the ferrimagnetic GdCo is exploited to achieve a change of the exchange bias sign. The presented effects locally affect the exchange bias in a reversible manner. These results may show a path towards electrochemical control of exchange bias for spintronic devices in general.

With chapter 8 and 9, we fulfilled the second objective of the presented thesis, namely: To demonstrate novel concepts on the tuning of exchange bias at room temperature based on electrochemical reactions. These findings provide new insights into the mechanisms of voltage controlled magnetic properties by electrochemical reactions.

12 Appendix

Atomic force microscopy

Atomic force microscopy was conducted with a Bruker Dimension ScanAsyst with sub-nanometer resolution to characterize the sample morphology. The surface morphology is imaged with an atomic force microscope by moving a cantilever with an attached (ideally) atomic sharp tip across the sample. In the used tapping mode, the cantilever oscillates close to its resonance frequency. Due to attractive and repulsive van-der Waals forces between the sample surface and the tip, the resonant frequency changes, which results in a shift in oscillating amplitude and -phase of the cantilever. A laser beam is directed to- and reflected from the backside of the cantilever onto a quadrupole photo detector, in order to indirectly measure the force. [196] The software WSxM 5.0 was used for image editing and analyzing. [197]

Characterization of the surface morphology and grain size of the FeO_x/Fe layers

The surface morphology of the FeO_x/Fe layers was characterized by atomic force microscopy (AFM). The AFM images in **Figure 12.1** reveal the polycrystalline nature of the films and an average lateral grain size of about 30 nm.

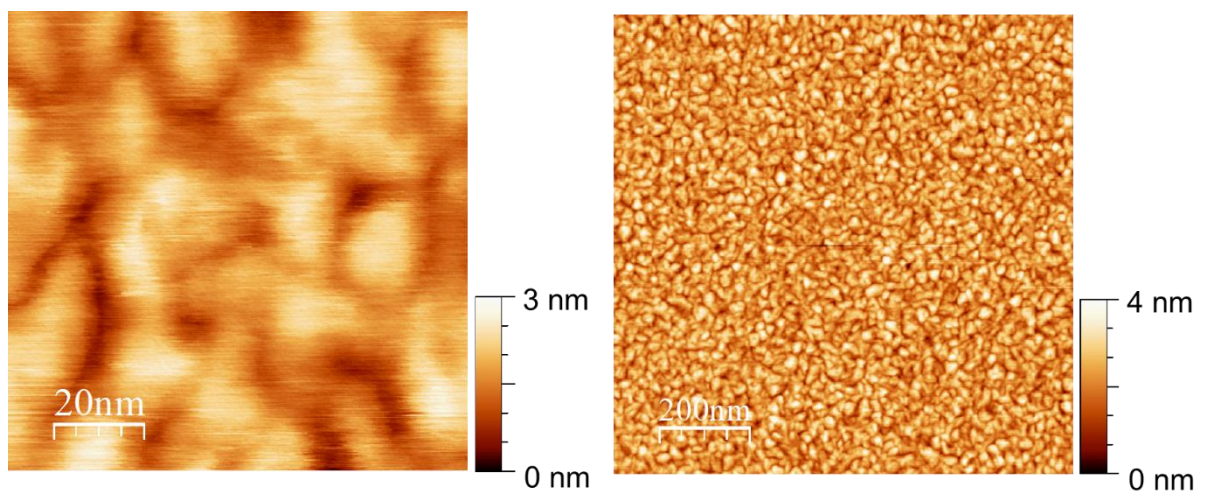


Figure 12.1: AFM images of the FeO_x/Fe/Au/Cr layers obtained in the tapping mode.

Raman spectroscopy for the characterization of the native FeO_x layer

By Raman spectroscopy, different iron oxides, such as Fe_3O_4 (magnetite), $\gamma\text{-Fe}_2\text{O}_3$ (maghemite), $\alpha\text{-Fe}_2\text{O}_3$ (hematite) can be distinguished. [198] The Raman spectrum of the FeO_x/Fe layer in pristine state (**Figure 12.2**) shows the typical Raman signature of magnetite, with a strong A_{1g} phonon mode peak at 661 cm^{-1} without peak splitting, and without further dominant peaks at higher or lower wave numbers. [199,200] This proves that magnetite is the predominant iron oxide phase in the present native oxide layer, in agreement with expectations for room temperature oxidation of iron in air. [101,102] Small amounts of other oxides and oxyhydroxides cannot be excluded, as they may yield intensities below the resolution limit, especially if they are not well crystallized.

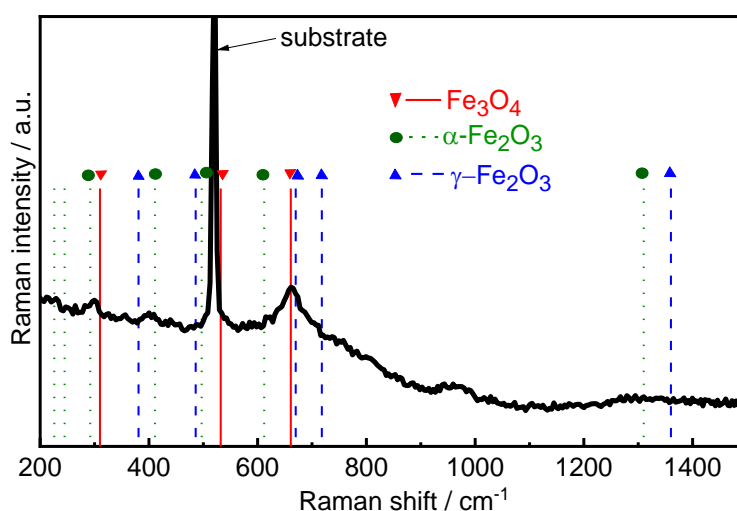


Figure 12.2. Raman spectra for the $\text{FeO}_x/\text{Fe}/\text{Au}/\text{Cr}$ layers after native oxidation, which identifies Fe_3O_4 as the dominant oxide. In Figure 3a, for the pristine state (black line), part of this curve (for the Raman shifts $400 - 700\text{ cm}^{-1}$) is displayed.

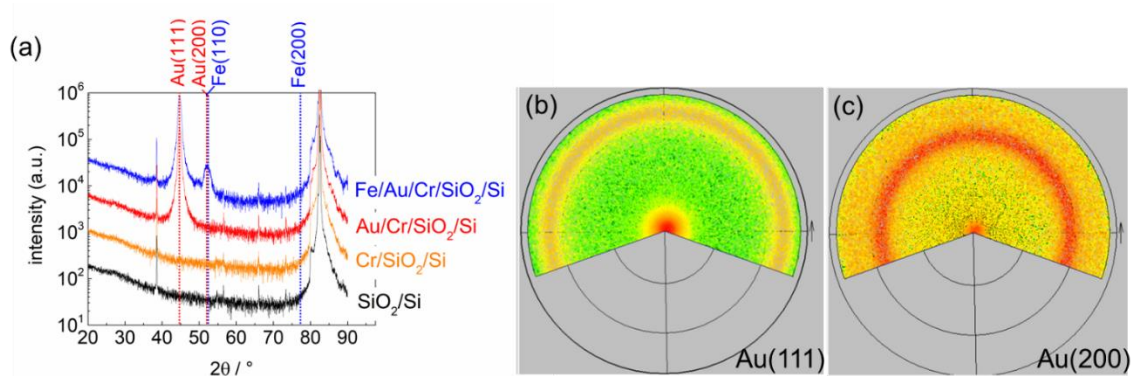
Structure and orientation of the Fe and Au layers on Cr/SiO₂/Si

Figure 12.3: X-ray diffraction on FeO_x/Fe/Au/Cr thin films.

a) X-ray diffraction spectra of the FeO_x/Fe/Au/Cr layers as compared with the Au/Cr and Cr buffer layers and the SiO₂/Si substrate. a) Au(111) and b) Au(200) pole figures of the Au/Cr layers on SiO₂/Si.

X-ray diffraction

X-ray diffraction (XRD) was used to collect structural information on a macroscopic scale for FeO_x/Fe/Au samples. The X-ray wavelength is similar to the lattice spacing of a crystal. The interaction of the X-rays with the crystal leads to constructive interference when Bragg's law is met. In the Bragg-Brentano geometry, structural information of the specimen with lattice planes parallel to the sample surface can be obtained. [201] XRD scans in Bragg Brentano geometry were collected on an X-ray diffraction Bruker D8 instrument using monochromatic Co-K α radiation with a wavelength of 0.17889 nm. The current and voltage of the X-ray tube were set to 40 mA and 40 kV, respectively. The usual two theta angle range was between 20° and 70°. An incremental step of 0.02°/s was used and the sample rotated in-plane at 0.5 Hz.

In order to determine the in-plane texture of a sample, pole figures were recorded. For this, the intensity of a given Bragg reflection is measured in dependence of the altitudinal and azimuthal angle with respect to the sample surface. The obtained pole distribution is plotted on a stereographic projection. For films with randomly in-plane (azimuthal) grain distribution, the projection will display a ring pattern of uniform intensity. [201]

Figure 12.3 (a) presents the X-ray diffraction (XRD) diagrams (Co K α radiation, θ -2 θ -geometry) for the gold and iron layers in comparison to the substrate. The fcc Au(111) reflex and the bcc Fe(110) reflex are observed for the gold layer and iron layer, respectively. In order to resolve the in-plane orientation, pole figure measurements (Cu K α radiation) were performed. Au(111) and Au(200) pole figures as measured for the Fe/Au/Cr layers deposited on SiO₂/Si substrate are presented in Figure 12.3 (b) and (c), respectively. A dominant (111) Au fiber texture is observed in accordance with the XRD results. Intensity rings in the pole figures confirm the random orientation of the Au grains in the film plane, which is as expected for the growth on amorphous SiO₂. Pole figures of

the iron layer have been measured but cannot be evaluated unambiguously due to the overlap of the Au(200) and Fe(110) reflexes.

The growth of epitaxial bcc Fe(110) films on Au(111), as indicated by the FFT (Figure 6.1 (a)), has been reported previously, although the lattice mismatch is high and the exact epitaxial relationship is controversial. [202,203]

We acknowledge Benjamin Schleicher and Stefan Schwabe (both IFW Dresden) for technical assistance and discussion regarding the pole figure measurements.

TEM crosssectional imaging of Au/Fe/Au structure

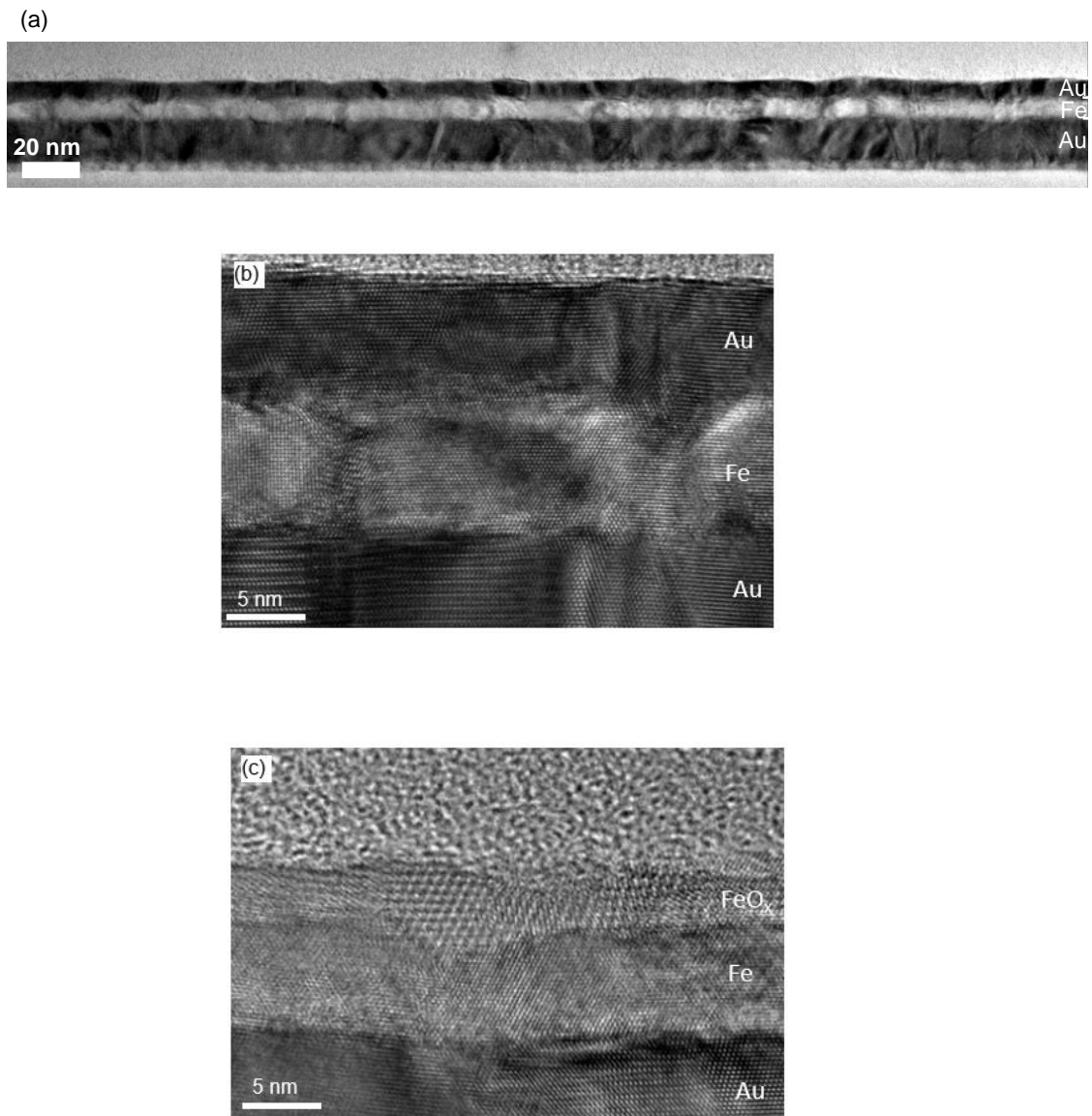


Figure 12.4: TEM crosssection of Au/Fe/Au thin film

(a) Overview image of the Au/Fe/Au structure and (b) high resolution image of the Au/Fe/Au structure. (c) high resolution image of the FeO_x/Fe/Au structure

Evaluation of charge transferred during the reduction of the FeO_x/Fe/Au layers

For the electrochemical reduction of iron ions to a metallic iron layer of a certain thickness, according to the reaction $\text{Fe}^{z+} + z\text{e}^- \rightarrow \text{Fe}$, the required charge density can be calculated from the Faraday's law (see details of the calculation in Ref. [2]). When starting from Fe₃O₄, this calculation yields a charge density q of 3.6 mC cm⁻², which is needed to form an iron layer of a thickness of 1 nm per 1 cm⁻². In **Figure 12.5** the reduction current density curve in dependence of the time at -1.10 V, and q derived from this curve by integration over time are plotted. q would suffice for a full transformation of Fe₃O₄ to 2 nm of iron after 12 s at -1.10 V, assuming 100 % current efficiency. This is only a rough estimation though, as some of the charge is consumed for proton reduction as a side reaction, which lowers current efficiency. A further indication, pointing at full transformation in the time scale of tens of seconds, is that for a reduction time of 20 s, the magnetization curves are stable over the measurement time of 60 s (e.g., presenting the same $\mu_0 H_C$ for the negative and the subsequent positive magnetic field sweep). In comparison to previous work on FeO_x/Fe/IrMn reduced in 1 mol l⁻¹ LiOH solution at -1.03 V, [2] the reduction is faster here, because of the more cathodic potential.

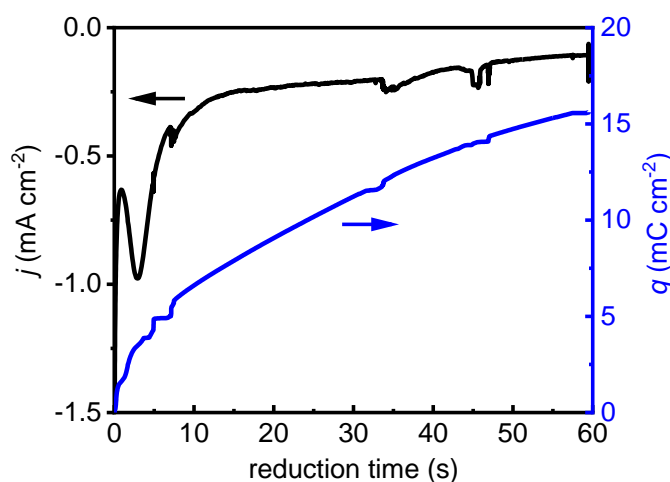


Figure 12.5. Cathodic current density j and inferred charge density q in dependence of the reduction time for the polarization of the FeO_x/Fe/Au layers at $E = -1.10$ V.

Angular dependency of the voltage-induced changes of M_R/M_S ratio and coercivity for higher angular resolution along the hard axis and in normalized view

For all angle-dependent measurements, the sample position remained constant during the measurement, while the application direction of the magnetic field was changed. This ensured that the measurements probe the same position on the sample, and that changes at a certain magnetic field direction are due to voltage application.

In **Figure 12.6** (a) and (b), the voltage-induced changes of coercivity and M_R/M_S ratio, respectively, are depicted for fields applied close to the hard axis with an angular resolution of 3° for the reduced state (-1.10 V). The measurements confirm the strong voltage-induced change of coercivity and M_R/M_S ratio near the hard axis. Coercivity and M_R/M_S ratio drop to 5% and 10% of the initial (pristine) value, respectively.

Figure 12.6 (c) and (d) show the normalized angle-dependent coercivity and M_R/M_S ratio, respectively, for the $\text{FeO}_x/\text{Fe}/\text{Au}$ films in the pristine state and the reduced state (-1.10 V). For both coercivity and M_R/M_S ratio, the angle-dependent values differ more strongly in the reduced than in the pristine state. This indicates that the magnitude of the uniaxial anisotropy increases when reducing the films.

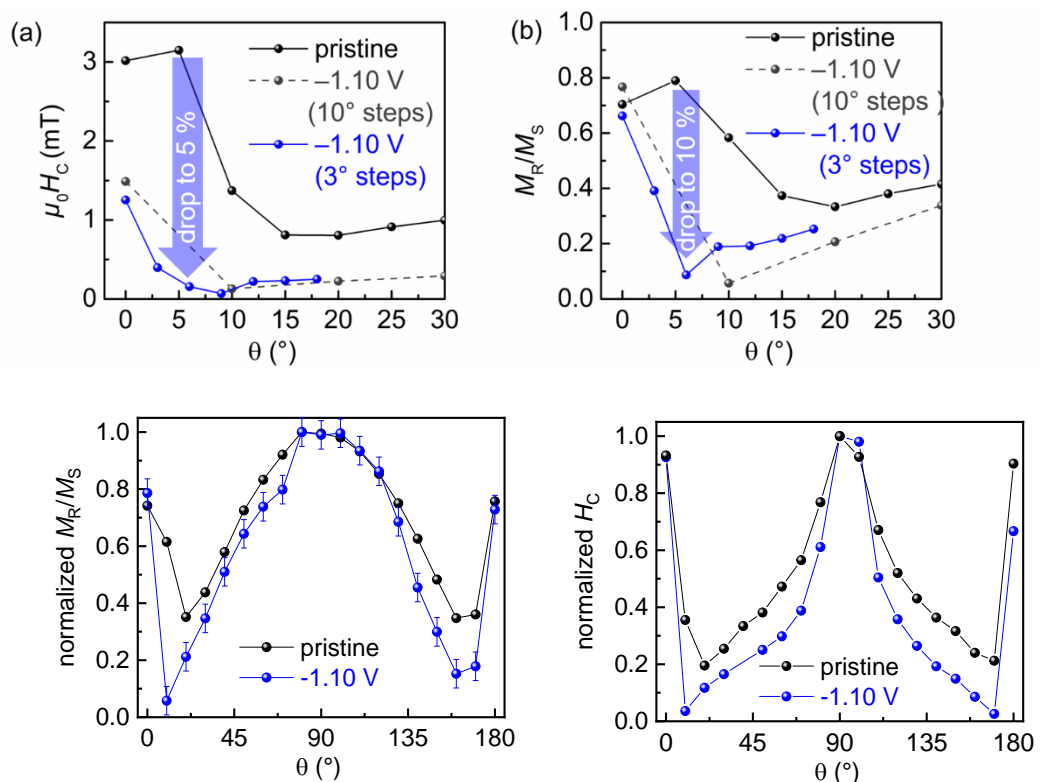


Figure 12.6: Angle-dependency of a,c) H_C and b,d) M_R/M_S in normalized view (a,b) and close to the hard axis in absolute values (c,d) for the pristine $\text{FeO}_x/\text{Fe}/\text{Au}$ films (black symbols) and during the application of -1.10 V (blue symbols). Lines are guides to the eye.

Average domain width analysis

For the quantification of the average domain width, the domain walls were counted along ten equidistant horizontal lines in the Kerr microscopy image (Figure 12.7). The number of domain walls per line was divided by the image width to obtain domain walls per μm . Then, the values obtained for the ten lines were averaged.

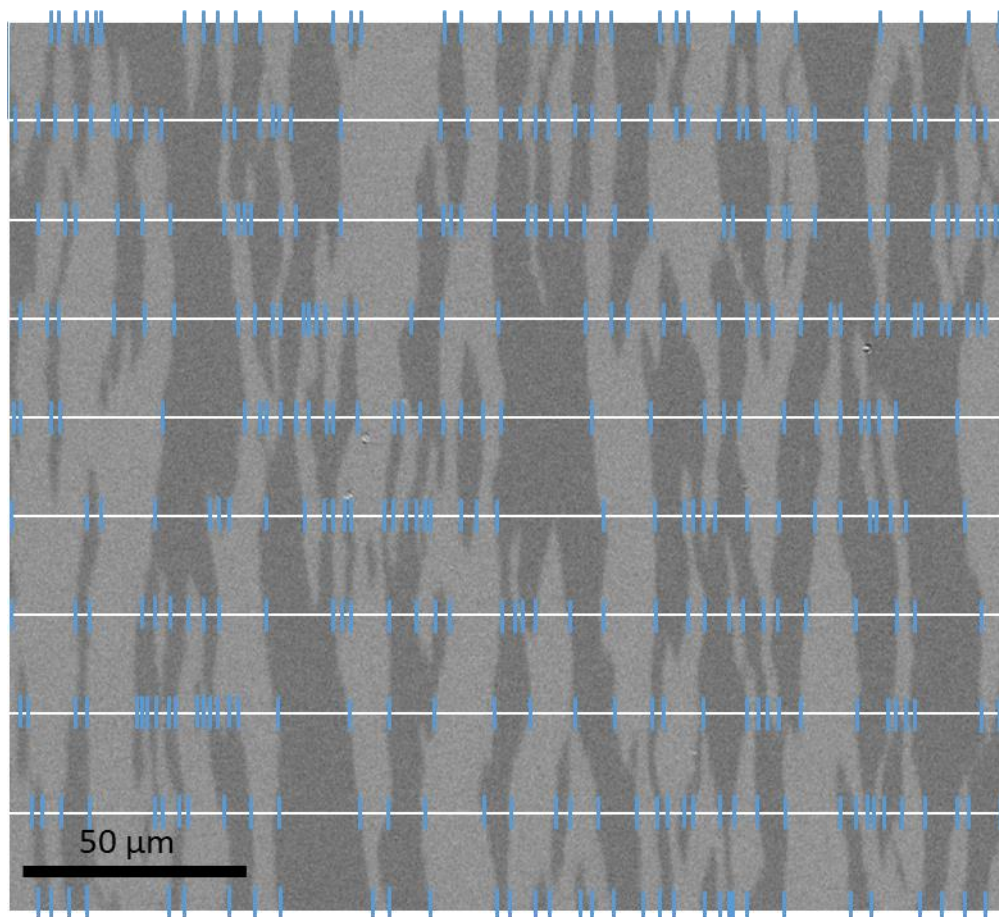


Figure 12.7: Example for the analysis of the number of domain walls per line width in a Kerr microscopy image to quantify the average domain width.

Cyclic voltammetry of the FeO_x/Fe/IrMn system in the electrolyte

The electrochemical behavior of the FeO_x/Fe/IrMn system in the electrolyte was characterized by cyclic voltammetry (CV) in the electrochemical cell implemented in the Kerr microscope setup. Pt wires are used as counter and reference electrodes. **Figure S1** shows the first cycle of the CV obtained for an FeO_x/Fe/IrMn system. The CV started at the open circuit potential (-0.230 V). The observed behavior is as expected for Fe in alkaline solution. [140] Peak C2 corresponds to the reduction of native iron oxide to metallic iron, followed by the hydrogen evolution reaction leading to the further strong cathodic current density increase. After potential reversal, the anodic peaks A1 and A2 indicate re-oxidation of metal iron to iron oxide.

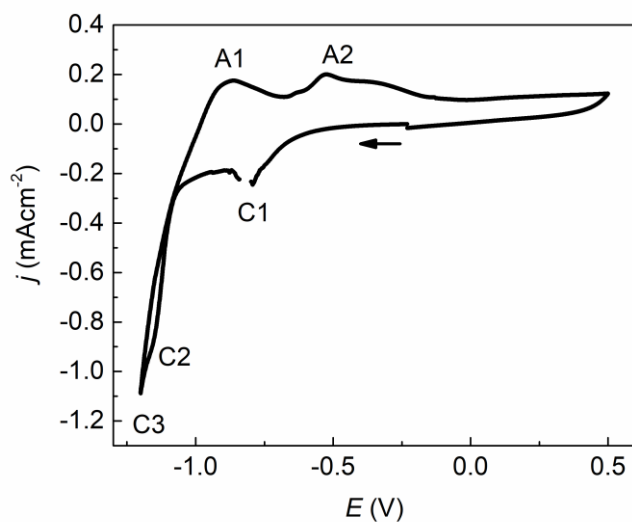


Figure 12.8. Cyclic voltammogram of an FeO_x/Fe/IrMn system with $d_{\text{Fe,nom}} = 11$ nm in 1 mol l⁻¹ LiOH, obtained at a rate of 20 mVs⁻¹

Exchange bias changes prior, during and after electrochemical treatment in the same area. In **Figure 12.9**, exemplary magnetization curves, from which the data in Figures 8.2 and 8.6 in the manuscript have been extracted, are presented. They directly show the impact of different kinds of electrochemical treatments on the magnetization curves in the exact same area.

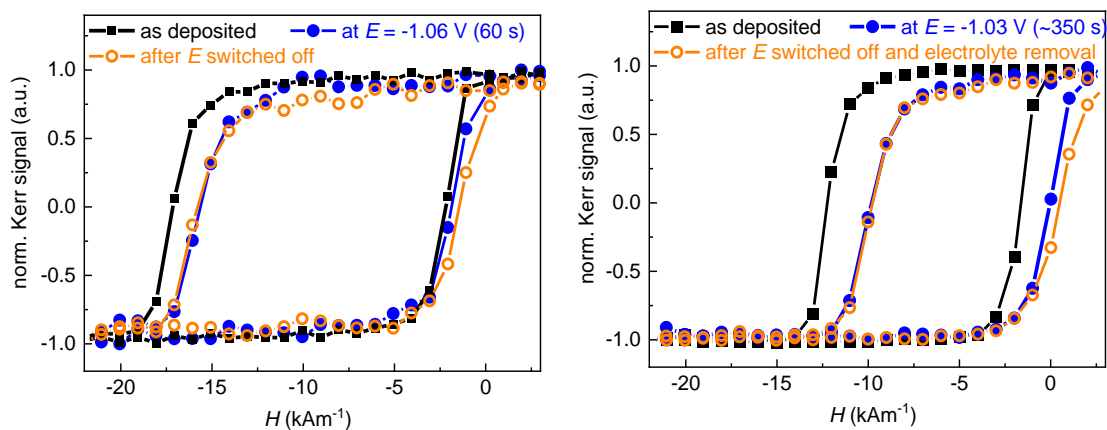


Figure 12.9. Magnetization curves of FeOx/Fe/IrMn systems

Measured in the in situ Kerr microscope setup in pristine state (black line), during the voltage application (blue line) and after voltage-switch off (orange line). These are exemplary curves from which the data in (a) Figure 2 and (b) Figure 6 have been extracted. The sample position and the measured area was not changed during the experiments.

Possible impact of antiferromagnetic iron oxides in the native oxide on EB variation

In natively oxidized Fe films prepared by sputtering in a magnetic field directly on the Au buffer layer without IrMn, no EB is observed (**Figure 12.10**), proving that the EB phenomena are connected to IrMn. In general, the composition of the native oxide layer of iron is highly dependent on the atmospheric conditions and the orientation of the iron surfaces. The exact composition is hard to resolve in many cases. Most often a structure composed of an ultrathin FeO layer followed by Fe₃O₄ and/or Fe₂O₃ as the outer layers is described. [136] Since FeO is antiferromagnetic below its Néel temperature T_N , exchange bias phenomena can indeed occur in the FeO-Fe system. However, the T_N of FeO is around 200 K, and the observation of EB in FeO_x-Fe systems thus usually requires field cooling procedures below room temperature. [140,204,205]

The present experiments are performed at room temperature where FeO is paramagnetic. Moreover, the occurrence of antiferromagnetism usually requires a critical thickness of the oxide. In the present case, EB variations caused by electrochemical modification of an interfacial FeO layer are thus not expected. Room temperature antiferromagnetism and EB phenomena are reported for some other iron oxides, such as α -Fe₂O₃, and iron oxyhydroxides. [136] In most cases though, the exchange energies and associated loop shifts are very small. [206] In the present experiments, the exact composition of the oxide layer and its modification especially at the FeO_x/Fe interface during the electrochemical treatment cannot be resolved in detail. EB modification via the electrochemical change of the iron oxide/iron interface thus cannot be fully excluded, but since the observed EB changes are large and fit well with the proposed Fe layer thickness model it is suggested that the modification of the native oxide is not important for the EB changes in the present case.

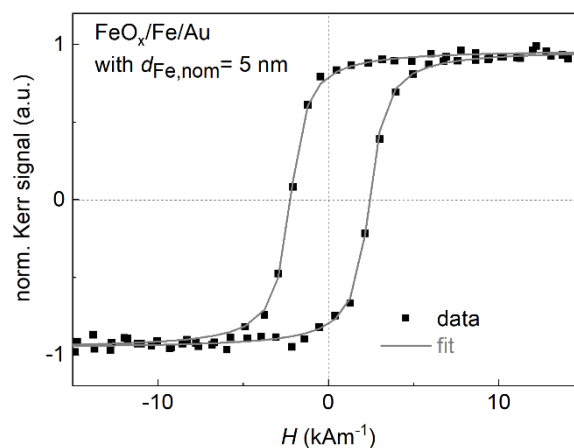


Figure 12.10. Magnetization curve of a FeO_x/Fe/Au(10nm) film with $d_{\text{Fe,nom}} = 5$ nm after sputtering and removal from the vacuum chamber

Lateral homogeneity of EB samples

To assess the lateral homogeneity of the EB systems in the pristine state, magnetization curves have been measured at different positions prior to electrochemical treatment (**Figure 12.11a**). The extracted H_{EB} and H_C values are plotted in Figure 12.11(b). Statistics give $H_{EB} = -8.39 (\pm 0.07) \text{ kAm}^{-1}$ and $H_C = 12.07 (\pm 0.44) \text{ kAm}^{-1}$. The error bars are significantly smaller than the change of H_{EB} induced by the electrochemical treatment.

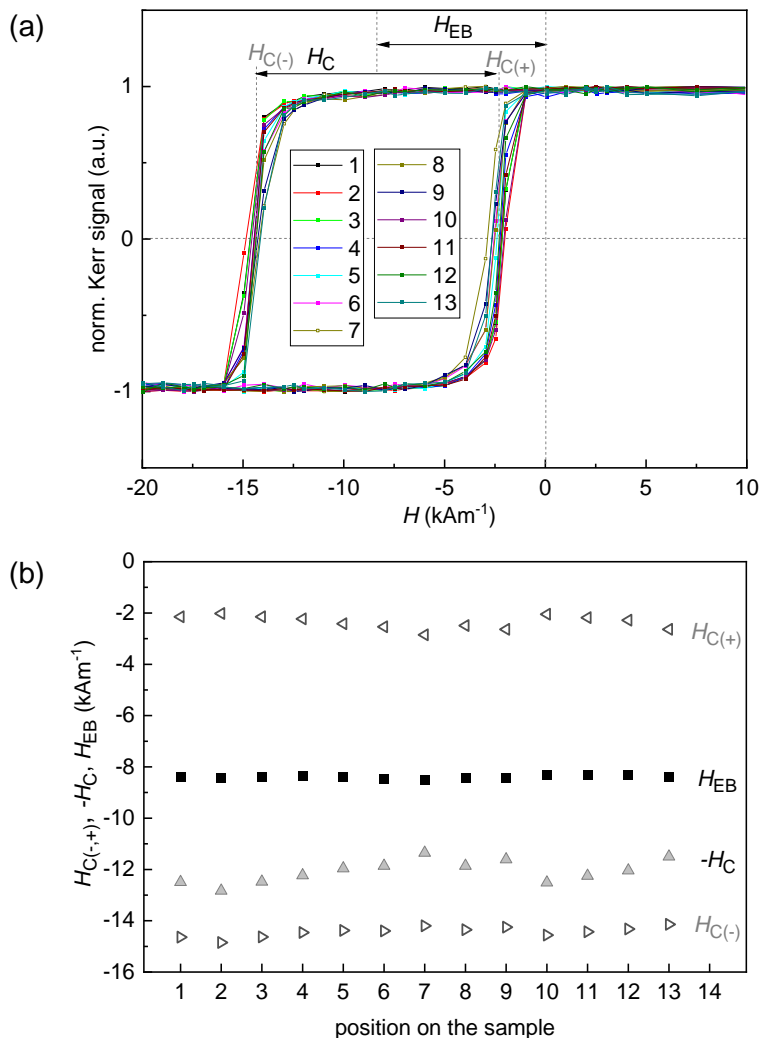


Figure 12.11. Magnetization curves measured in the pristine state at different positions across an FeOx/Fe/IrMn system with $d_{Fe,nom} = 13 \text{ nm}$. The inset depicts the measured positions on the sample area ($1 \times 1 \text{ cm}^2$). The grey line shows the position of the perimeter of the O-ring which defines the sample area that can be modified later on in the electrochemical cell.

Training effect

The decrease of the exchange bias as a function of n is fitted according to [177]:

$$H_{eb}^n = H_{eb}^\infty + A_f \exp(-n/P_f) + A_i \exp(-n/P_i),$$

where, H_{neb} is the exchange bias of the n th hysteresis loop, A_f and P_f are parameters related to the change of the frozen spins, A_i and P_i are parameters related to the evolution of the interfacial disorder. The obtained parameters are:

$$H_{eb}^\infty = 6.03 \frac{kA}{m} \pm 0.53 \frac{kA}{m}, \quad A_f = 55.70 \frac{kA}{m} (set), \quad P_f = 0.29 \pm 0.02,$$

$$A_i = 3.76 \frac{kA}{m} \pm 0.33 \frac{kA}{m}, \quad P_i = 4.35 \pm 1.20,$$

Note, without setting A_f , the error would be larger than the obtained value and the fit would not converge. Nevertheless, the relative ratio of P_f/P_i is always larger 1 even when A_f is not set.

The relative ratio between P_f/P_i signifies the difference in the relaxation of both frozen and rotatable spin components. The observed value of P_r is much greater than that of P_f , which clearly indicates that the spin-flipping components relax faster than the frozen spin components at the pinning surface. This behavior might be ascribed as a relaxor behavior.

Overall, this equation was developed for common training effects where no phase change occurs which breaks the direct scaling of H_{EB} and H_C . The uncertainty in the parameter A_f might partly arise from the superimposed phase change.

References

- [1] J. Zehner, I. Soldatov, S. Schneider, R. Heller, N. B. Khojasteh, S. Schiemenz, S. Fähler, K. Nielsch, R. Schäfer, and K. Leistner, *Voltage-Controlled Deblocking of Magnetization Reversal in Thin Films by Tunable Domain Wall Interactions and Pinning Sites*, *Adv. Electron. Mater.* **6**, 2000406 (2020).
- [2] J. Zehner, R. Huhnstock, S. Oswald, U. Wolff, I. Soldatov, A. Ehresmann, K. Nielsch, D. Holzinger, and K. Leistner, *Nonvolatile Electric Control of Exchange Bias by a Redox Transformation of the Ferromagnetic Layer*, *Adv. Electron. Mater.* **5**, 1900296 (2019).
- [3] J. Zehner, D. Wolf, M. U. Hasan, M. Huang, D. Bono, K. Nielsch, K. Leistner, and G. S. D. Beach, *Magnetoionic Control of Perpendicular Exchange Bias*, *Phys. Rev. Materials* **5**, L061401 (2021).
- [4] J. Puebla, J. Kim, K. Kondou, and Y. Otani, *Spintronic Devices for Energy-Efficient Data Storage and Energy Harvesting*, *Commun. Mater.* **1**, 24 (2020).
- [5] C. Song, B. Cui, F. Li, X. Zhou, and F. Pan, *Recent Progress in Voltage Control of Magnetism: Materials, Mechanisms, and Performance*, *Prog. Mater. Sci.* **87**, 33 (2017).
- [6] A. Molinari, H. Hahn, and R. Kruk, *Voltage-Control of Magnetism in All-Solid-State and Solid/Liquid Magnetolectric Composites*, *Adv. Mater.* **31**, 1806662 (2019).
- [7] C. Leighton, *Electrolyte-Based Ionic Control of Functional Oxides*, *Nat. Mater.* **18**, 13 (2019).
- [8] T. Taniyama, *Electric-Field Control of Magnetism via Strain Transfer across Ferromagnetic/Ferroelectric Interfaces*, *Journal of Physics: Condensed Matter* **27**, 504001 (2015).
- [9] C. Navarro-Senent, A. Quintana, E. Menéndez, E. Pellicer, and J. Sort, *Electrolyte-Gated Magnetolectric Actuation: Phenomenology, Materials, Mechanisms, and Prospective Applications*, *APL Mater.* **7**, 030701 (2019).
- [10] K. Leistner, J. Wunderwald, N. Lange, S. Oswald, M. Richter, H. Zhang, L. Schultz, and S. Fähler, *Electric-Field Control of Magnetism by Reversible Surface Reduction and Oxidation Reactions*, *Physical Review B* **87**, 224411 (2013).
- [11] U. Bauer, L. Yao, A. J. Tan, P. Agrawal, S. Emori, H. L. Tuller, S. van Dijken, and G. S. D. Beach, *Magneto-Ionic Control of Interfacial Magnetism*, *Nat. Mater.* **14**, 174 (2015).
- [12] K. Taniguchi, K. Narushima, H. Sagayama, W. Kosaka, N. Shito, and H. Miyasaka, *In Situ Reversible Ionic Control for Nonvolatile Magnetic Phases in a Donor/Acceptor Metal-Organic Framework*, *Advanced Functional Materials* **27**, 1604990 (2017).
- [13] K. Duschek, D. Pohl, S. Fähler, K. Nielsch, and K. Leistner, *Research Update: Magnetoionic Control of Magnetization and Anisotropy in Layered Oxide/Metal Heterostructures*, *APL Mater.* **4**, 032301 (2016).
- [14] D. A. Gilbert, A. J. Grutter, E. Arenholz, K. Liu, B. J. Kirby, J. A. Borchers, and B. B. Maranville, *Structural and Magnetic Depth Profiles of Magneto-Ionic Heterostructures beyond the Interface Limit*, *Nat. Commun.* **7**, 12264 (2016).
- [15] R. Mishra, D. Kumar, and H. Yang, *Oxygen-Migration-Based Spintronic Device Emulating a Biological Synapse*, *Phys. Rev. Appl.* **11**, 054065 (2019).

- [16] D. Holzinger, D. Lengemann, F. Göllner, D. Engel, and A. Ehresmann, *Controlled Movement of Superparamagnetic Bead Rows for Microfluid Mixing*, *Appl. Phys. Lett.* **100**, 153504 (2012).
- [17] S. Rampini, P. Li, and G. U. Lee, *Micromagnet Arrays Enable Precise Manipulation of Individual Biological Analyte–Superparamagnetic Bead Complexes for Separation and Sensing*, *Lab Chip* **16**, 3645 (2016).
- [18] D. Sander, S. O. Valenzuela, D. Makarov, C. H. Marrows, E. E. Fullerton, P. Fischer, J. McCord, P. Vavassori, S. Mangin, P. Pirro, B. Hillebrands, A. D. Kent, T. Jungwirth, O. Gutfleisch, C. G. Kim, and A. Berger, *The 2017 Magnetism Roadmap*, *J. Phys. D: Appl. Phys.* **50**, 363001 (2017).
- [19] M. Gößler, M. Albu, G. Klinser, E. Steyskal, H. Krenn, and R. Würschum, *Magneto-Ionic Switching of Superparamagnetism*, *Small* **15**, 1904523 (2019).
- [20] A. J. Tan, M. Huang, C. O. Avci, F. Büttner, M. Mann, W. Hu, C. Mazzoli, S. Wilkins, H. L. Tuller, and G. S. D. Beach, *Magneto-Ionic Control of Magnetism Using a Solid-State Proton Pump*, *Nat. Mater.* **18**, 35 (2019).
- [21] N. Tournerie, A. P. Engelhardt, F. Maroun, and P. Allongue, *Influence of the Surface Chemistry on the Electric-Field Control of the Magnetization of Ultrathin Films*, *Physical Review B* **86**, (2012).
- [22] K. Leistner, N. Lange, J. Hänisch, S. Oswald, F. Scheiba, S. Fähler, H. Schlörb, and L. Schultz, *Electrode Processes and in Situ Magnetic Measurements of FePt Films in a LiPF₆ Based Electrolyte*, *Electrochimica Acta* **81**, 330 (2012).
- [23] L. Herrera Diez, Y. T. Liu, D. A. Gilbert, M. Belmeguenai, J. Vogel, S. Pizzini, E. Martinez, A. Lamperti, J. B. Mohammedi, A. Laborieux, Y. Roussigné, A. J. Grutter, E. Arenholtz, P. Quarterman, B. Maranville, S. Ono, M. S. E. Hadri, R. Tolley, E. E. Fullerton, L. Sanchez-Tejerina, A. Stashkevich, S. M. Chérif, A. D. Kent, D. Querlioz, J. Langer, B. Ocker, and D. Ravelosona, *Nonvolatile Ionic Modification of the Dzyaloshinskii-Moriya Interaction*, *Phys. Rev. Appl.* **12**, 034005 (2019).
- [24] P. Dhanapal, T. Zhang, B. Wang, H. Yang, H. Xuan, C. Bi, W. Wang, and R.-W. Li, *Reversibly Controlled Magnetic Domains of Co Film via Electric Field Driven Oxygen Migration at Nanoscale*, *Applied Physics Letters* **114**, 232401 (2019).
- [25] X. Chen, X. Zhu, W. Xiao, G. Liu, Y. P. Feng, J. Ding, and R.-W. Li, *Nanoscale Magnetization Reversal Caused by Electric Field-Induced Ion Migration and Redistribution in Cobalt Ferrite Thin Films*, *ACS Nano* **9**, 4210 (2015).
- [26] *ON THE THEORY OF THE DISPERSION OF MAGNETIC PERMEABILITY IN FERROMAGNETIC BODIES*, in *Collected Papers of L.D. Landau* (Elsevier, 1965), pp. 101–114.
- [27] R. Hilzinger and W. Rodewald, *Magnetic Materials: Fundamentals, Products, Properties, and Applications* (Publicis ; VAC, VACUUMSCHMELZE, Erlangen : Hanau, Germany, 2013).
- [28] J. M. D. Coey, *Magnetism and Magnetic Materials*, 1st ed. (Cambridge University Press, 2001).
- [29] A. Hubert and R. Schäfer, *Magnetic Domains* (Springer Verlag Berlin Heidelberg, Berlin, Heidelberg, 1998).
- [30] M. T. Johnson, P. J. H. Bloemen, F. J. A. den Broeder, and J. J. de Vries, *Magnetic Anisotropy in Metallic Multilayers*, *Rep. Prog. Phys.* **59**, 1409 (1996).
- [31] R. C. O’Handley, *Modern Magnetic Materials: Principles and Applications* (Wiley, New York, 2000).

- [32] W. H. Meiklejohn and C. P. Bean, *New Magnetic Anisotropy*, Phys. Rev. **105**, 904 (1957).
- [33] W. H. Meiklejohn, *Exchange Anisotropy—A Review*, Journal of Applied Physics **33**, 1328 (1962).
- [34] J. Nogués, J. Sort, V. Langlais, V. Skumryev, S. Suriñach, J. S. Muñoz, and M. D. Baró, *Exchange Bias in Nanostructures*, Physics Reports **422**, 65 (2005).
- [35] A. E. Berkowitz and K. Takano, *Exchange Anisotropy — a Review*, Journal of Magnetism and Magnetic Materials **200**, 552 (1999).
- [36] F. Radu and H. Zabel, *Exchange Bias Effect of Ferro-/Antiferromagnetic Heterostructures*, in *Magnetic Heterostructures*, edited by H. Zabel and S. D. Bader, Vol. 227 (Springer Berlin Heidelberg, Berlin, Heidelberg, 2008), pp. 97–184.
- [37] J. Kerr, *XLIII. On Rotation of the Plane of Polarization by Reflection from the Pole of a Magnet*, The London, Edinburgh, and Dublin Philosophical Magazine and Journal of Science **3**, 321 (1877).
- [38] J. Kerr, *XXIV. On Reflection of Polarized Light from the Equatorial Surface of a Magnet*, The London, Edinburgh, and Dublin Philosophical Magazine and Journal of Science **5**, 161 (1878).
- [39] F. Matsukura, Y. Tokura, and H. Ohno, *Control of Magnetism by Electric Fields*, Nature Nanotech **10**, 209 (2015).
- [40] D. A. Gilbert, J. Olamit, R. K. Dumas, B. J. Kirby, A. J. Grutter, B. B. Maranville, E. Arenholz, J. A. Borchers, and K. Liu, *Controllable Positive Exchange Bias via Redox-Driven Oxygen Migration*, Nat. Commun. **7**, 11050 (2016).
- [41] F. Bonell, Y. T. Takahashi, D. D. Lam, S. Yoshida, Y. Shiota, S. Miwa, T. Nakamura, and Y. Suzuki, *Reversible Change in the Oxidation State and Magnetic Circular Dichroism of Fe Driven by an Electric Field at the FeCo/MgO Interface*, Appl. Phys. Lett. **102**, 152401 (2013).
- [42] C. Bi, Y. Liu, T. Newhouse-Illige, M. Xu, M. Rosales, J. W. Freeland, O. Mryasov, S. Zhang, S. G. E. te Velthuis, and W. G. Wang, *Reversible Control of Co Magnetism by Voltage-Induced Oxidation*, Phys. Rev. Lett. **113**, 267202 (2014).
- [43] K. Duschek, A. Petr, J. Zehner, K. Nielsch, and K. Leistner, *All-Electrochemical Voltage-Control of Magnetization in Metal Oxide/Metal Nanoislands*, J. Mater. Chem. C **6**, 8411 (2018).
- [44] H. Ohno, D. Chiba, F. Matsukura, T. Omiya, E. Abe, T. Dietl, Y. Ohno, and K. Ohtani, *Electric-Field Control of Ferromagnetism*, Nature **408**, 944 (2000).
- [45] D. Chiba, M. Sawicki, Y. Nishitani, Y. Nakatani, F. Matsukura, and H. Ohno, *Magnetization Vector Manipulation by Electric Fields*, Nature **455**, 515 (2008).
- [46] T. Lottermoser, T. Lonkai, U. Amann, D. Hohlwein, J. Ihringer, and M. Fiebig, *Magnetic Phase Control by an Electric Field*, Nature **430**, 541 (2004).
- [47] K. J. A. Franke, B. Van de Wiele, Y. Shirahata, S. J. Hämäläinen, T. Taniyama, and S. van Dijken, *Reversible Electric-Field-Driven Magnetic Domain-Wall Motion*, Phys. Rev. X **5**, 011010 (2015).
- [48] D. López González, Y. Shirahata, B. Van de Wiele, K. J. A. Franke, A. Casiraghi, T. Taniyama, and S. van Dijken, *Electric-Field-Driven Domain Wall Dynamics in Perpendicularly Magnetized Multilayers*, AIP Advances **7**, 035119 (2017).

- [49] Y. Shirahata, R. Shiina, D. L. González, K. J. A. Franke, E. Wada, M. Itoh, N. A. Pertsev, S. van Dijken, and T. Taniyama, *Electric-Field Switching of Perpendicularly Magnetized Multilayers*, NPG Asia Mater **7**, e198 (2015).
- [50] N. Lei, T. Devolder, G. Agnus, P. Aubert, L. Daniel, J.-V. Kim, W. Zhao, T. Trypiniotis, R. P. Cowburn, C. Chappert, D. Ravelosona, and P. Lecoeur, *Strain-Controlled Magnetic Domain Wall Propagation in Hybrid Piezoelectric/Ferromagnetic Structures*, Nat. Commun. **4**, 1378 (2013).
- [51] T. H. E. Lahtinen, J. O. Tuomi, and S. van Dijken, *Pattern Transfer and Electric-Field-Induced Magnetic Domain Formation in Multiferroic Heterostructures*, Adv. Mater. **23**, 3187 (2011).
- [52] K. Nakamura, R. Shimabukuro, Y. Fujiwara, T. Akiyama, T. Ito, and A. J. Freeman, *Giant Modification of the Magnetocrystalline Anisotropy in Transition-Metal Monolayers by an External Electric Field*, Phys. Rev. Lett. **102**, 187201 (2009).
- [53] M. Weisheit, S. Fahler, A. Marty, Y. Souche, C. Poinignon, and D. Givord, *Electric Field-Induced Modification of Magnetism in Thin-Film Ferromagnets*, Science **315**, 349 (2007).
- [54] T. Maruyama, Y. Shiota, T. Nozaki, K. Ohta, N. Toda, M. Mizuguchi, A. A. Tulapurkar, T. Shinjo, M. Shiraishi, S. Mizukami, Y. Ando, and Y. Suzuki, *Large Voltage-Induced Magnetic Anisotropy Change in a Few Atomic Layers of Iron*, Nature Nanotech **4**, 158 (2009).
- [55] K. Shimamura, D. Chiba, S. Ono, S. Fukami, N. Ishiwata, M. Kawaguchi, K. Kobayashi, and T. Ono, *Electrical Control of Curie Temperature in Cobalt Using an Ionic Liquid Film*, Applied Physics Letters **100**, 122402 (2012).
- [56] Y. T. Liu, S. Ono, G. Agnus, J.-P. Adam, S. Jaiswal, J. Langer, B. Ocker, D. Ravelosona, and L. Herrera Diez, *Electric Field Controlled Domain Wall Dynamics and Magnetic Easy Axis Switching in Liquid Gated CoFeB/MgO Films*, Journal of Applied Physics **122**, 133907 (2017).
- [57] Y. Wang, X. Zhou, C. Song, Y. Yan, S. Zhou, G. Wang, C. Chen, F. Zeng, and F. Pan, *Electrical Control of the Exchange Spring in Antiferromagnetic Metals*, Adv. Mater. **27**, 3196 (2015).
- [58] T. Hirai, T. Koyama, and D. Chiba, *Electric Field Modulation of Exchange Bias at the Co / Co O x Interface*, Phys. Rev. B **101**, 014447 (2020).
- [59] M. Endo, S. Kanai, S. Ikeda, F. Matsukura, and H. Ohno, *Electric-Field Effects on Thickness Dependent Magnetic Anisotropy of Sputtered MgO/Co₄₀Fe₄₀B₂₀/Ta Structures*, Appl. Phys. Lett. **96**, 212503 (2010).
- [60] F. Bonell, S. Murakami, Y. Shiota, T. Nozaki, T. Shinjo, and Y. Suzuki, *Large Change in Perpendicular Magnetic Anisotropy Induced by an Electric Field in FePd Ultrathin Films*, Appl. Phys. Lett. **98**, 232510 (2011).
- [61] D. Chiba and T. Ono, *Control of Magnetism in Co by an Electric Field*, Journal of Physics D: Applied Physics **46**, 213001 (2013).
- [62] Y. Shiota, T. Nozaki, F. Bonell, S. Murakami, T. Shinjo, and Y. Suzuki, *Induction of Coherent Magnetization Switching in a Few Atomic Layers of FeCo Using Voltage Pulses*, Nat. Mater. **11**, 39 (2012).
- [63] O. O. Brovko, P. Ruiz-Díaz, T. R. Dasa, and V. S. Stepanyuk, *Controlling Magnetism on Metal Surfaces with Non-Magnetic Means: Electric Fields and Surface Charging*, Journal of Physics: Condensed Matter **26**, 093001 (2014).

- [64] M. Kawaguchi, K. Shimamura, S. Ono, S. Fukami, F. Matsukura, H. Ohno, D. Chiba, and T. Ono, *Electric Field Effect on Magnetization of an Fe Ultrathin Film*, Applied Physics Express **5**, 063007 (2012).
- [65] L. Herrera Diez, A. Bernand-Mantel, L. Vila, P. Warin, A. Marty, S. Ono, D. Givord, and L. Ranno, *Electric-Field Assisted Depinning and Nucleation of Magnetic Domain Walls in FePt/Al₂O₃/Liquid Gate Structures*, Applied Physics Letters **104**, 082413 (2014).
- [66] A. Bernand-Mantel, L. Herrera-Diez, L. Ranno, S. Pizzini, J. Vogel, D. Givord, S. Auffret, O. Boulle, I. M. Miron, and G. Gaudin, *Electric-Field Control of Domain Wall Nucleation and Pinning in a Metallic Ferromagnet*, Applied Physics Letters **102**, 122406 (2013).
- [67] F. Ando, H. Kakizakai, T. Koyama, K. Yamada, M. Kawaguchi, S. Kim, K.-J. Kim, T. Moriyama, D. Chiba, and T. Ono, *Modulation of the Magnetic Domain Size Induced by an Electric Field*, Applied Physics Letters **109**, 022401 (2016).
- [68] W. Lin, N. Vernier, G. Agnus, K. Garcia, B. Ocker, W. Zhao, E. E. Fullerton, and D. Ravelosona, *Universal Domain Wall Dynamics under Electric Field in Ta/CoFeB/MgO Devices with Perpendicular Anisotropy*, Nat. Commun. **7**, (2016).
- [69] A. J. Schellekens, A. van den Brink, J. H. Franken, H. J. M. Swagten, and B. Koopmans, *Electric-Field Control of Domain Wall Motion in Perpendicularly Magnetized Materials*, Nat. Commun. **3**, (2012).
- [70] H. Kakizakai, F. Ando, T. Koyama, K. Yamada, M. Kawaguchi, S. Kim, K.-J. Kim, T. Moriyama, D. Chiba, and T. Ono, *Switching Local Magnetization by Electric-Field-Induced Domain Wall Motion*, Applied Physics Express **9**, 063004 (2016).
- [71] U. Bauer, S. Emori, and G. S. D. Beach, *Voltage-Controlled Domain Wall Traps in Ferromagnetic Nanowires*, Nat. Nanotechnol. **8**, 411 (2013).
- [72] X. Zhou, Y. Yan, M. Jiang, B. Cui, F. Pan, and C. Song, *Role of Oxygen Ion Migration in the Electrical Control of Magnetism in Pt/Co/Ni/HfO₂ Films*, The Journal of Physical Chemistry C **120**, 1633 (2016).
- [73] N. Di, J. Kubal, Z. Zeng, J. Greeley, F. Maroun, and P. Allongue, *Influence of Controlled Surface Oxidation on the Magnetic Anisotropy of Co Ultrathin Films*, Appl. Phys. Lett. **106**, 122405 (2015).
- [74] H. L. Wang, Y. Wu, H. J. Yu, Y. Jiang, and J. H. Zhao, *Manipulation of Magnetism in Perpendicularly Magnetized Heusler Alloy Co₂FeAl_{0.5}Si_{0.5} by Electric-Field at Room Temperature*, Journal of Applied Physics **120**, 093901 (2016).
- [75] A. van den Brink, M. A. J. van der Heijden, H. J. M. Swagten, and B. Koopmans, *Large Time-Dependent Coercivity and Resistivity Modification under Sustained Voltage Application in a Pt/Co/AlOx/Pt Junction*, Journal of Applied Physics **117**, 17C717 (2015).
- [76] U. Bauer, S. Emori, and G. S. D. Beach, *Electric Field Control of Domain Wall Propagation in Pt/Co/GdOx Films*, Appl. Phys. Lett. **100**, 192408 (2012).
- [77] K. Klyukin, G. Beach, and B. Yildiz, *Hydrogen Tunes Magnetic Anisotropy by Affecting Local Hybridization at the Interface of a Ferromagnet with Nonmagnetic Metals*, Phys. Rev. Materials **4**, 104416 (2020).
- [78] A. J. Tan, M. Huang, S. Sheffels, F. Büttner, S. Kim, A. H. Hunt, I. Waluyo, H. L. Tuller, and G. S. D. Beach, *Hydration of Gadolinium Oxide (GdO_x) and Its*

- Effect on Voltage-Induced Co Oxidation in a Pt / Co / Gd O x / Au Heterostructure*, Phys. Rev. Materials **3**, 064408 (2019).
- [79] A. D. Lamirand, J.-P. Adam, D. Ravelosona, P. Allongue, and F. Maroun, *In Situ Monitoring of Electric Field Effect on Domain Wall Motion in Co Ultrathin Films in Direct Contact with an Electrolyte*, Applied Physics Letters **115**, 032402 (2019).
- [80] A. Mougín, T. Mewes, M. Jung, D. Engel, A. Ehresmann, H. Schmoranzer, J. Fassbender, and B. Hillebrands, *Local Manipulation and Reversal of the Exchange Bias Field by Ion Irradiation in FeNi/FeMn Double Layers*, Phys. Rev. B **63**, 060409 (2001).
- [81] T. Mewes, R. Lopusnik, J. Fassbender, B. Hillebrands, M. Jung, D. Engel, A. Ehresmann, and H. Schmoranzer, *Suppression of Exchange Bias by Ion Irradiation*, Appl. Phys. Lett. **76**, 1057 (2000).
- [82] X. He, Y. Wang, N. Wu, A. N. Caruso, E. Vescovo, K. D. Belashchenko, P. A. Dowben, and C. Binek, *Robust Isothermal Electric Control of Exchange Bias at Room Temperature*, Nat. Mater. **9**, 579 (2010).
- [83] S. Manipatruni, D. E. Nikonov, C.-C. Lin, B. Prasad, Y.-L. Huang, A. R. Damodaran, Z. Chen, R. Ramesh, and I. A. Young, *Voltage Control of Unidirectional Anisotropy in Ferromagnet-Multiferroic System*, Sci. Adv. **4**, eaat4229 (2018).
- [84] V. Laukhin, V. Skumryev, X. Martí, D. Hrabovský, F. Sánchez, M. V. García-Cuenca, C. Ferrater, M. Varela, U. Lüders, J. F. Bobo, and J. Fontcuberta, *Electric-Field Control of Exchange Bias in Multiferroic Epitaxial Heterostructures*, Phys. Rev. Lett. **97**, 227201 (2006).
- [85] M. Liu, J. Lou, S. Li, and N. X. Sun, *E-Field Control of Exchange Bias and Deterministic Magnetization Switching in AFM/FM/FE Multiferroic Heterostructures*, Adv. Funct. Mater. **21**, 2593 (2011).
- [86] A. Chen, Y. Zhao, P. Li, X. Zhang, R. Peng, H. Huang, L. Zou, X. Zheng, S. Zhang, P. Miao, Y. Lu, J. Cai, and C.-W. Nan, *Angular Dependence of Exchange Bias and Magnetization Reversal Controlled by Electric-Field-Induced Competing Anisotropies*, Adv. Mater. **28**, 363 (2016).
- [87] Q. Li, S. S. Yan, J. Xu, S. D. Li, G. X. Zhao, Y. Z. Long, T. T. Shen, K. Zhang, and J. Zhang, *Electrical Control of Exchange Bias via Oxygen Migration across CoO-ZnO Nanocomposite Barrier*, Appl. Phys. Lett. **109**, 252406 (2016).
- [88] Z. Wang, Y. Sun, X. Zhou, F. Pan, and C. Song, *Local Control of Exchange Bias by Resistive Switching*, Physica Status Solidi (RRL) – Rapid Research Letters **12**, 1800446 (2018).
- [89] L. Wei, Z. Hu, G. Du, Y. Yuan, J. Wang, H. Tu, B. You, S. Zhou, J. Qu, H. Liu, R. Zheng, Y. Hu, and J. Du, *Full Electric Control of Exchange Bias at Room Temperature by Resistive Switching*, Advanced Materials **30**, 1801885 (2018).
- [90] J. E. Greene, *Review Article: Tracing the Recorded History of Thin-Film Sputter Deposition: From the 1800s to 2017*, Journal of Vacuum Science & Technology A: Vacuum, Surfaces, and Films **35**, 05C204 (2017).
- [91] K. Vernon-Parry and A. Wright, *TEM: An Introduction — Part 2*, III-Vs Review **14**, 48 (2001).
- [92] D. B. Williams and C. B. Carter, *Transmission Electron Microscopy: A Textbook for Materials Science*, 2nd ed (Springer, New York, 2008).
- [93] M. Nichterwitz, S. Honnali, J. Zehner, S. Schneider, D. Pohl, S. Schiemenz, S. T. B. Goennenwein, K. Nielsch, and K. Leistner, *Control of Positive and Negative*

- Magnetoresistance in Iron Oxide–Iron Nanocomposite Thin Films for Tunable Magnetoelectric Nanodevices*, ACS Appl. Electron. Mater. **2**, 2543 (2020).
- [94] N. B. Khojasteh, S. Apelt, U. Bergmann, S. Facsko, and R. Heller, *Revealing the Formation Dynamics of the Electric Double Layer by Means of in - Situ Rutherford Backscattering Spectrometry*, Review of Scientific Instruments **90**, 085107 (2019).
- [95] M. Mayer, *SIMNRA, a Simulation Program for the Analysis of NRA, RBS and ERDA*, in *AIP Conference Proceedings* (AIP, Denton, Texas (USA), 1999), pp. 541–544.
- [96] V. V. Kharton, editor, *Solid State Electrochemistry* (Wiley-VCH, Weinheim ; Chichester, 2009).
- [97] I. V. Soldatov and R. Schäfer, *Selective Sensitivity in Kerr Microscopy*, Rev. Sci. Instrum. **88**, 073701 (2017).
- [98] F. Schmidt, W. Rave, and A. Hubert, *Enhancement of Magneto-Optical Domain Observation by Digital Image Processing*, IEEE Trans. Magn. **21**, 1596 (1985).
- [99] K. Duschek, M. Uhlemann, H. Schlörb, K. Nielsch, and K. Leistner, *Electrochemical and in Situ Magnetic Study of Iron/Iron Oxide Films Oxidized and Reduced in KOH Solution for Magneto-Ionic Switching*, Electrochemistry Communications **72**, 153 (2016).
- [100] R. M. Cornell and U. Schwertmann, *The Iron Oxides: Structure, Properties, Reactions, Occurrences and Uses*, 1st ed. (Wiley, 2003).
- [101] Y. K. Kim and M. Oliveria, *Magnetic Properties of Sputtered Fe Thin Films: Processing and Thickness Dependence*, Journal of Applied Physics **74**, 1233 (1993).
- [102] S. Meng, J. Wu, L. Zhao, H. Zheng, S. Jia, S. Hu, W. Meng, S. Pu, D. Zhao, and J. Wang, *Atomistic Insight into the Redox Reactions in Fe/Oxide Core–Shell Nanoparticles*, Chem. Mater. **30**, 7306 (2018).
- [103] E. C. Stoner and E. P. Wohlfarth, *A Mechanism of Magnetic Hysteresis in Heterogeneous Alloys*, Philosophical Transactions of the Royal Society A: Mathematical, Physical and Engineering Sciences **240**, 599 (1948).
- [104] S. Mallick, S. Mallik, B. B. Singh, N. Chowdhury, R. Gieniusz, A. Maziewski, and S. Bedanta, *Tuning the Anisotropy and Domain Structure of Co Films by Variable Growth Conditions and Seed Layers*, J. Phys. D: Appl. Phys. **51**, 275003 (2018).
- [105] O. Idigoras, A. K. Suszka, P. Vavassori, P. Landeros, J. M. Porro, and A. Berger, *Collapse of Hard-Axis Behavior in Uniaxial Co Films*, Phys. Rev. B **84**, 132403 (2011).
- [106] T. G. Knorr and R. W. Hoffman, *Dependence of Geometric Magnetic Anisotropy in Thin Iron Films*, Phys. Rev. **113**, 1039 (1959).
- [107] D. O. Smith, M. S. Cohen, and G. P. Weiss, *Oblique-Incidence Anisotropy in Evaporated Permalloy Films*, Journal of Applied Physics **31**, 1755 (1960).
- [108] S. V. Komogortsev, S. N. Varnakov, S. A. Satsuk, I. A. Yakovlev, and S. G. Ovchinnikov, *Magnetic Anisotropy in Fe Films Deposited on SiO₂/Si(001) and Si(001) Substrates*, Journal of Magnetism and Magnetic Materials **351**, 104 (2014).
- [109] J. L. Bubendorff, S. Zabrocki, G. Garreau, S. Hajjar, R. Jaafar, D. Berling, A. Mehdaoui, C. Pirri, and G. Gewinner, *Origin of the Magnetic Anisotropy in Ferromagnetic Layers Deposited at Oblique Incidence*, Europhys. Lett. **75**, 119 (2006).

- [110] A. Barranco, A. Borrás, A. R. González-Elipé, and A. Palmero, *Perspectives on Oblique Angle Deposition of Thin Films: From Fundamentals to Devices*, Progress in Materials Science **76**, 59 (2016).
- [111] G. Herzer, *Grain Size Dependence of Coercivity and Permeability in Nanocrystalline Ferromagnets*, IEEE Trans. Magn. **26**, 1397 (1990).
- [112] E. Feldtkeller, *Blockierte Drehprozesse in dünnen magnetischen Schichten / Locked rotation in thin ferromagnetic films*, it - Information Technology **3**, (1961).
- [113] J. Nowak and E. Szibel, *Domain Splitting in Thin Films with In-Plane Anisotropy*, IEEE Trans. Magn. **20**, 2105 (1984).
- [114] H. Hoffmann, *Die Abhängigkeit der Magnetisierungsschwankungen, der Domänenbreite und der Dispersion der leichten Richtung von den Schichtparametern einachsiger Permalloyfilme*, phys. stat. sol. (b) **5**, 187 (1964).
- [115] K. J. Harte, *Theory of Magnetization Ripple in Ferromagnetic Films*, Journal of Applied Physics **39**, 1503 (1968).
- [116] J. Steiner, R. Schäfer, H. Wiczorek, J. McCord, and F. Otto, *Formation and Coarsening of the Concertina Magnetization Pattern in Elongated Thin-Film Elements*, Phys. Rev. B **85**, 104407 (2012).
- [117] S. Tumański, *Handbook of Magnetic Measurements* (Taylor & Francis, Boca Raton, 2011).
- [118] E. Lopatina, I. Soldatov, V. Budinsky, M. Marsilius, L. Schultz, G. Herzer, and R. Schäfer, *Surface Crystallization and Magnetic Properties of Fe_{84.3}Cu_{0.7}Si₄B₈P₃ Soft Magnetic Ribbons*, Acta Materialia **96**, 10 (2015).
- [119] A. Hubert, *Stray-Field-Free and Related Domain Wall Configurations in Thin Magnetic Films (II)*, phys. stat. sol. (b) **38**, 699 (1970).
- [120] C. A. F. Vaz, J. A. C. Bland, and G. Lauhoff, *Magnetism in Ultrathin Film Structures*, Rep. Prog. Phys. **71**, 056501 (2008).
- [121] K. Duschek, D. Pohl, S. Fähler, K. Nielsch, and K. Leistner, *Research Update: Magnetoionic Control of Magnetization and Anisotropy in Layered Oxide/Metal Heterostructures*, APL Materials **4**, 032301 (2016).
- [122] Z. He, R. V. Gudavathy, J. A. Koza, and J. A. Switzer, *Room-Temperature Electrochemical Reduction of Epitaxial Magnetite Films to Epitaxial Iron Films*, J. Am. Chem. Soc. **133**, 12358 (2011).
- [123] D. Chiba, M. Kawaguchi, S. Fukami, N. Ishiwata, K. Shimamura, K. Kobayashi, and T. Ono, *Electric-Field Control of Magnetic Domain-Wall Velocity in Ultrathin Cobalt with Perpendicular Magnetization*, Nat. Commun. **3**, (2012).
- [124] U. Bauer, M. Przybylski, and G. S. D. Beach, *Voltage Control of Magnetic Anisotropy in Fe Films with Quantum Well States*, Physical Review B **89**, (2014).
- [125] C.-H.-T. Chang, W.-H. Kuo, Y.-C. Chang, J.-S. Tsay, and S.-L. Yau, *Tuning Coercive Force by Adjusting Electric Potential in Solution Processed Co/Pt(111) and the Mechanism Involved*, Sci. Rep. **7**, 43700 (2017).
- [126] S. Middelhoek, *Domain Walls in Thin Ni-Fe Films*, Journal of Applied Physics **34**, 1054 (1963).
- [127] G. Q. Li, H. Takahashi, H. Ito, H. Saito, S. Ishio, T. Shima, and K. Takanashi, *Morphology and Domain Pattern of L10 Ordered FePt Films*, Journal of Applied Physics **94**, 5672 (2003).
- [128] T. G. Woodcock, Y. Zhang, G. Hrkac, G. Ciuta, N. M. Dempsey, T. Schrefl, O. Gutfleisch, and D. Givord, *Understanding the Microstructure and Coercivity of High Performance NdFeB-Based Magnets*, Scripta Materialia **67**, 536 (2012).

- [129] Z. Luo, Z. Lu, C. Xiong, T. Zhu, W. Wu, Q. Zhang, H. Wu, X. Zhang, and X. Zhang, *Reconfigurable Magnetic Logic Combined with Nonvolatile Memory Writing*, *Adv. Mater.* **29**, 1605027 (2017).
- [130] D. A. Allwood, *Magnetic Domain-Wall Logic*, *Science* **309**, 1688 (2005).
- [131] C. Grezes, F. Ebrahimi, J. G. Alzate, X. Cai, J. A. Katine, J. Langer, B. Ocker, P. Khalili Amiri, and K. L. Wang, *Ultra-Low Switching Energy and Scaling in Electric-Field-Controlled Nanoscale Magnetic Tunnel Junctions with High Resistance-Area Product*, *Appl. Phys. Lett.* **108**, 012403 (2016).
- [132] Z. Wang, H. Wu, G. W. Burr, C. S. Hwang, K. L. Wang, Q. Xia, and J. J. Yang, *Resistive Switching Materials for Information Processing*, *Nat. Rev. Mater.* **5**, 173 (2020).
- [133] A. C. Torrezan, J. P. Strachan, G. Medeiros-Ribeiro, and R. S. Williams, *Sub-Nanosecond Switching of a Tantalum Oxide Memristor*, *Nanotechnology* **22**, 485203 (2011).
- [134] G. Schiavone, M. Desmulliez, and A. Walton, *Integrated Magnetic MEMS Relays: Status of the Technology*, *Micromachines* **5**, 622 (2014).
- [135] O. Cugat, J. Delamare, and G. Reyne, *Magnetic Micro-Actuators and Systems (MAGMAS)*, *IEEE Trans. Magn.* **39**, 3607 (2003).
- [136] Dr. R. M. Cornell and Prof. em. Dr. Dr. h. c. U. Schwertmann, *The Iron Oxides: Structure, Properties, Reactions, Occurrences and Uses*, Second Edition (Wiley-VCH Verlag GmbH & Co. KGaA, Weinheim, Germany, 2003).
- [137] Y. J. Tang, B. Roos, T. Mewes, S. O. Demokritov, B. Hillebrands, and Y. J. Wang, *Enhanced Coercivity of Exchange-Bias Fe/MnPd Bilayers*, *Applied Physics Letters* **75**, 707 (1999).
- [138] J. Yu, A. D. Kent, and S. S. P. Parkin, *Exchange Biasing in Polycrystalline Thin Film Microstructures*, *Journal of Applied Physics* **87**, 5049 (2000).
- [139] K. Duschek, D. Pohl, S. Fähler, K. Nielsch, and K. Leistner, *Research Update: Magnetoionic Control of Magnetization and Anisotropy in Layered Oxide/Metal Heterostructures*, *APL Mater.* **4**, 032301 (2016).
- [140] Z. He, R. V. Gudavarthy, J. A. Koza, and J. A. Switzer, *Room-Temperature Electrochemical Reduction of Epitaxial Magnetite Films to Epitaxial Iron Films*, *J. Am. Chem. Soc.* **133**, 12358 (2011).
- [141] K. Duschek, M. Uhlemann, H. Schlörb, K. Nielsch, and K. Leistner, *Electrochemical and in Situ Magnetic Study of Iron/Iron Oxide Films Oxidized and Reduced in KOH Solution for Magneto-Ionic Switching*, *Electrochem. Commun.* **72**, 153 (2016).
- [142] M. Uhlemann, A. Kraus, and A. Gebert, *Effect of a Magnetic Field on the Local PH Value in Front of the Electrode Surface during Electrodeposition of Co*, *J. Electroanal. Chem.* **577**, 19 (2005).
- [143] T. Ohtsuka, *Passivation Oxide Films and Rust Layers on Iron*, in *Characterization of Corrosion Products on Steel Surfaces*, edited by Y. Waseda and S. Suzuki (Springer Berlin Heidelberg, 2006), pp. 19–31.
- [144] A. P. Grosvenor, B. A. Kobe, N. S. McIntyre, S. Tougaard, and W. N. Lennard, *Use of QUASESTM/XPS Measurements to Determine the Oxide Composition and Thickness on an Iron Substrate*, *Surf. Interface Anal.* **36**, 632 (2004).
- [145] G. Bhargava, I. Gouzman, C. M. Chun, T. A. Ramanarayanan, and S. L. Bernasek, *Characterization of the “Native” Surface Thin Film on Pure Polycrystalline Iron: A High Resolution XPS and TEM Study*, *Applied Surface Science* **253**, 4322 (2007).

- [146] C. Navarro-Senent, J. Fornell, E. Isarain-Chávez, A. Quintana, E. Menéndez, M. Foerster, L. Aballe, E. Weschke, J. Nogués, E. Pellicer, and J. Sort, *Large Magnetolectric Effects in Electrodeposited Nanoporous Microdisks Driven by Effective Surface Charging and Magneto-Ionics*, ACS Appl. Mater. Interfaces **10**, 44897 (2018).
- [147] H. Wang, Y. Liang, M. Gong, Y. Li, W. Chang, T. Mefford, J. Zhou, J. Wang, T. Regier, F. Wei, and H. Dai, *An Ultrafast Nickel–Iron Battery from Strongly Coupled Inorganic Nanoparticle/Nanocarbon Hybrid Materials*, Nat. Commun. **3**, 917 (2012).
- [148] Z. Lu, K. Jiang, G. Chen, H. Wang, and Y. Cui, *Lithium Electrochemical Tuning for Electrocatalysis*, Adv. Mater. **30**, 1800978 (2018).
- [149] I. Díez-Pérez, P. Gorostiza, F. Sanz, and C. Müller, *First Stages of Electrochemical Growth of the Passive Film on Iron*, J. Electrochem. Soc. **148**, B307 (2001).
- [150] R. Schuster, *Electrochemical Micromachining*, Science **289**, 98 (2000).
- [151] F. Ernult, B. Dieny, L. Billard, F. Lançon, and J. R. Regnard, *Increase in Ferromagnetic/Antiferromagnetic Exchange Bias Due to a Reduction of the Interfacial Exchange Interaction*, Journal of Applied Physics **94**, 6678 (2003).
- [152] V. Höink, M. D. Sacher, J. Schmalhorst, G. Reiss, D. Engel, T. Weis, and A. Ehresmann, *Thermal Stability of Magnetic Nanostructures in Ion-Bombardment-Modified Exchange-Bias Systems*, Phys. Rev. B **73**, 224428 (2006).
- [153] X. Zhang, Q. Zhan, G. Dai, Y. Liu, Z. Zuo, H. Yang, B. Chen, and R.-W. Li, *Effect of Mechanical Strain on Magnetic Properties of Flexible Exchange Biased FeGa/IrMn Heterostructures*, Appl. Phys. Lett. **102**, 022412 (2013).
- [154] Y. Y. Wang, C. Song, J. Y. Zhang, and F. Pan, *Spintronic Materials and Devices Based on Antiferromagnetic Metals*, Progress in Natural Science: Materials International **27**, 208 (2017).
- [155] J. M. Barandiarán, J. Gutiérrez, and A. García-Arribas, *Magneto-Elasticity in Amorphous Ferromagnets: Basic Principles and Applications*, Phys. Status Solidi A **208**, 2258 (2011).
- [156] D. Atkinson, P. T. Squire, M. R. J. Gibbs, and S. N. Hogsdon, *Implications of Magnetic and Magnetoelastic Measurements for the Domain Structure of FeSiB Amorphous Wires*, J. Phys. D: Appl. Phys. **27**, 1354 (1994).
- [157] M. Han, D. F. Liang, and L. J. Deng, *Sensors Development Using Its Unusual Properties of Fe/Co-Based Amorphous Soft Magnetic Wire*, J Mater Sci **40**, 5573 (2005).
- [158] L. Xia, K. C. Chan, L. Zhao, D. Ding, and B. Z. Tang, *Magnetic Properties and Magnetostriction of a Binary Dy 50 Co 50 Amorphous Alloy*, Journal of Non-Crystalline Solids **493**, 29 (2018).
- [159] N. Eliaz and D. Eliezer, *An Overview of Hydrogen Interaction with Amorphous Alloys*, Advanced Performance Materials **6**, 5 (1999).
- [160] R. C. Bowman, Jr., *Preparation and Properties of Amorphous Hydrides*, MSF **31**, 197 (1988).
- [161] D. Paccard, C. Schlenker, O. Massenet, R. Montmory, and A. Yelon, *A New Property of Ferromagnetic-Antiferromagnetic Coupling*, phys. stat. sol. (b) **16**, 301 (1966).
- [162] B. Kaeswurm and K. O’Grady, *The Origin of Athermal Training in Polycrystalline Metallic Exchange Bias Thin Films*, Appl. Phys. Lett. **99**, 222508 (2011).

- [163] C. Binek, *Training of the Exchange-Bias Effect: A Simple Analytic Approach*, Phys. Rev. B **70**, 014421 (2004).
- [164] A. Hoffmann, *Symmetry Driven Irreversibilities at Ferromagnetic-Antiferromagnetic Interfaces*, Phys. Rev. Lett. **93**, 097203 (2004).
- [165] A. Paetzold and K. Röhl, *Thermally Activated Self-Alignment of Exchange Coupling in NiO/NiFe Bilayers*, J. Appl. Phys. **91**, 7748 (2002).
- [166] L. Thomas and B. Negulescu, *Metastable Antiferromagnetic Domain Configurations in Exchange Biased Bilayers*, Journal of Applied Physics **93**, 8606 (2003).
- [167] A. Ehresmann, C. Schmidt, T. Weis, and D. Engel, *Thermal Exchange Bias Field Drift in Field Cooled Mn₈₃Ir₁₇/Co₇₀Fe₃₀ Thin Films after 10 KeV He Ion Bombardment*, Journal of Applied Physics **109**, 023910 (2011).
- [168] J. Dho, C. W. Leung, and M. G. Blamire, *Universal Time Relaxation Behavior of the Exchange Bias in Ferromagnetic/Antiferromagnetic Bilayers*, Journal of Applied Physics **99**, 033910 (2006).
- [169] A. Migliorini, B. Kuerbanjiang, T. Huminiuc, D. Kepaptsoglou, M. Muñoz, J. L. F. Cuñado, J. Camarero, C. Aroca, G. Vallejo-Fernández, V. K. Lazarov, and J. L. Prieto, *Spontaneous Exchange Bias Formation Driven by a Structural Phase Transition in the Antiferromagnetic Material*, Nat. Mater. **17**, 28 (2018).
- [170] W. Echtenkamp and Ch. Binek, *Electric Control of Exchange Bias Training*, Phys. Rev. Lett. **111**, 187204 (2013).
- [171] J.-L. Wang, W. Echtenkamp, A. Mahmood, and C. Binek, *Voltage Controlled Magnetism in Cr₂O₃ Based All-Thin-Film Systems*, Journal of Magnetism and Magnetic Materials **486**, 165262 (2019).
- [172] J. Fujikata, K. Hayashi, H. Yamamoto, and M. Nakada, *Thermal Fluctuation Aftereffect of Exchange Coupled Films for Spin Valve Devices*, Journal of Applied Physics **83**, 7210 (1998).
- [173] L. Néel, *Thermoremanent Magnetization of Fine Powders*, Rev. Mod. Phys. **25**, 293 (1953).
- [174] E. Fulcomer and S. H. Charap, *Thermal Fluctuation Aftereffect Model for Some Systems with Ferromagnetic-antiferromagnetic Coupling*, Journal of Applied Physics **43**, 4190 (1972).
- [175] K. O'Grady, L. E. Fernandez-Outon, and G. Vallejo-Fernandez, *A New Paradigm for Exchange Bias in Polycrystalline Thin Films*, Journal of Magnetism and Magnetic Materials **322**, 883 (2010).
- [176] U. Nowak, A. Misra, and K. D. Usadel, *Domain State Model for Exchange Bias*, Journal of Applied Physics **89**, 7269 (2001).
- [177] S. K. Mishra, F. Radu, H. A. Dürr, and W. Eberhardt, *Training-Induced Positive Exchange Bias in NiFe / IrMn Bilayers*, Phys. Rev. Lett. **102**, 177208 (2009).
- [178] A. Bollero, V. Neu, V. Baltz, D. Serantes, J. L. F. Cuñado, J. Pedrosa, E. M. Palmero, M. Seifert, B. Dieny, R. P. del Real, M. Vázquez, O. Chubykalo-Fesenko, and J. Camarero, *An Extraordinary Chiral Exchange-Bias Phenomenon: Engineering the Sign of the Bias Field in Orthogonal Bilayers by a Magnetically Switchable Response Mechanism*, Nanoscale **12**, 1155 (2020).
- [179] T. Ueltzhöffer, C. Schmidt, I. Krug, F. Nickel, D. Gottlob, and A. Ehresmann, *Néel Walls between Tailored Parallel-Stripe Domains in IrMn/CoFe Exchange Bias Layers*, Journal of Applied Physics **117**, 123904 (2015).

- [180] H. Yan, Z. Feng, P. Qin, X. Zhou, H. Guo, X. Wang, H. Chen, X. Zhang, H. Wu, C. Jiang, and Z. Liu, *Electric-Field-Controlled Antiferromagnetic Spintronic Devices*, *Adv. Mater.* **32**, 1905603 (2020).
- [181] K.-J. Kim, S. K. Kim, Y. Hirata, S.-H. Oh, T. Tono, D.-H. Kim, T. Okuno, W. S. Ham, S. Kim, G. Go, Y. Tserkovnyak, A. Tsukamoto, T. Moriyama, K.-J. Lee, and T. Ono, *Fast Domain Wall Motion in the Vicinity of the Angular Momentum Compensation Temperature of Ferrimagnets*, *Nat. Mater.* **16**, 1187 (2017).
- [182] K. Cai, Z. Zhu, J. M. Lee, R. Mishra, L. Ren, S. D. Pollard, P. He, G. Liang, K. L. Teo, and H. Yang, *Ultrafast and Energy-Efficient Spin–Orbit Torque Switching in Compensated Ferrimagnets*, *Nat. Electron.* **3**, 37 (2020).
- [183] L. Caretta, M. Mann, F. Büttner, K. Ueda, B. Pfau, C. M. Günther, P. Helsing, A. Churikova, C. Klose, M. Schneider, D. Engel, C. Marcus, D. Bono, K. Bagschik, S. Eisebitt, and G. S. D. Beach, *Fast Current-Driven Domain Walls and Small Skyrmions in a Compensated Ferrimagnet*, *Nat. Nanotechnol.* **13**, 1154 (2018).
- [184] M. Huang, *PhD Thesis: Voltage Control of Electrical, Optical and Magnetic Properties of Materials by Solid State Ionic Transport and Electrochemical Reactions* <https://hdl.handle.net/1721.1/127898>.
- [185] P. Hansen and H. Heitmann, *Media for Erasable Magneto-optic Recording*, *IEEE Trans. Magn.* **25**, 4390 (1989).
- [186] TRL, *Technology Readiness Level European Union* https://ec.europa.eu/research/participants/data/ref/H2020/Wp/2014_2015/Annexes/H2020-Wp1415-Annex-g-Trl_en.Pdf.
- [187] D. A. Gilbert and A. J. Grutter, *Hydrogen Finds a Home in Ionic Devices*, *Nat. Mater.* **18**, 7 (2019).
- [188] K.-Y. Lee, S. Jo, A. J. Tan, M. Huang, D. Choi, J. H. Park, H.-I. Ji, J.-W. Son, J. Chang, G. S. D. Beach, and S. Woo, *Fast Magneto-Ionic Switching of Interface Anisotropy Using Yttria-Stabilized Zirconia Gate Oxide*, *Nano Lett.* **20**, 3435 (2020).
- [189] R. Dittmann and J. P. Strachan, *Redox-Based Memristive Devices for New Computing Paradigm*, *APL Materials* **7**, 110903 (2019).
- [190] Z. Luo, A. Hrabec, T. P. Dao, G. Sala, S. Finizio, J. Feng, S. Mayr, J. Raabe, P. Gambardella, and L. J. Heyderman, *Current-Driven Magnetic Domain-Wall Logic*, *Nature* **579**, 214 (2020).
- [191] I. P. Radu, O. Zografos, A. Vaysset, F. Ciubotaru, J. Yan, J. Swerts, D. Radisic, B. Briggs, B. Soree, M. Manfrini, M. Ercken, C. Wilson, P. Raghavan, S. Sayan, C. Adelman, A. Thean, L. Amaru, P.-E. Gaillardon, G. De Micheli, D. E. Nikonov, S. Manipatruni, and I. A. Young, *Spintronic Majority Gates*, in *2015 IEEE International Electron Devices Meeting (IEDM)* (IEEE, Washington, DC, USA, 2015), p. 32.5.1-32.5.4.
- [192] M. Prezioso, F. Merrikh-Bayat, B. D. Hoskins, G. C. Adam, K. K. Likharev, and D. B. Strukov, *Training and Operation of an Integrated Neuromorphic Network Based on Metal-Oxide Memristors*, *Nature* **521**, 61 (2015).
- [193] K. Xiao, C. Wan, L. Jiang, X. Chen, and M. Antonietti, *Bioinspired Ionic Sensory Systems: The Successor of Electronics*, *Adv. Mater.* 2000218 (2020).
- [194] <http://www.spin-ion.com/>, (n.d.).
- [195] L. Pan, F. Wang, W. Wang, G. Chai, and D. Xue, *In-Plane Isotropic Microwave Performance of CoZr Trilayer in GHz Range*, *Sci. Rep.* **6**, 21327 (2016).
- [196] P. J. Eaton and P. West, *Atomic Force Microscopy* (Oxford University Press, Oxford ; New York, 2010).

- [197] I. Horcas, R. Fernández, J. M. Gómez-Rodríguez, J. Colchero, J. Gómez-Herrero, and A. M. Baro, *WSXM : A Software for Scanning Probe Microscopy and a Tool for Nanotechnology*, *Review of Scientific Instruments* **78**, 013705 (2007).
- [198] W. Kim, C.-Y. Suh, S.-W. Cho, K.-M. Roh, H. Kwon, K. Song, and I.-J. Shon, *A New Method for the Identification and Quantification of Magnetite–Maghemite Mixture Using Conventional X-Ray Diffraction Technique*, *Talanta* **94**, 348 (2012).
- [199] R. M. Cornell and U. Schwertmann, *The Iron Oxides: Structure, Properties, Reactions, Occurrences and Uses*, 1st ed. (Wiley, 2003).
- [200] A. M. Jubb and H. C. Allen, *Vibrational Spectroscopic Characterization of Hematite, Maghemite, and Magnetite Thin Films Produced by Vapor Deposition*, *ACS Appl. Mater. Interfaces* **2**, 2804 (2010).
- [201] L. Spieß, editor, *Moderne Röntgenbeugung: Röntgendiffraktometrie für Materialwissenschaftler, Physiker und Chemiker*, 2., überarb. und erw. Aufl (Vieweg + Teubner, Wiesbaden, 2009).
- [202] T. Allmers and M. Donath, *Growth and Morphology of Thin Fe Films on Flat and Vicinal Au(111): A Comparative Study*, *New J. Phys.* **11**, 103049 (2009).
- [203] H. F. Jurca, A. Damian, C. Gougau, D. Thiaudière, R. Cortès, F. Maroun, and P. Allongue, *Epitaxial Electrodeposition of Fe on Au(111): Structure, Nucleation, and Growth Mechanisms*, *J. Phys. Chem. C* **120**, 16080 (2016).
- [204] U. Casellato, N. Comisso, and G. Mengoli, *Effect of Li Ions on Reduction of Fe Oxides in Aqueous Alkaline Medium*, *Electrochim. Acta* **51**, 5669 (2006).
- [205] W. H. Meiklejohn, *Exchange Anisotropy in the Iron-Iron Oxide System*, *Journal of Applied Physics* **29**, 454 (1958).
- [206] J. Nogués and I. K. Schuller, *Exchange Bias*, *Journal of Magnetism and Magnetic Materials* **192**, 203 (1999).

List of Figures

Figure 1.1. Electricity consumption of the ICT sector and involved subsections. In a more intuitive picture, the electricity usage of Data Centers is about two times the amount of electricity which is produced in the UK. Adapted with permission from [4].	1
Figure 1.2. Electrochemical reactions and subsequent changes on the magnetic properties.	2
Figure 2.1: Characteristics of Bloch and Néel walls in thin films.	6
Figure 2.2: Néel wall decomposed in tails and core.	7
Figure 2.3: Typical magnetization processes in a material with uniaxial anisotropy.	8
Figure 2.4: Characteristics of an exchange bias (EB) system.	9
Figure 2.5: Magneto-optical Kerr effect in longitudinal geometry. Adapted from [30]	10
Figure 3.1: Illustration of ferroelectric/ferromagnetic magneto-elastic coupling. The alternating ferro-electric domains (white arrows) transfer strain to the ferromagnetic domains (black arrows) and causes their magnetization to rotate from in-plane to out-of-plane. Reprinted from [49] under Creative Common CC-BY license.	12
Figure 3.2: Common architectures to achieve magnetoelectric effects.	12
Figure 3.3: Electrochemical control of FeO _x /Fe films polarized in 1 mol l ⁻¹ KOH.	15
Figure 3.4: Electrochemical control of a Co thin film via surface reduction and oxidation.	16
Figure 3.5: Co/GdO based architectures and switching mechanism of magnetization.	17
Figure 3.6: Hydration of Pd layer and magnetization switching.	18
Figure 3.7: Co/GdO architecture and modulations of domain wall propagation. Adapted with permission from [Ref].	18
Figure 4.1: Illumination and image forming path.	26
Figure 4.2: Influence of selected light sensitivity on the magnetic domain contrast.	26
Figure 4.3: Digital contrast enhancement.	27
Figure 5.1. In situ electrochemical cell for the Kerr microscope.	30
Figure 5.2. In situ electrochemical cell combined with the Kerr microscope.	30
Figure 5.3. CV on FeO _x /Fe/Au thin film in 1 M LiOH in the developed cell.	31
Figure 6.1: Microstructural and thickness characterization of pristine FeO _x /Fe thin film.	33
Figure 6.2: In-plane angular resolved measurements of a Au/Fe/Au and an FeO _x /Fe thin film.	35
Figure 6.3: Magnetization curves and schematic of magnetization reversal along the hard axis.	36
Figure 6.4: Magnetization reversal along the hard axis with Kerr microscopy.	37
Figure 6.5: An hysteretic measurement.	38
Figure 6.6: High resolution Kerr microscopy image of FeO _x /Fe/Au thin films.	39
Figure 7.1: In situ characterization of FeO _x /Fe thin film.	42
Figure 7.2: Electrochemical control of magnetization curves in FeO _x /Fe thin films.	45
Figure 7.3: (In situ) an hysteresis measurements.	46
Figure 7.4: Voltage control of magnetic domain size.	47
Figure 7.5. Magnetic domain images of FeO _x /Fe/Au films in LiOH solution during magnetization reversal along the hard axis in ocp state (left) and at -1.10 V (right).	50

Figure 7.6: E-induced 180° switching of magnetization by a low voltage.	52
Figure 8.1: Layer architecture and ferromagnetic layer thickness dependence of the FeO _x /Fe/IrMn exchange bias systems.	58
Figure 8.2: Electrochemical modification of EB in FeO _x /Fe(11nm)/IrMn systems.	59
Figure 8.3: Control of the magnetic properties of an EB system by the reduction time.	62
Figure 8.4: FM layer thickness dependence of E-induced EB and H _C change.	63
Figure 8.5: Correlation of the electrochemical EB modification with a partial reduction of the FeO _x and associated Fe layer thickness increase.	64
Figure 8.6: Non-volatile and partly reversible setting of EB by voltage.	66
Figure 8.7: Non-volatile voltage-induced change of oxidation state and layer thickness for an FeO _x /Fe/IrMn exchange bias system with d _{Fe,nom} = 13 nm.	67
Figure 8.8: Lateral patterning of EB and magnetic domain state by voltage.	69
Figure 9.1: Co/(Pd)/NiO thin film system – crosssection and magnetization curve.	74
Figure 9.2: Electrochemical controlled switching of EB.	75
Figure 9.3: Voltage induced changes of magnetic properties in EB system.	75
Figure 9.4: Exchange bias switching by voltage and magnetic field.	76
Figure 9.5: Cross-sectional TEM on SiO/Ta/Pd/NiO/Pd/Co/Pd/GdO _x system.	78
Figure 9.6: Model for change in exchange bias field.	80
Figure 9.7: GdCo exchange bias stack and dominant sublattice switching.	82
Figure 11.1: Visual summary of the findings in chapter 7.	89
Figure 11.2: Visual summary of the findings in chapter 8.	90
Figure 12.1: AFM images of the FeO _x /Fe/Au/Cr layers obtained in the tapping mode.	93
Figure 12.2: Raman spectra for the FeO _x /Fe/Au/Cr layers after native oxidation, which identifies Fe ₃ O ₄ as the dominant oxide. In Figure 3a, for the pristine state (black line), part of this curve (for the Raman shifts 400 – 700 cm ⁻¹) is displayed.	94
Figure 12.3: X-ray diffraction on FeO _x /Fe/Au/Cr thin films.	95
Figure 12.4: TEM crosssection of Au/Fe/Au thin film.	97
Figure 12.5: Cathodic current density <i>j</i> and inferred charge density <i>q</i> in dependence of the reduction time for the polarization of the FeO _x /Fe/Au layers at <i>E</i> = -1.10 V.	98
Figure 12.6: Angle-dependency of a,c) H _C and b,d)	99
Figure 12.7: Example for the analysis of the number of domain walls per line width in a Kerr microscopy image to quantify the average domain width.	100
Figure 12.8: Cyclic voltammogram of an FeO _x /Fe/IrMn system with d _{Fe,nom} = 11 nm in 1 mol l ⁻¹ LiOH, obtained at a rate of 20 mVs ⁻¹	101
Figure 12.9: Magnetization curves of FeO _x /Fe/IrMn systems.	102
Figure 12.10: Magnetization curve of a FeO _x /Fe/Au(10nm) film with d _{Fe,nom} = 5 nm after sputtering and removal from the vacuum chamber.	103
Figure 12.11: Magnetization curves measured in the pristine state at different positions across an FeO _x /Fe/IrMn system with d _{Fe,nom} = 13 nm. The inset depicts the measured positions on the sample area (1x1cm ²). The grey line shows the position of the	

Publication List

Publications resulting from this dissertation are marked with a ★

2021

- ★ 1. **Jonas Zehner**, Daniel Wolf, Usama M. Hasan, Mantao Huang, David Bono, Kornelius Nielsch, Karin Leistner, Geoffrey S. D. Beach
“Magnetoionic control of perpendicular exchange bias”
Physical Review Materials 2021, 5, L061401 (9pp) – Editor’s Suggestion –
DOI: 10.1103/PhysRevMaterials.5.L061401
2. **Jonas Zehner**, Olivia Vaerst, Ivan Soldatov, Kornelius Nielsch, Rudolf Schäfer, Karin Leistner
“Robust magneto-ionic effect in Fe/FeOx thin films in electrolytes with different cations”
IEEE Transactions on Magnetism 2021 – *accepted for publication* –
DOI:10.1109/TMAG.2021.3081862
3. Mantao Huang, Usama M. Hasan, Konstantin Klyukin, Delin Zhang, Deyuan Lyu, Pierluigi Gargiani, Manuel Valvidares, Sara Sheffels, Alexandra Churikova, Felix Büttner, **Jonas Zehner**, Lucas Caretta, Ki-Young Lee, Joonyeon. Chang, Jian-Ping Wang, Karin Leistner, Bilge Yildiz and Geoffrey S. D. Beach
“Voltage control of ferrimagnetic order and voltage-assisted writing of ferrimagnetic spin textures”
Nature Nanotechnology 2021 – *accepted for publication* –
4. Ivan V. Soldatov, **Jonas Zehner**, Karin Leistner, Tong Kang, Daniil Karnaushenko, Rudolf Schäfer
“Advanced, Kerr-microscopy-based MOKE magnetometry for the anisotropy characterisation of magnetic films”
Journal of Magnetism and Magnetic Materials 2021, 529, 167889
DOI: 10.1016/j.jmmm.2021.167889
5. Martin Nichterwitz, Shashank Honnali, Maksim Kutuzau, Shanshan Guo, **Jonas Zehner**, Kornelius Nielsch, Karin Leistner
“Advances in magneto-ionic materials and perspectives for their application”
APL Materials 2021, 9, 030903 (11pp)
DOI: 10.1063/5.0042544

2020

- ★ 6. **Jonas Zehner**, Ivan Soldatov, Sebastian Schneider, René Heller, Nasrin B. Khojasteh, Sandra Schiemenz, Sebastian Fähler, Kornelius Nielsch, Rudolf Schäfer, Karin Leistner
“Voltage-Controlled Deblocking of Magnetization Reversal in Thin Films by Tunable Domain Wall Interactions and Pinning Sites”
Advanced Electronic Materials 2020, 6, 2000406 (13pp)
DOI: 10.1002/aelm.202000406

7. Max Merkel, Rico Huhnstock, Meike Reginka, Dennis Holzinger, Michael Vogel, Arno Ehresmann, **Jonas Zehner**, Karin Leistner
“Interrelation between polycrystalline structure and time-dependent magnetic anisotropies in exchange-biased bilayers”
Physical Review B 2020, 102, 144421 (10pp)
DOI: 10.1103/PhysRevB.102.144421
8. Martin Nichterwitz, Shashank Honnali, **Jonas Zehner**, Sebastian Schneider, Darius Pohl, Sandra Schiemenz, Sebastian T. B. Goennenwein, Kornelius Nielsch, Karin Leistner
“Control of Positive and Negative Magnetoresistance in Iron Oxide-Iron Nanocomposite Thin Films for Tunable Magnetoelectric Nanodevices”
ACS Applied Electronic Materials 2020, 2, 8, 2543 (7pp)
DOI: 10.1021/acsaelm.0c00448

2019

- ★ 9. **Jonas Zehner**, Rico Huhnstock, Steffen Oswald, Ulrike Wolff, Ivan Soldatov, Arno Ehresmann, Kornelius Nielsch, Dennis Holzinger, Karin Leistner
“Nonvolatile Electric Control of Exchange Bias by a Redox Transformation of the Ferromagnetic Layer”
Advanced Electronic Materials 2019, 5, 1900296 (11pp)
DOI: 10.1002/aelm.201900296

2018

10. Kenny Duschek, Andreas Petr, **Jonas Zehner**, Kornelius Nielsch, Karin Leistner
“All-electrochemical voltage-control of magnetization in metal oxide/metal nanoislands”
Journal of Materials Chemistry C 2018, 6, 8411 (7pp)
DOI: 10.1039/C8TC01994K
11. Karin Leistner, Kenny Duschek, **Jonas Zehner**, Mingze Yang, Andreas Petr, Kornelius Nielsch, Karen L. Kavanagh
“Role of Hydrogen Evolution during Epitaxial Electrodeposition of Fe on GaAs”
Journal of the Electrochemical Society 2018, 165, H3076 (4pp)
DOI: 10.1149/2.0071804jes

2017

12. Alexander Drayton, **Jonas Zehner**, James Timmis, Vijay Patel, Gonzalo Vallejo-Fernandez, Kevin Dermot O’Grady
“A comparative measurement technique of nanoparticle heating for magnetic hyperthermia applications”
Journal of Physics D: Applied Physics 2017, 50, 495003 (6pp)
DOI: 10.1088/1361-6463/aa95d8

Acknowledgments

I am very grateful to Prof. Kornelius Nielsch for giving me the opportunity to work at the IFW and being my first referee. He gave me a lot of autonomy when it comes to my research, which is what I hoped for. I want to emphasize his commitment for building a strong community among the PhD students, for example by initiating the PhD seminars, enabling the participation in international conferences or research stays abroad.

I am thankful to Prof. Sebastian Goennenwein for his willingness being the second referee and to Dr. habil. Liza Herrera Diez being the third referee.

I am fortunate to have Dr. Karin Leistner as my PhD advisor. Her constant support, optimistic attitude and my success under her direction inspired me to keep on this path. Valuable discussions and suggestions helped me to gain a deeper understanding of electrochemistry and magnetism. I would also like to acknowledge the members of Karins group for their help and support.

My growth and progress in the field of magnetism would not have been possible without the professional input of Prof. Rudolf Schäfer. He gave me good advice on how to properly conduct research.

I am particularly grateful for the years of beautiful Kerr microscopy work together with Dr. Ivan Soldatov.

I thank Prof. Geoffrey Beach for hosting me at the Massachusetts Institute of Technology, an experience which broadened my scientific and cultural horizon. Special thanks to my teammates in the Beach group for their help and support.

I would like to thank my collaborators, especially Rico Huhnstock and Max Merkel from the University of Kassel, who enabled our experimental measurements.

I would like to acknowledge the IFW research department, especially Stefanie Gloge and Ralf Voigtländer who made the realization of the in situ cell possible.

I am thankful to Sebastian, David, Daniel and Lauritz. They are wonderful people to spend the lunch time and to unwind with. I am also thankful to all the other PhD students, scientists and staff of the IFW who always supported me.

I thank my family for their encouragement, care and constant support. I am especially grateful to my parents Dagmar and Fridolin for their unconditional love. I am thankful to have Arianna at my side. I thank her for her love and wisdom.

Symbols

Symbol	Term
a	Néel wall core thickness
A	Exchange constant
A_A	Area
d	Film thickness
E	Electric potential
F	Faraday constant
γ	Surface energy density
γ'	Euler-Mascheroni constant
H	Applied field
H_{EB}	Exchange bias field
H_C	coercivity
j	Current density
K_d	Stray field energy coefficient
K_U	Uniaxial anisotropy constant
μ_0	Vacuum permeability
m	Mass
M	Magnetization
(M)	Molar Mass
M_R	Remanence
M_S	Saturation Magnetization
N	Demagnetizing factor
Q	Quality factor
Q'	Electrical charge
ρ	Density
t	time
V_g	Gate Voltage
T	Temperature
z	number of exchanged electrons

Acronyms

AFM – antiferromagnet

FM - ferromagnet

EB – exchange bias

PMA – perpendicular magnetic anisotropy

Statement of Authorship

Erklärung

Hiermit versichere ich, dass ich die vorliegende Arbeit ohne unzulässige Hilfe Dritter und ohne Benutzung anderer als der angegebenen Hilfsmittel angefertigt habe; die aus fremden Quellen direkt oder indirekt übernommenen Gedanken sind als solche kenntlich gemacht. Bei der Auswahl und Auswertung des Materials sowie bei der Herstellung des Manuskripts habe ich Unterstützungsleistungen von folgenden Personen erhalten: Dr. Karin Leistner, Prof. Kornelius Nielsch, Prof. Rudolf Schäfer. Weitere Personen waren an der geistigen Herstellung der vorliegenden Arbeit nicht beteiligt. Insbesondere habe ich nicht die Hilfe eines kommerziellen Promotionsberaters in Anspruch genommen. Dritte haben von mir keine geldwerten Leistungen für Arbeiten erhalten, die in Zusammenhang mit dem Inhalt der vorgelegten Dissertation stehen. Die Arbeit wurde bisher weder im Inland noch im Ausland in gleicher oder ähnlicher Form einer anderen Prüfungsbehörde vorgelegt und ist auch noch nicht veröffentlicht worden. Die Promotionsordnung der Fakultät Maschinenwesen aus dem Jahr 2001 wird anerkannt.

Jonas Zehner, Dresden im Dezember 2020